© COPYRIGHTED BY

Shansong Jiang

December 2015

PROGRESSING THE UNDERSTANDING AND CAPABILITY OF TWO DISTINCT ISOLATED TASK SPECIFIC INVERSE SCATTERING SUBSERIES: (1) REFERENCE VELOCITY REQUIREMENTS FOR THE ISS INTERNAL MULTIPLE ATTENUATION, AND (2) EXTENDING THE ISS DEPTH IMAGING FOR A VARIABLE MULTI-PARAMETER SUBSURFACE

A Dissertation

Presented to

the Faculty of the Department of Physics

University of Houston

In Partial Fulfillment

of the Requirements for the Degree

Doctor of Philosophy

By

Shansong Jiang

December 2015

PROGRESSING THE UNDERSTANDING AND CAPABILITY OF TWO DISTINCT ISOLATED TASK SPECIFIC INVERSE SCATTERING SUBSERIES: (1) REFERENCE VELOCITY REQUIREMENTS FOR THE ISS INTERNAL MULTIPLE ATTENUATION, AND (2) EXTENDING THE ISS DEPTH IMAGING FOR A VARIABLE MULTI-PARAMETER SUBSURFACE

Shansong Jiang

APPROVED:

Dr. Arthur B. Weglein, Chairman
Dept. of Physics

Dr. Kevin E. Bassler,
Dept. of Physics

Dr. Lowell T. Wood,
Dept. of Physics

Dr. Fang Liu,
Dept. of Physics

Dr. David J. Francis,
Dept. of Psychology

Dean, College of Natural Sciences and Mathematics

Acknowledgements

This dissertation documents the research work during my doctoral period between the Fall of 2007 and the Fall of 2009. Upon the completion of my PhD program, here I would like to express my sincere acknowlegements to my professors, friends, and family members who have ever offered infinite help, warmth, passion and encouragement during the past 5-year passage of study to my doctoral degree in the USA.

First of all, my deep appreciation goes to my PhD advisor, Professor Arthur Weglein who is such a highly capable physicist with serious professionalism when he explores the issues in technical world, but also with a wonderful personality full of humor and enthusiasm. He shares his life happiness with everyone around him. I feel so honored in pursuit of my doctoral research on Seismic Physics after Professor Weglein. I thank him for launching a very challenging but quite informative research topic for me, for his intellectual supervision on my doctoral work, sufficient patience, and warm-hearted encouragement to me when I was emotionally perplexed, under academic pressure, and for his invaluable positiveness and generosity provided to me. I have benefited greatly from the technical learning from Professor Weglein and the invaluable knowlege beyond textbooks that he imparted to me.

I am indebted to Dr. Simon Shaw for offering me a wonderful internship opportunity and for his co-mentoring with Professor Weglein on my doctoral research during my internship projects at ConocoPhillips. Without Dr. Shaw's careful and insightful instruction, it would be impossible for me to achieve such a productive research in such a short term. I would also like to thank Dr. Haiyan Zhang for her generous

assistance during my stay at ConocoPhillips. I am much appreciative to Simon and Haiyan for helping me get an approval from ConocoPhillips company management for the permission, so that I can write into my thesis on the research work done during my internship. This research consists of: (1). the ISS internal multiple attenuator's sensitivity to reference velocity for land application; (2). initial numerical tests of multi-parameter ISS LOIS/HOIS imaging algorithms for a layered acoustic medium with both velocity and density variation.

Next, I need to express my sincere gratitude to Dr. Ruben Martinez who offered me the very first industrial internship opportunity at Petro-Geo-Service in Houston, where I gained quantative seismic industry data processing skills. Dr. Faqi Liu and Dr. Scott Morton are thanked for their strong support and mentoring when I had the great internship at the HESS corporation. Dr. Faqi Liu is also very much thanked for his consistent encouragement and strong recommendations, whenever I ask for them. I would also like to thank Dr. Kenneth Matson for offering me a great internship experience at BP (British Petroleum), Dr. Nurul Kabir for mentoring my internship project, and Drs. Jingfeng Zhang and Kyoung-Jin Lee for their warm help during my internship at BP.

I am also grateful to all my M-OSRP's colleagues: Drs. Fang Liu, Haiyan Zhang, Jingfeng Zhang, Adriana Citlali Ramirez Perez, Jose Eduardo Lira, Zhiqiang Wang, Xu Li, Shih-Ying Hsu, Jim Mayhan, Hong Liang, and Dr. Jinlong Yang, Chao Ma, Yanglei Zou, Xinglu Lin, Jing Wu, Qiang Fu, Yuchang Shen and Zhen Zhang, for their valuable research discussion and every assistance. Dr. Jim Mayhan and Dr. Jinglong Yang are specially thanked for their invaluable reviewing and assistance

during this dissertation writing. M-OSRP's sponsors are thanked for their strong financial support and research encouragement.

Both my current and previous Ph.D committee Professors and Drs. are very much thanked for serving on the committee: Professors Arthur Weglein, Kevin Bassler, Lowell Wood, Fang Liu, David Francis, Kristopher Innanen, Edward Hungerford, Lawrence Pinsky, Lennart Johnsson, Dr. Kenneth Matson and Dr. Simon Shaw.

I am also thankful to Jennifer Chin-Davis and Naomi Haynes for their long-term coordination and warm assistance on graduate work in the Department of Physics.

A special thank-you goes to Chris Weglein and Haiyan and Jingfeng who shared invaluable parenting advices and experience with my wife Min and I when we became new parents in 2009.

At last, I would like to express my deep gratitude to my parents who taught me righteousness and integrity as the basis of life. My wife Min and my daughter Sophie deserve my most heart-felt thanks because they are the source of my passion in life, and I specially thank Min for her dedication to the family and sharing with me both my excitement and affliction on the way to every success.

PROGRESSING THE UNDERSTANDING AND CAPABILITY OF TWO DISTINCT ISOLATED TASK SPECIFIC INVERSE SCATTERING SUBSERIES: (1) REFERENCE VELOCITY REQUIREMENTS FOR THE ISS INTERNAL MULTIPLE ATTENUATION, AND (2) EXTENDING THE ISS DEPTH IMAGING FOR A VARIABLE MULTI-PARAMETER SUBSURFACE

An Abstract of a Dissertation

Presented to

the Faculty of the Department of Physics

University of Houston

In Partial Fulfillment

of the Requirements for the Degree

Doctor of Philosophy

By

Shansong Jiang

December 2015

Abstract

To achieve seismic exploration goals, conventional seismic data processing methods need subsurface information (for example velocity distribution and earth structure), which is generally inaccessible for geologically complex regions. Seismic algorithms derived from inverse scattering series (*ISS*) do not require subsurface information, but they directly invert seismic data (with a reference medium) order by order for achieving seismic processing objectives.

The ISS internal multiple attenuator (*IMA*) is data-driven and uses a constant reference velocity (water speed for marine cases, and p-wave and s-wave velocities for land cases) to accurately predict all leading order internal multiples' arrival time. However, in the land application of ISS IMA, it is hard to choose a simple constant elastic medium as the reference, due to the heterogeneous and complicated properties in near surface layer. This dissertation presents research on the ISS IMAs sensitivity to the reference velocity in land cases. An analytical calculation of the ISS IMA is performed for a 1D layered earth with multi-component PP, PS, SP and SS (P denotes compressional wave, and S denotes shear wave) data at both normal and non-normal incidence. The computation demonstrates that the prediction of 1D ISS IMA is independent of the chosen P and S reference velocities. Numerical tests on the 1D ISS IMA algorithm are done for different types of media to demonstrate its value for land applications.

The leading order imaging subseries (*LOIS*) and higher order imaging subseries (*HOIS*) methods for the one-parameter (velocity variation only) case can fail for an acoustic medium with both velocity and density variation. Hence, a multi-parameter

LOIS imaging algorithm is derived and tested in this dissertation to extend the one-parameter imaging algorithms to a 1D two-parameter (velocity and density) acoustic medium, and to a more complete earth model, eventually. The calculation of the ISS third order term for a 1D acoustic medium leads to the identification of the two-parameter LOIS algorithm, and justifies the multi-parameter LOIS and HOIS imaging conjectures. Analytical and synthetic tests are done for the two-parameter LOIS and HOIS algorithms to demonstrate their different imaging capability: HOIS is better than LOIS in locating subsurface interfaces for an acoustic medium with larger contrast and error duration in velocity and density. The multi-parameter LOIS and HOIS imaging algorithms are capable of outputting subsurface structure without using a velocity model.

Contents

List of Figures **xi**

1 Introduction **1**

1.1 Seismic exploration 2

1.2 Inverse scattering series 10

1.3 Dissertation overview 20

2 Elastic internal multiple attenuation using inverse scattering series **22**

2.1 Chapter overview 22

2.2 Introduction to elastic internal multiple attenuation 23

2.3 Reference velocity insensitivity of the 1D elastic IMA 28

2.3.1 Analytic analysis (part I): 1D normal incidence 29

2.3.2 Analytic analysis (part II): 1D non-normal incidence 34

2.4 Numerical tests 38

2.4.1 Tests on acoustic over elastic media 38

2.4.2 Tests on elastic multi-component geophone data 46

2.5 Conclusion 52

3 Multi-parameter imaging algorithms using inverse scattering series **53**

3.1 Chapter overview 53

3.2 Background introduction 54

3.2.1 1D two-parameter acoustic medium 57
3.2.2 Results of the first two ISS terms 58
3.2.3 Conjectured multi-parameter imaging algorithms 58
3.3 Derivation of two-parameter acoustic imaging algorithms 63
3.3.1 Analytic derivation of the 3^{rd} order *ISS* term 64
3.3.2 Examination on the one-parameter case 66
3.3.3 Leading order imaging series and its closed form 68
3.4 Analytic analyses 74
3.4.1 1D two-parameter acoustic model 74
3.4.2 1D analytic data preparation 74
3.4.3 Analytic calculation of *LOIS* closed form 78
3.4.4 Analysis on the shifted quantity 79
3.4.5 Numerical evaluations using analytic data 82
3.5 Synthetic tests 96
3.5.1 Imaging with band-limited data 97
3.5.2 Polarity reversal test 105
3.6 Conclusion and discussion 107

4 Summary **112**

References **117**

Appendices

A Mathematical derivation of α_3 and β_3 of the 3^{rd} term in the *ISS* for a 1D two-parameter acoustic medium case **127**

List of Figures

1.1 *A cartoon illustrating two typical types of seismic experiments: (a). a marine seismic acquisition (http://www.championsforcetaceans.com); (b). a land seismic acquisition (http://www.lingo.cast.uark.edu). In both cases, a man-made source is ignited to send seismic waves downward into the earth, and reflected waves (only primaries are here) are collected at the situated array of receivers. An exact repeated experiment will be done by moving the man-made source to the next location with a specified distance in between.* 3

1.2 *Categorization of seismic events in the marine case: a. direct wave, b. ghosts (source-side and receiver-side), c. primary, d. free surface multiple, e. internal multiple. More detailed definitions can be found in Weglein et al. (2003).* 5

2.1 *A cartoon picture demonstrating the mechanism of the* 1^{st} *order elastic IMA : two deeper primaries and one shallower primary controlled by pseudo-depths are used to construct all* 1^{st} *order internal multiples in one step. The total arrival time of the predicted internal multiple is the sum of two deeper primaries' arrival times subtracted by one shallower primary event's arrival time.* 27

2.2 *A cartoon picture of the experiment layout for a 1D non-normal incidence elastic case:* x_h *is the offset between sources and geophones.* . . 34

2.3 *Predicted* 1^{st} *order internal multiples on a 5-layer acoustic medium: left-hand side is the input shot gather where all* 5 *p-leg primaries are denoted by red letters, and the right-hand side is the prediction of the* 1^{st} *order internal multiples.* 40

2.4 *A zoom-in comparison of amplitude prediction and wavelet difference between predicted 1^{st} order internal multiples and input shot gather.* . 41

2.5 *A comparison between the input shot gather and the predicted internal multiples for an acoustic over isotropic elastic medium: for a clearer further comparison, the 2^{nd} order internal multiples denoted by white letters are also predicted by using the 1D acoustic IMA code which has included the prediction.* 43

2.6 *The IMA prediction for an acoustic over anisotropic elastic VTI medium* 44

2.7 *The same prediction result of previous VTI medium with NMO: the arrival time prediction at far offsets is also accurate, as denoted by the yellow dashed horizontal line.* 45

2.8 *A 3-layer elastic model to test reference velocity insensitivity: in the model, p-wave velocity, s-wave velocity and density are all varied to simulate an approximated earth structure for multi-component data.* . 47

2.9 *Predicted 1^{st} order internal multiples in XX direction using $c_0 = 1500m/s$: left-hand side is the XX direction input shot gather, and the right-hand side is the prediction.* 48

2.10 *Predicted 1^{st} order internal multiples in XX direction using $c_0 = 1000m/s$: left-hand side is the XX direction input shot gather, and the right-hand side is the prediction.* 49

2.11 *Predicted 1^{st} order internal multiples in YY direction using $c_0 = 1500m/s$: left-hand side is the YY direction input shot gather, and the right-hand side is the prediction.* 50

2.12 *Predicted 1^{st} order internal multiples in YY direction using $c_0 = 1000m/s$: left-hand side is the YY direction input shot gather, and the right-hand side is the prediction.* 51

3.1 *A 1D acoustic model with both velocity(c_0, c_1, c_2) and density (ρ_0, ρ_1, ρ_2) variations in the three layers, where θ, i_1, i_2 are three incident angles in the layers, respectively; a and b are two constants to express the real depths of the two interfaces. For simplicity, both source depth z_s and receiver depth z_g are set to zero.* 75

3.2 *Imaging comparison 1: left figure is a result of constant velocity (c_0=1500 m/s) migration, middle and right figures are results using two-parameter ISS LOIS imaging algorithm, where the blue dashed lines are the real depths of the two interfaces in the model. The color scale beside each graph denotes the value of reflection amplitude in each layer.* 84

3.3 *Imaging comparison 2: the outer two figures are the results of constant velocity (c_0=1500 m/s) migration, the inner two figures are the corresponding results using two-parameter ISS LOIS imaging algorithm, where the blue dashed lines are the real depths of the two interfaces in the model. The color scale beside each graph denotes the value of reflection amplitude in each layer.* 85

3.4 *Imaging comparison 3: left figure is a result of constant velocity (c_0=1500 m/s) migration, middle and right figures are results using two-parameter ISS LOIS imaging algorithm, where the blue dashed lines are the real depths of the two interfaces in the model. The color scale beside each graph denotes the value of reflection amplitude in each layer.* 87

3.5 *Imaging comparison 4: right figure is a result of constant velocity (c_0=1600 m/s) migration, left figure is the result using two-parameter ISS LOIS imaging algorithm, where the blue dashed lines are the real depths of the two interfaces in the model. The color scale beside each graph denotes the value of reflection amplitude in each layer.* 88

3.6 *Imaging comparison 5: both figures are results using two-parameter ISS LOIS imaging algorithm, where the blue dashed lines are the real depths of the two interfaces in the model. The color scale beside each graph denotes the value of reflection amplitude in each layer.* 89

3.7 *Results of $\alpha_1(z,\theta) - \beta_1(z,\theta)$ for the three different models, where the blue dashed lines are the real depths of the two interfaces in the model. The color scale beside each graph denotes the value of reflection amplitude in each layer.* 90

3.8 *Imaging comparison 6: right figure is a result of constant velocity (c_0=1500 m/s) migration, middle and left figures are results using two-parameter ISS LOIS and HOIS imaging algorithms, respectively, where the yellow dashed lines are the real depths of the two interfaces in the model. The color scale beside each graph denotes the value of reflection amplitude in each layer.* 91

3.9 *Imaging comparison 7: right figure is a result of constant velocity (c_0=1500 m/s) migration, middle and left figures are results using two-parameter ISS LOIS and HOIS imaging algorithms, respectively, where the yellow dashed lines are the real depths of the two interfaces in the model. The color scale beside each graph denotes the value of reflection amplitude in each layer.* 92

3.10 *The sensitivity of density changes to the result of the two-parameter ISS LOIS imaging algorithm: velocity model keeps same in all models. The yellow dashed lines are the real depths of the two interfaces in the model. The color scale beside each graph denotes the value of reflection amplitude in each layer.* 93

3.11 *The sensitivity of density changes to the result of the two-parameter ISS HOIS imaging algorithm: velocity model keeps same in all models. The yellow dashed lines are the real depths of the two interfaces in the model. The color scale beside each graph denotes the value of reflection amplitude in each layer.* 94

3.12 *Effect of depth duration changes to the results of constant velocity migration and the two-parameter ISS LOIS/HOIS imaging algorithms: for all models,density and velocity values are same in each layer. The yellow dashed lines are the real depths of the two interfaces. The color scale beside each graph denotes the value of reflection amplitude in each layer.* 95

3.13 *A reflectivity model used to generate bandlimited datasets for a 1D two-parameter acoustic medium with specific parameter contrast.* . . . 98

3.14 *Dataset with bandwidth of 1.0 hz $\sim$ 60 hz expressed in $(\tau - p)$ domain and in $(z - p)$ domain: the green lines in the graphs indicate the actual depths of the three interfaces in the model, and primaries and internal multiples are identified by the arrows. The color scale beside each graph denotes the value of each seismic event's (primary's or multiple's) reflection amplitude in each layer.* 99

3.15 *Dataset with bandwidth of 0.01 hz $\sim$ 60 hz expressed in $(\tau - p)$ domain and in $(z - p)$ domain: the green lines in the graphs indicate the actual depths of the three interfaces in the model, and primaries and internal multiples are identified by the arrows. The color scale beside each graph denotes the value of each seismic event's (primary's or multiple's) reflection amplitude in each layer.* 100

3.16 *Imaging results comparison among constant velocity migration, LOIS and HOIS for band-limited dataset of 1.0 hz ∼ 60 hz: the green lines in the graphs indicate the actual depths of the three interfaces in the model. The color scale beside each graph denotes the value of each seismic event's (primary's or multiple's) reflection amplitude in each layer.* 102

3.17 *Imaging results comparison among constant velocity migration, LOIS and HOIS for band-limited dataset of 0.01 hz ∼ 60 hz: the green lines in the graphs indicate the actual depths of the three interfaces in the model. The color scale beside each graph denotes the value of each seismic event's (primary's or multiple's) reflection amplitude in each layer.* 103

3.18 *A further imaging comparison among constant velocity migration, LOIS, HOIS for band-limited dataset of 0.01 hz ∼ 60 hz and HOIS by using full bandwidth data: the green lines in the graphs indicate the actual depths of the three interfaces in the model; the yellow lines show the location of horizontal slowness value with good results corresponding incicent angles below* 30°*. The color scale beside each graph denotes the value of each seismic event's (primary's or multiple's) reflection amplitude in each layer.* 104

3.19 *An acoustic two-parameter 1D model specifically designed to test the polarity reversals* 106

3.20 *Imaging comparison between water-speed velocity migration and ISS HOIS results over the synthetic dataset with two deeper layers of polarity reversals: green lines in the graphs indicate the actual location of all interfaces; yellow dashed lines indicate the* 2^{nd} *interfaces after two migration methods. Improved image for far-offset is denoted by the two white arrows. The color scale beside each graph denotes the value of reflection amplitude in each layer.* 108

3.21 *A zoom-in ISS HOIS imaging result for the polarity reversal model: reflection coefficients' phases transit the zero value boxed in the pink dash line* 109

Chapter 1

Introduction

In this chapter, I will first present a brief introduction to the background of general seismic exploration and the challenges and issues in current seismic exploration. Then, I will introduce inverse scattering series and its task-specific subseries, and the seismic application of inverse scattering series to address the pressing challenges encountered in current seismic exploration. At the end of this chapter, I will provide an overview of this dissertation.

1.1 Seismic exploration

The goal of seismic exploration is to locate hydrocarbon reservoirs[1]with high commercial value underlying the earth's surface. To accurately locate hydrocarbon accumulations, a seismic experiment, called seismic acquisition, is first conducted on shore or off shore (figure 1.1) to collect seismic data[2]. Afterwards the seismic data are further processed by geoscientists (a process called seismic data processing) to reveal information about the undergound earth. In seismic exploration, man-made sources such as air guns (for marine cases), dynamite, or seismic vibrators (for land cases) are deployed and ignited to generate high-energy seismic waves in a very short-time interval. Such high-energy seismic waves propagate through, get refracted by, and are partially reflected by the rock layers of the earth's subsurface, then travel back to the measurement surface where they are recorded by receivers, such as hydrophones in marine acquisition and geophones on land exploration. Figure 1.1 shows both cases, marine and land seismic acquisition.

A seismic event is a temporally localized arrival of seismic wave energy. The entirety of seismic events recorded by the receivers constitutes seismic data. Since seismic data are huge in volume and are comprised of complicated subsurface information, geoscientists must employ different seismic algorithms to achieve the final seismic goal of locating hydrocarbon targets. Seismic data processing is therefore

[1]A subsurface body of rock having sufficient porosity and permeability to store and transmit fluids. Sedimentary rocks are the most common reservoir rocks because they have more porosity than most igneous and metamorphic rocks and form under temperature conditions at which hydrocarbons can be preserved. A reservoir is a critical component of a complete petroleum system. -From Schlumberger Oilfield Glossary:www.glossary.oilfield.slb.com

[2]Generally speaking, seismic data are a temporal series of recorded sonic wave arrivals with certain localized energy.

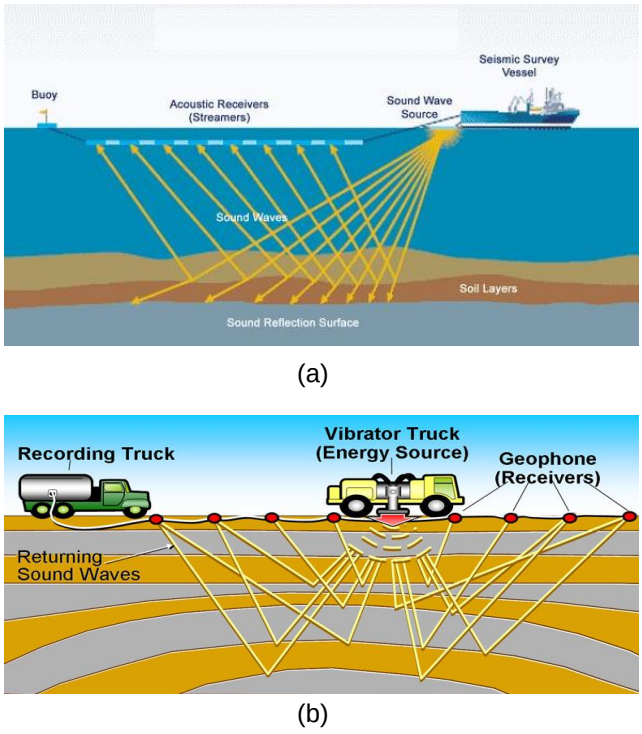

Figure 1.1: *A cartoon illustrating two typical types of seismic experiments: (a). a marine seismic acquisition (http://www.championsforcetaceans.com); (b). a land seismic acquisition (http://www.lingo.cast.uark.edu). In both cases, a man-made source is ignited to send seismic waves downward into the earth, and reflected waves (only primaries are here) are collected at the situated array of receivers. An exact repeated experiment will be done by moving the man-made source to the next location with a specified distance in between.*

divided into several stages. A typical sequence of current seismic data processing is:

- Seismic data preprocessing (random noise suppression, data interpolation and extrapolation, source wavelet estimation);
- Deghosting;
- Free surface multiple removal/attenuation;

- Internal multiple removal/attenuation;
- Imaging, and
- Inversion.

Next, I will give a set of definitions of recorded seismic events so that the above data processing sequence will be better understood. In seismic exploration, seismic events are defined according to whether or not they, in their propagating history, have been reflected from the interfaces under the earth (see the cartoon illustration of the categorization of seismic events in figure 1.2).

Events propagating straight from the source to the receiver are called direct waves. Ghosts are events that start their history propagating upward from the source or end their history as the downgoing recorded wavefield at the receiver.

Events that start downward from the source or end upward at the receiver and have experienced their upward reflections from underground interfaces, are further classified into primaries and multiples. Primaries are seismic events which have experienced only one upward reflection at the underlying interfaces below the free surface. Events with more than one upward reflection at the subsurfaces of the earth are called multiples. Multiples are further divided into free surface multiples and internal multiples. Free surface multiples are multiples that have at least one of their downward reflections at the free surface (defined as air-water interface for marine or air-land interface for land). Internal multiples are multiples which have all of their downward reflections below the free surface. The order of internal multiples is defined by the number of their downward reflections at those subsurfaces, whereas, the order

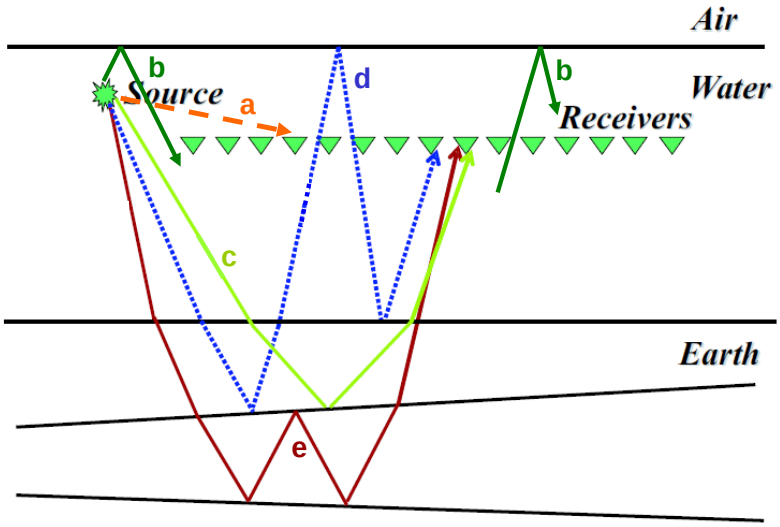

Figure 1.2: *Categorization of seismic events in the marine case: a. direct wave, b. ghosts (source-side and receiver-side), c. primary, d. free surface multiple, e. internal multiple. More detailed definitions can be found in Weglein et al. (2003).*

of free surface multiples is decided by the number of their downward reflections at the free surface, independent of the total numbers of downward reflections in their propagation history. More specific and detailed definitions of these seismic events can be found in the review paper by Weglein et al. (2003).

Now I will explain why current seismic data processing uses the previously listed workflow to achieve the objective of seismic exploration. Compared with other seismic events, primaries have a much simpler spatial traveling history (only one upward

reflection), and hence primaries require simpler logic mathematic algorithms to create a map of earth structure (imaging) and the change of mechanical properties (inversion) of the earth. Therefore, most current seismic algorithms view primaries as the basic seismic signals for achieving seismic goals, and treat other seismic events as noise. In other words, ghosts and multiples contain quantative information about the subsurface they have experienced, but the inability of current seismic data processing algorithms to extract useful information leads to the categorization of ghosts and multiples as noise, and their removal from seismic data.

The seismic data processing sequence assumes each processing step is taken in the right order so that the next step will be accomplished to its full capability. If preprocessing of seismic data is done well, and direct waves, ghosts, free-surface multiples and internal multiples are removed from the original data, the remaining wave energy, corresponding to primaries only, is then ready to be processed to extract information about reflectors' spatial location and to figure out the change of mechanical properties (such as density change, velocity variation etc.) across underground interfaces. The processes are listed as the last two stages in the above seismic processing sequence, imaging and inversion, respectively.

Primaries contain both time and amplitude information. Seismic imaging is a procedure to map the seismic energy of primaries in time domain as displayed in the recorded data set, to the geological boundaries of earth properties in depth domain. In physics, the mapping from time to depth is the multiplication of time by

velocity. All current conventional imaging algorithms only use the temporal information embedded in the primaries, and they assume that an accurate velocity model[3] is provided for the full imaging capability to be reached in the imaging procedure. Hence, a conventional imaging result relies heavily on an accurate velocity model created through velocity analysis, a process generally taken before performing a conventional imaging procedure. After the imaging process, the amplitude of primaries will then be used in the inversion AVO[4] analysis stage to identify the change of properties across the imaged earth interfaces. The accuracy of both imaging and inversion plays a pivotal role for geoscientists in interpreting the final processed data and hence in making conclusions regarding where and how oil companies drill a well for reaching oil and gas.

As mentioned previously, each step in the processing chain depends on the algorithms applied at that stage for a specified processing goal, and the result of the processing is also dependent on how effectively the previous processing stage was achieved. In this dissertation, my work will focus on the internal multiple attenuation/removal and imaging parts in the seismic processing sequence. So I will discuss the pressing challenges and issues on these two topics.

[3]Seismic velocity model means the configuration of various velocity values that seismic waves propagate with in the different layers of subsurface media. Current velocity analysis processes establish a velocity model through recorded data by employing different techniques, such as normal-moveout, travel time tomography, migration velocity analysis, and full waveform inversion (abbreviated as FWI). For an overview of velocity estimation methods, please refer to Gray et al. (2001).

[4]AVO is a geophysics term abbreviated for amplitude variation with offset, or amplitude versus offset. The amplitude of the recorded seismic wave energy at the receriver array generally varies with the distance (called offset) between the source and each receiver. This variation is used by geoscientists to determine subsurface mechanical properties such as density, velocity, porosity, and fluid content.

Removing or attenuating multiples is a prerequisite for achieving a clear imaging of earth structure and accurately determining earth propery changes through inversion. In the history of seismic exploration, geophysicists have been extensively involved in proposing effective and efficient methods and algorithms to attenuate or eliminate the coherent noise of multiples. Weglein and Dragoset (2005) collected a comprehensive list of literature on multiple removal. Current multiple removal or attenuator algorithms are based either on assumptions of the seismic data characteristics (primaries and random multiples are periodic, sufficient velocity discrimination exists between primaries and multiples) or on the nature of the earth (seismic velocity is fully determined and the earth is assumed to be one-dimensional) (Weglein and Dragoset, 2005). These methods are effective in suppressing coherent noise when the assumptions of the methods are well satisfied or mildly violated. However, the assumptions made by these conventional multiple removal algorithms can be easily and seriously violated in many geological complex regions, which lead to incorrect interpretation of the original data set (Weglein et al., 2003). The inability to attenuate or eliminate multiples can obstruct the following seismic processing chain, since the existence of multiples can cause destructive interference with primaries. The misinterpretation with multiples-entangled signals, generally, result in poor drilling decisions with high risk of negative financial cost, economic burden and political impact. Hence, a much more reliable multiple-removal method is in great demand, especially for exploration in geologically complex area.

A similar challenge also arises from imaging field data. Many imaging methods were proposed in the past decades (Hagedoorn, 1954; Claerbout, 1971; French, 1974;

Schneider, 1978; Stolt, 1978; Stolt and Weglein, 1985). Among the most popular imaging approaches are FK migration, Kirchhoff migration, Gaussian Beam theory, and the RTM method. All of these conventional imaging methods are effective, based on their prerequisite of utilizing a highly-accurate velocity model. In other words, when provided accurate velocity models, all these imaging tools can output the depth configuration of the subsurface earth interfaces to different extents of accuracy. However, with higher and higher demand for energy, current seismic exploration is moving toward regions with more and more complex geological features, such as deepwater subsalt areas, ill-defined sub-basalt, and sub-karsted sediments. In these areas, most current velocity estimation techniques are not capable enough to provide an accurate velocity model (Herron, 2000; Gray et al., 2001; Glogovsky et al., 2002). Therefore, current imaging methods generally lose their capability of clearly imaging the subsurface structure in those geologically complex regions.

To summarize, current traditional multiple removal algorithms and imaging algorithms work effectively only when subsurface information (for example, earth structure, subsurface velocity model, etc.) are provided accurately. But when such a priori information are not accurate or even inaccessible for geologically complex conditions, the traditional methods break down. The solution to the pressing challenges arising from current seismic exploration is either to improve the conventional methods by decreasing their demand for sufficient subsurface information, or to avoid the assumptions of using subsurface information innate in conventional methods, by developing a new set of seismic data processing methods which do not make those assumptions.

The inverse scattering theory takes the second approach and provides a stand-alone solution for addressing the current pressing seismic challenges. The formalism of inverse scattering series was first introduced in Weglein et al. (1981). The inverse scattering series provides the unique potential and promise of achieving all seismic processing objectives directly in terms of measured data (and water speed) without requiring, needing or determining in principle or practice, subsurface information, e.g., velocity, structure, etc., that traditional processing methods require (Weglein et al., 2003).

In the following section, I will give an introduction to the background and history of the inverse scattering theory and series and the successful seismic application of inverse scattering series to address the pressing challenges discussed in this section.

1.2 Inverse scattering series

Scattering theory is a form of perturbation analysis. It was proposed and discussed by physicists and mathematicians (Jost and Kohn, 1952; Morse and Feshbach, 1953; Razavy, 1975), and then introduced into the field of seismic exploration (Weglein et al., 1981; Weglein, 1985; Weglein et al., 2003). Generally speaking, scattering theory describes how a perturbation in the properties of a medium relates to a wavefield that experiences that perturbed medium. Let's start with two general differential equations governing wave propagation in these media:

$$LG = \delta(\mathbf{r} - \mathbf{r_s}), \tag{1.1}$$

$$L_0 G_0 = \delta(\mathbf{r} - \mathbf{r_s}). \tag{1.2}$$

where L, L_0 are the actual and reference differential operators, respectively, which can be expressed in different forms depending on the properties of the actual and reference media e.g. homogeneous or inhomogeneous, acoustic or elastic or inelastic, one parameter or multi-parameter. Several specific examples of the two operators are given in Weglein et al. (2003). G, G_0 are two Green's functions (wave fields) in actual and reference media, respectively, and represent a response to a Dirac delta function $\delta(\mathbf{r} - \mathbf{r_s})$. $\mathbf{r}$ and $\mathbf{r_s}$ are the field point and source location, respectively.

The Lippmann-Schwinger equation is an integral solution to the wave equation (1.1) by using the reference wave equation (1.2) and defining a perturbation operator as $V = L_0 - L$ (perturbation operator is defined as the properties difference between the reference medium and the actual medium),

$$\Psi_s = G - G_0 = G_0 V G \tag{1.3}$$

where Ψ_s is the scattered field, i.e., the difference between actual wave field and the reference wave field.

The total scattered field is related to the earth perturbation and the reference wave field (generally using water as reference background for marine seismic exploration) by the above recursive integral form of Lippmann-Schiwinger equation.

Expanding equation (1.3) by iterating (Taylor, 1972), a forward scattering series is obtained,

$$\Psi_s = G_0 V G_0 + G_0 V G_0 V G_0 + \cdots \tag{1.4}$$

$$= (\Psi_s)_1 + (\Psi_s)_2 + \cdots , \tag{1.5}$$

where $(\Psi_s)_n$ is the portion of Ψ_s that is n^{th} order in V. The measured value of Ψ_s is the data, D, where $D = (\Psi_s)_{ms} = (\Psi_s)_{\text{on the measurement surface}}$.

The forward scattering series provides an ability to model the data since the perturbation V underneath the measurement surface has been assumed known in the forward problem (Matson, 1996).

To obtain an inverse scattering series (ISS) from the above forward series, an important assumption is introduced: expanding the perturbation operator V in orders of data D yields (Weglein et al., 1997),

$$V = V_1 + V_2 + V_3 + \cdots \tag{1.6}$$

where V_n is n^{th} order in the data D.

An inverse scattering series is obtained by substituting equation (1.6) in equation (1.4) and setting the same order of the data equal on both sides of the resulting equation at the measurement surface,

$$\begin{aligned} D &= [G_0 V_1 G_0]_{ms}, && (1.7)\\ 0 &= [G_0 V_2 G_0]_{ms} + [G_0 V_1 G_0 V_1 G_0]_{ms}, && (1.8)\\ 0 &= [G_0 V_3 G_0]_{ms} + [G_0 V_1 G_0 V_2 G_0]_{ms} \\ &+ [G_0 V_2 G_0 V_1 G_0]_{ms} + [G_0 V_1 G_0 V_1 G_0 V_1 G_0]_{ms}, && (1.9)\\ &\vdots \end{aligned}$$

where $\vdots$ denotes more higher order inverse scattering series equations.

To solve the above inverse scattering series, one can invert both sides of V_1 in equation (1.7), so V_1 can be expressed directly in terms of recorded data D and the

reference wave field G_0. Then substitute the result of V_1 into the 2^{nd} order equation (1.8), and solve V_2 in terms of data and the reference wave field. The other higher order of V can be solved order by order.

So, the inverse scattering series provides a direct multi-dimensional method for obtaining the subsurface configuration information (earth structure and material property) by inverting the series order by order to solve for the perturbation V, only using the measured data, D, and a reference wave field, G_0. Since the inverse scattering series is an infinite series, the convergence of this series was a concern and is fully discussed in Prosser (1969, 1976, 1980, 1982) and Carvalho (1992). These papers demonstrated that the full inverse scattering series converges for a small range of models. Then a natural question might be raised: what value does the inverse scattering series have for seismic exploration since it is divergent for a real contrast in perturbations? To answer this question, Weglein et al. (1997, 2003) proposed and developed, for the first time, a new understanding for the implementation of inverse scattering series into seismology: task separation and task-specific inverse scattering subseries.

The main idea of task separation is that the inverse scattering series can be isolated into subseries corresponding to each separated task objective, and when each task completes, the next task will start with *new data*[5] using an isolated subseries for that individual task. Under the inverse scattering formalism, seismic data can be inverted through four separate processing tasks to achieve different objective at each stage: (1) removal of free surface multiples; (2) removal of internal multiples; (3)

[5]Here "new data" denotes that the original data set has been processed and updated by individual task , for example a data set after elimination of free surface multiple etc.

migration of primaries to corresponding reflectors (imaging); (4) amplitude analysis of migrated primaries for property changes (inversion). A detailed overview of inverse scattering series regarding how individual tasks are separated and how each task-specific subseries is isolated and implemented to seismic processing, is presented and discussed in Weglein et al. (2003). This dissertation narrows its mission to demonstrate work in the task of internal multiple removal and imaging without a velocity model.

Up to now, the M-OSRP[6] research group has explored, developed and delivered to the oil industry a set of successful task-specific algorithms using inverse scattering subseries to address current pressing seismic exploration challenges. The first successful implementation of an isolated subseries was free surface multiple removal using ISS. All free surface multiples of a specified order are removed in frequency domain. Successful intial test on field data demonstrated the convincing strength of ISS isolated free surface multiple removal subseries (Carvalho, 1992; Weglein et al., 1997, 2003).

The second isolated subseries to remove internal multiples was first identified by Araújo (1994), and it was initially tested on field data by Coates and Weglein (1996) and Weglein and Matson (1998). The ISS acoustic internal multiple attenuator[7] was further extended to the attenuation of elastic internal multiples by using

[6]M-OSRP stands for Mission-Oriented Seismic Research Program, a consortium intiated and directed by Arthur Weglein in the Department of Physics at the University of Houston.

[7]This algorithm is called as an attenuator since it accurately predicts the arrival times of all the leading order internal multiples, but approximate their amplitude. More details regarding the attenuator algorithm will be discussed in Chapter 2 of this dissertation.

multi-component land and ocean-bottom dataset by Matson (1997). The ISS internal multiple attenuator also demonstrated its strength in a multi-D earth (Nita and Weglein, 2005). To remove the predicted internal multiple with approximated amplitude using this ISS internal multiple attenuator, an adaptive subtraction method can be employed to subtract the prediction from the original dataset. Minimum energy criterion method is the most widely used adaptive subtraction technique in today's seismic data processing industry. However, the principle of this method, using a matched filter to subtract the prediction from the original data, leads to a minimun of energy and usually works for data with multiples not interfering with or not proximal to primaries. In the cases of interfering multiples-primaries, the method of minimum energy subtraction can seriously harm the dataset by distorting primaries embedded in it. To avoid this processing dilemma, an eliminator rather than the attenuator of ISS internal multiples was identified. Ramírez and Weglein (2005), Herrera et al. (2012), and Zou and Weglein (2014) developed an ISS internal multiple eliminator for a 1D earth. The accurate prediction of all the leading order internal multiples with exact amplitude for all reflectors make the elimination of all internal multiples through a simple direct subtraction, and the most remarkable result from the eliminator is that the invisible primaries originally obscured by internal multiples, emerge from the dataset after the direct subtraction. In addition, spurious events can be generated due to the mechnism of combining of internal multiple as subevents by a spatial "lower-higher-lower" relationship in the ISS internal multiple attenuator algorithm, and they cause problems for the leading order attenuator. A new higher-order attenuator to address spurious events based on the leading order

internal multiple attenuator was proposed and tested by Liang and Weglein (2012) and Ma and Weglein (2014).

Note that both the ISS free-surface multiple and internal multiple eliminator/attenuator algorithms are driven by water-speed migrated input data, without using or searching for any subsurface information other than recorded seismic data and a reference medium. Both algorithms are model type independent, which means effectiveness stays the same and no code is changed regardless of whether the medium is homogeneous or heterogeneous, isotropic or anisotropic, acoustic, elastic, or anelastic (Weglein et al., 2003). The derivations of ISS algorithms, in principle, take reference medium in accordance with the medium where seismic source and receivers are situated. This choice of reference medium restricts all of the perturbation V under the measurement surface, and makes calculations much simpler than the case of the perturbation on both sides of the measurement surface. In marine case, we choose water as reference background, but for onshore case, the near surface properties are generally heterogeneous and complicated. Research was initiated in M-OSRP (Hsu and Weglein, 2008; Hsu et al., 2009) to investigate the sensitivity of ISS internal multiple attenuator algorithm to reference velocity for both offshore and onshore data processing[8]. Through both analytic calculation and synthetic tests, the researchers verified and concluded that the ISS internal multiple attenuator is insensitive to the reference velocity used in the algorithm while still accurately predicting the exact arrival times of all internal multiples with approximated reflection amplitudes. A

[8]Internal multiples are the predominant issue for land case, while free surface multiples are the main issue to address for marine case.

partial contribution and a detailed analysis on this research topic for elastic application constitute part of this dissertation and is presented in Chapter 2.

After the task of internal multiple removal, imaging and inversion are the next processes, respectively. Weglein et al. (2000) first proposed a scheme using ISS to perform the tasks of spatially locating subsurface reflectors and directly inverting the earth properties without knowing the subsurface velocity or any other medium property information below the measurement surface, by calculating the ISS order by order in the recorded data and using a constant velocity reference medium. The authors also identified that the first ISS term is a constant velocity $f-k$ migration of the original dataset, and the calculation of the second ISS term leads to a separation of "inversion-only" term and "imaging-only" term[9] . Following the formalism and scheme of Weglein et al. (2000), a leading order ISS imaging subseries (abbreviated as LOIS) was first identified, analyzed, and initially tested for a 1D velocity-only change acoustic medium (Weglein et al., 2002; Shaw et al., 2002; Shaw and Weglein, 2003). The authors verified the LOIS algorithm is actually a Taylor series expanded over the pseudodepth by a constant reference velocity migration of the input data. The LOIS can be written as a closed form, so it has no convergence problem. For small velocity contrast medium, addition of LOIS subseries up to a number of orders can move the mislocated interfaces toward their correct positions. LOIS algorithm uses amplitude information in the data and a constant reference velocity to image subsurface reflectors. The issues of low-frequency missing in the data were also fully

[9]Imaging-only term means this kind of term survives only when mislocated reflectors exist due to velocity change in the medium. This term will be further discussed in detail in Chapter 3 of this dissertation.

investigated (Shaw et al., 2003; Shaw and Weglein, 2004; Shaw, 2005): tapered low-frequencey data impacts the LOIS imaging capability to some extent[10]. The issue of limited imaging competence of the LOIS is due to its limited collection of imaging-only terms (only leading order in the reflection data) in each ISS term. So a research effort was taken in M-OSRP to capture more imaging terms: Innanen and Weglein (2003) isolated a subseries by capturing more terms with simultaneous imaging and inversion tasks in one algorithm. Following this work, Liu et al. (2004, 2005) and Liu (2006) intuitively[11]identified a new multi-D higher order ISS imaging algorithm (called HOIS) and largly improved the ISS imaging capability for a large velocity contrast acoustic medium in the presence of lateral variation. This was done by flipping the imaging-shifting arguments from the right-hand side of the identity to the left-hand side, and by excluding the imaging algorithm's "communication" with deeper events than the imaged point. With more higher order imaging-only terms captured, ISS imaging algorithms can produce a better imaging. Based on Liu's HOIS work, a set of higher order imaging algorithms were proposed in Wang (2011): the HHOIS (for higher and higher order imaging subseries) imaging algorithm works better than HOIS for even larger velocity contrast and velocity error duration. The RHOIS (for recursive higher order imaging subseries) uses a recursive method for iterating the initial input imaging result back into the algorithm itself to correct the mislocated reflectors. The HOIS-LE (representing higher order imaging subseries with lateral exclusive) improves the salt-model imaging result by absorbing more

[10]The issue of low frequency missing has been well addressed by data regularization methods developed in Liu et al. (2010) andLiu and Weglein (2011).

[11]HOIS subseries actually composes more higher-order imaging terms than LOIS, which was mathematically verified by Wang (2011)

diffraction energy to correct sharp lateral variation imaging.

To apply the imaging algorithms developed by M-OSRP to field seismic data, the one-parameter (constant density but variable velocity) imaging algorithms must be progressed to multi-paramter (variation in more than velocity parameter) ones. Zhang and Weglein (2003, 2004) generalized Weglein et al. (2002) from 1D acoustic medium with velocity change only to a 1D multi-parameter acoustic and elastic medium, and identified a nonlinear inversion subseries in the second ISS term. Meanwhile, the imaging-only terms in the second order ISS term for the multi-parameter case were also identified, and were later rewritten as an "imaging composite" by Weglein (Jiang and Weglein, 2008), leading to Weglein's "multi-parameter imaging conjecture". This conjecture addressed the issue of how many parameters and which parameter should be imaged for a multi-parameter medium. The analytic derivation of α_3, β_3 ISS terms for a two-parameter acoustic medium led to identifying an imaging algorithm and justified the "multi-parameter imaging conjecture" (Jiang and Weglein, 2008; Jiang et al., 2009). The initial analytical and synthetic tests demonstrated the imaging strength of the multi-parameter ISS imaging algorithms (more details are presented in Chapter 3 of this dissertation.) Later, Wang (2011) captured partial imaging-only terms of β_3 in Jiang's calculation result to obtain a "beyond conjecture HOIS" algorithm which improved the multi-parameter imaging capability for even larger parameter contrast and velocity error duration. Li (2011) tested elastic version of the multi-parameter imaging conjecture, and the first encouraging field data test on the Kristin field dataset warranted field application of the multi-parameter imaging algorithm. Readers interested in more details of the

updates and progress of M-OSRP's imaging project can refer to Weglein et al. (2011).

This dissertation will focus on two topics within the above frame of research: internal multiple attenuation and multi-parameter acoustic imaging. In the next section, an overview of this dissertation will be presented.

1.3 Dissertation overview

Chapter 1 of this dissertation provided a brief introduction to general seismic exploration with processes, methods and challenges. The inverse scattering series and its application in seismic exploration were then described and discussed to address the challenges.

Chapter 2 will present the investigation of the sensitivity of 1D ISS internal multiple attenuation (IMA) algorithm to reference velocity for land application. The general steps of how to identify an ISS IMA for multi-component (compressional - P, and shear - S) PP, PS, SP and SS data will be discussed. Followed these steps, the theoretical calculation of the ISS IMA will be provided for a 1D-layered elastic earth to analyze the algorithm's sensitivity to reference velocities (V_p and V_s). Both normal and non-normal incident cases will be calculated and discussed. The numerical tests on IMA for isotropic acoustic, acoustic over elastic, anisotropic VTI, and elastic medium with wrong reference velocity will also be presented to demonstrate the value of its land application.

Chapter 3 will be devoted to describing the research on ISS multi-parameter

imaging for a 1D acoustic medium with both velocity and density variation. The logic of imaging conjecture will be analyzed and justified by presenting an analytic calculation result of α_3 and β_3 terms for the two-parameter case. This chapter will also provide the analytic evaluation and synthetic tests of the multi-parameter LOIS and HOIS algorithms on different acoustic models, to test the imaging capability of both algorithms. The algorithms' imaging strengths will be compared, and the existing issues will be analyzed and discussed at the end of the chapter.

The last chapter will give a summary on the research documented in this dissertation.

Chapter 2

Elastic internal multiple attenuation using inverse scattering series

2.1 Chapter overview

In section 1, I will first briefly introduce general steps of how to identify an inverse scattering series (*ISS*) internal multiple attenuator (*IMA*) for elastic case. In section 2, a 1D elastic IMA will then be calculated to prove its insensitivity to reference velocities (V_p and V_s). Analytical elastic data will be prepared for the algorithm to predict the 1^{st} order internal multiples for a 1D 3-layer elastic medium at both normal incidence case and non-normal incidence cases. In the following section, a series of numerical examples will first demonstrate 1D acoustic IMA can

be successfully implimented to acoustic over elastic isotropic and anisotropic VTI media, and then show the successful prediction with correct and incorrect p-wave reference velocities for the 1^{st} order internal multiples by using multi-component geophone dataset. A conclusion will be presented in the last section of this chapter.

2.2 Introduction to elastic internal multiple attenuation

The leading order ISS internal multiple attenuation algorithm was first proposed and tested on field data by Araújo (1994) and Weglein et al. (1997), and later was progressed into multi-component data in elastic media by Matson (1997). In this section, I will focus on the key points and some basic workflow of Matson's derivation of elastic IMA, to help understand why it automatically predicts the arrival time of internal multiples in land seismic data.

To identify an elastic ISS IMA basically follows the same steps in calculating the acoustic IMA (Araújo, 1994; Coates and Weglein, 1996; Weglein et al., 1997). Here, I only introduce the identification steps for the 1^{st} order elastic IMA, since all higher orders of IMA follow the same steps:

1. Calculate $D = (G_0 V_1 G_0)_{m.s.}$;

2. Define the given quantity B_1 referring to an incident plane wave, using the measured data D;

3. Select V_{33} from the ISS 3^{rd} order term $(G_0V_1G_0V_1G_0V_1G_0)_{m.s.}$ by restricting the integral intervals according to the "lower-higher-lower" geometry relation (the 1^{st} order internal multiple spatial geometry);

4. Calculate V_{33} using contour integration and residue theorem;

5. Define the given quantity, B_3, corresponding to V_{33};

6. Calculate B_{33} as a portion of B_3 expressed as the "lower-higher-lower" integral in depth;

7. B_{33} is the ISS IMA of the 1^{st} order.

Next, I will follow the above steps to briefly go through the logic of deriving the elastic version of IMA. For elastic case, the first ISS term is expressed as a linear relation between perturbation and multi-component data (PP, PS, SS and SP data).

$$\hat{D}_{ij} = \hat{G}_{0i}\hat{V}_{ij}^{(1)}\hat{G}_{0j}. \tag{2.1}$$

where $i, j = P, S$, $\hat{V}_{ij}^{(1)}$ is the 1^{st} order perturbation operator in the elastic medium, and G_{0i}, G_{0j} are P wave or S wave causal reference Green's functions without free surface:

$$G_{0i}(x_g, z_g|x_s, z_s; \omega) = \frac{1}{2\pi}\int_{-\infty}^{\infty}\frac{1}{2i\theta_{1i}}e^{ik(x_g-x_s)}e^{i\theta_{1i}|z_s-z_g|}dk. \tag{2.2}$$

x_s and x_g are horizontal position of the source and the geophone; z_s and z_g denote source and geophone depth, respectively. For P wave and S wave, the vertical wave number θ_{1i} is defined respectively as,

$$\theta_{1i} = \mu = sign(\omega)\sqrt{\frac{\omega^2}{\alpha^2} - k^2}. \tag{2.3}$$

$$\theta_{1i} = \eta = sign(\omega)\sqrt{\frac{\omega^2}{\beta^2} - k^2}. \tag{2.4}$$

where k is the horizontal wave number, α and β correspond to P-wave and S-wave velocities in reference medium, respectively.

Inserting the above Green's function into the integral equation (2.1) and executing a Fourier transform, the multi-component data can be expressed in the (k, ω) domain as,

$$D_{ij}(k_1, z_g|k_2, z_s; \omega) = \frac{1}{2i\theta_{1i}} e^{-i\theta_{1i} z_g} V_{ij}^{(1)}(k_1, k_2, \theta_{1i} + \theta_{2j}) \frac{1}{2i\theta_{2j}} e^{-i\theta_{2j} z_s}. \tag{2.5}$$

Now the incident plane wave B_1 in the elastic case can be defined as,

$$\begin{aligned} B_{ij}^{(1)}(k_1, k_2, \theta_{1i} + \theta_{2j}) &= -\frac{1}{2i\theta_{1i}} e^{-i\theta_{1i} z_g} V_{ij}^{(1)}(k_1, k_2, \theta_{1i} + \theta_{2j}) e^{-i\theta_{2j} z_s} \\ &= -2i\theta_{2j} D_{ij}(k_1, z_g|k_2, z_s; \omega) \end{aligned} \tag{2.6}$$

As mentioned in the steps, the first order internal multiple starts from the third term in the ISS,

$$\begin{aligned} V_{ij}^{(33)}(k_1, k_2, \theta_{1i} + \theta_{2j}) = \widetilde{\int_{-\infty}^{\infty}} d\tilde{\mathbf{r}} e^{-ik_1 x_1} e^{i\theta_{1i} z_2} V_{il}^{(1)}(x_1, x_2, z_2) G_{0l}(x_2, z_2|x_3, z_4; \omega) \\ V_{lm}^{(1)}(x_3, x_4, z_4) G_{0m}(x_4, z_4|x_5, z_6; \omega) V_{mj}^{(1)}(x_5, x_6, z_6) e^{i\theta_{2j} z_6} e^{ik_2 x_6} \end{aligned} \tag{2.7}$$

So, the plane-wave incident quantity B_3 now is defined as,

$$B_{ij}^{(3)}(k_1, k_2, \theta_{1i} + \theta_{2j}) = -\frac{1}{2i\theta_{1i}} e^{-i\theta_{1i} z_g} V_{ij}^{(33)}(k_1, k_2, \theta_{1i} + \theta_{2j}) e^{-i\theta_{2j} z_s} \tag{2.8}$$

Finally, as a portion of the above B_3 quantity with spatial integration of "lower-higher-lower" relation, the 1^{st} order elastic internal multiple prediction is (Matson,

1997),

$$
\begin{aligned}
B_{ij}^{(3)IM}(k_1,k_2,\theta_{1i}+\theta_{2j}) =& \frac{1}{(2\pi)^2}\int_{-\infty}^{\infty} dk_3 e^{-i\theta_{3l}(z_g-z_s)} \int_{-\infty}^{\infty} dk_4 e^{i\theta_{4m}(z_g-z_s)} \\
& \cdot \int_{-\infty}^{\infty} dz_1 B_{il}^{(1)}(k_1,k_3,z_1) e^{i(\theta_{1i}+\theta_{3l})z_1} \\
& \cdot \int_{-\infty}^{z_1-\epsilon} dz_2 B_{lm}^{(1)}(k_3,k_4,z_2) e^{-i(\theta_{3l}+\theta_{4m})z_2} \\
& \cdot \int_{z_2+\epsilon}^{\infty} dz_3 B_{mj}^{(1)}(k_4,k_2,z_3) e^{i(\theta_{4m}+\theta_{2j})z_3}
\end{aligned}
\tag{2.9}
$$

The above 1^{st} order elastic IMA is a data-driven algorithm: it automatically reconstructs the 1^{st} order internal multiples using sub-events which are three primary events following the "lower-higher-lower" pseudo-depth[1] spatial relationship as indicated by the integral variables z_1, z_2 and z_3 (see figure 2.1). Here, the small variable ϵ is used to ensure the spatial relationship. It generally takes the value of width of wavelet in numerical implementation for a band limited dataset. The ISS elastic IMA algorithm accurately predicts the travel times of all internal multiples at one time through data convolution and cross-correlation. Since each leg of the predicted internal multiple can be either P or S, the elastic attenuator suggests that the prediction of the 1^{st} order internal multiples needs multicomponent data, $B_{ij}^{(1)}$ in equation (2.6). When the reference is changed into acoustic medium, the elastic IMA formula, equation (2.9), will be reduced to a simple version, the 1^{st} order acoustic IMA

[1]Pseudo-depth in ISS-based algorithms is the imaged depth by doing a f-k migration on seismic data using a constant reference velocity (usually water speed $1500m/s$). This is generally a standard procedure to prepare the input data for ISS-based algorithms.

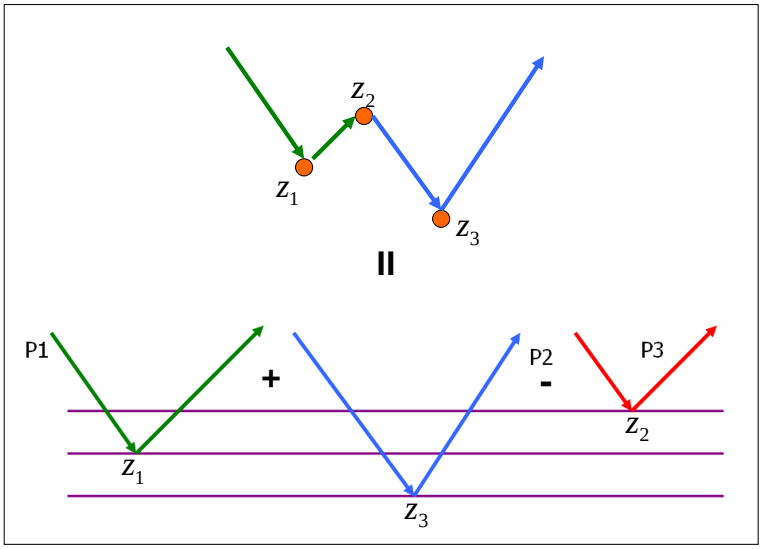

Figure 2.1: *A cartoon picture demonstrating the mechanism of the* 1^{st} *order elastic IMA : two deeper primaries and one shallower primary controlled by pseudo-depths are used to construct all* 1^{st} *order internal multiples in one step. The total arrival time of the predicted internal multiple is the sum of two deeper primaries' arrival times subtracted by one shallower primary event's arrival time.*

(Araújo, 1994; Weglein et al., 1997):

$$b_3(k_g,k_s,\omega) = \frac{1}{(2\pi)^2}\int_{-\infty}^{\infty} dk_1 e^{-iq_1(z_g-z_s)} \int_{-\infty}^{\infty} dk_2 e^{iq_2(z_g-z_s)} \int_{-\infty}^{\infty} dz_1 e^{i(q_g+q_1)z_1} b_1(k_g,k_1,z_1) \cdot \int_{-\infty}^{z_1-\epsilon} dz_2 e^{i(-q_1-q_2)z_2} b_1(k_1,k_2,z_2) \int_{z_2+\epsilon}^{\infty} dz_3 e^{i(q_2+q_s)z_3} b_1(k_2,k_s,z_3) \tag{2.10}$$

2.3 Reference velocity insensitivity of the 1D elastic IMA

In the previous introduction section, the elastic IMA algorithm is identified step by step. A key point during the derivation of the IMA is that the reference background must agree with the actual medium at sources and receivers so as to keep all perpurbation below measurement surface[2].

However, in practice of seismic exploration, the medium property where acquisition surface locates is different between marine cases and land cases. The former one is an acoustic homogeneous water column, while the latter is an elastic heterogeneous layer with generally variable properties. Due to near-surface complexity on land, it is often difficult to accurately estimate the near-surface P-wave and S-wave velocities, and hence hard to provide the correct reference velocity for the IMA. So the scattered field will be different and the perturbation will exist on both sides of the measurement surface. Strictly speaking, the elastic IMA algorithm should be rederived, but the new algorithm will be more complicated.

The ISS IMA predicts the arrival times of internal multiples without knowing subsurface information. Ken Matson's elastic IMA was synthetically tested with correct P-wave and S-wave reference velocities in near surface. Results showed it works robustly, given P- and S- multicomponent data (Matson, 1997). If given an

[2]This is a convention that when we when derive all ISS algorithms, we assume knowing the medium above acquisition surface to constrain perturbation. With this assumption, the reference Green's function will be much simpler to write down and hence calculation is much more simplified, than the case of keeping purturbation on both sides of the measurement surface.

approximate incorrect near-surface velocity as the reference velocity, how robustly will the elastic IMA work? In this section, I will make theoretical analysis of the IMA on two analytic cases to investigate whether the 1D elastic IMA is sensitive to reference velocity. The first part is to consider a 1D normal incidence case, and the second part is 1D non-normal incidence.

2.3.1 Analytic analysis (part I): 1D normal incidence

First, for a 1D normal incidence case, the elastic IMA is simplified to be,

$$\begin{aligned} B_{ij}^{(3)IM}(\theta_{1i}+\theta_{1j}) =& \frac{1}{(2\pi)^2}\int_{-\infty}^{\infty} dz_1^{'} B_{il}^{(1)}(z_1^{'}) e^{i(\theta_{1i}+\theta_{1l})z_1^{'}} \\ & \int_{-\infty}^{z_1^{'}-\epsilon} dz_2^{'} B_{lm}^{(1)}(z_2^{'}) e^{-i(\theta_{1l}+\theta_{1m})z_2^{'}} \\ & \int_{z_2^{'}+\epsilon}^{\infty} dz_3^{'} B_{mj}^{(1)}(z_3^{'}) e^{i(\theta_{1m}+\theta_{1j})z_3^{'}} \end{aligned} \tag{2.11}$$

Multicomponent effective data need to be prepared for the prediction of the 1^{st} order internal multiples.

To begin with, let's prepare analytic data in the time domain for the normal incidence case,

$$D_{mj}(t) = \sum_n \tilde{R}_n \delta(t - t_n) \tag{2.12}$$

where t_n and $\tilde{R}_n$ are the arrival time and amplitude of the n^{th} seismic event, respectively. Both reflection and transmission coefficients are included in $\tilde{R}_n$ for refracted and reflected events.

The analytic multicomponent data can now be expressed in the frequency domain by conducting a Fourier transform over t, then the data can be rescaled by a reference

velocity c_0^{mj}:

$$D_{mj}(\omega) = \sum_n \tilde{R}_n e^{i\omega t_n} \tag{2.13}$$

$$D_{mj}\left(\frac{2\omega}{c_0^{mj}}\right) = \sum_n \tilde{R}_n e^{i\frac{2\omega}{c_0^{mj}}\cdot\frac{c_0^{mj}t_n}{2}} = \sum_n \tilde{R}_n e^{ik_0^{mj}\cdot z_n^{mj}} \tag{2.14}$$

where,

$$k_0^{mj} = \frac{2\omega}{c_0^{mj}} = \theta_{1m} + \theta_{1j} \tag{2.15}$$

$$z_n^{mj} = \frac{c_0^{mj} t_n}{2} \tag{2.16}$$

$$\theta_{1m} = \sqrt{\left(\frac{\omega}{\alpha_0}\right)^2 - k_1^2} \tag{2.17}$$

$$\theta_{1m} = \sqrt{\left(\frac{\omega}{\beta_0}\right)^2 - k_1^2} \tag{2.18}$$

c_0^{mj} is the reference velocity, which does not need to be the correct near-surface velocity in this research. θ_{1m} and θ_{1j} are two vertical wave numbers of the P-wave (with velocity as α_0) or S-wave (with velocity as β_0) in the reference medium. z_n^{mj} is the corresponding pseudo-depth with such a reference velocity.

Now we can define the multicomponent effective data by using the above analytic multicomponent data in the wave-number domain, and then perform an inverse Fourier transform to express it in the pseudo-depth domain.

$$B_{mj}^{(1)}(k_0^{mj}) = D_{mj}\left(\frac{2\omega}{c_0^{mj}}\right) = \sum_n \tilde{R}_n e^{ik_0^{mj}\cdot z_n^{mj}} \tag{2.19}$$

$$B_{mj}^{(1)}(z) = \frac{1}{2\pi}\int_{-\infty}^{\infty} B_{mj}^{(1)}(k_0^{mj}) e^{ik_0^{mj} z} dk_0^{mj}. \tag{2.20}$$

$$B_{mj}^{(1)}(z) = \frac{1}{2\pi} \sum_{n} \tilde{R}_n \delta(z - z_n^{mj}) \tag{2.21}$$

Clearly, $B_{mj}^{(1)}(z)$ is a series of spikes of plane-wave incidence as required by the algorithm.

By performing a similar procedure, the other two components of effective data can also be written down immediately as,

$$B_{lm}^{(1)}(z) = \frac{1}{2\pi} \sum_{n'} \tilde{R}_{n'} \delta(z - z_{n'}^{lm}) \tag{2.22}$$

where,

$$k_0^{lm} = \frac{2\omega}{c_0^{lm}} = \theta_{1l} + \theta_{1m} \tag{2.23}$$

$$z_{n'}^{lm} = \frac{c_0^{lm} t_{n'}}{2} \tag{2.24}$$

$$c_0^{lm} = \frac{2\omega}{\theta_{1l} + \theta_{1m}} \tag{2.25}$$

and,

$$B_{il}^{(1)}(z) = \frac{1}{2\pi} \sum_{n''} \tilde{R}_{n''} \delta(z - z_{n''}^{il}) \tag{2.26}$$

where,

$$k_0^{il} = \frac{2\omega}{c_0^{il}} = \theta_{1i} + \theta_{1l} \tag{2.27}$$

$$z_{n''}^{il} = \frac{c_0^{il} t_{n''}}{2} \tag{2.28}$$

$$c_0^{il} = \frac{2\omega}{\theta_{1i} + \theta_{1l}} \tag{2.29}$$

All the above prepared multicomponent effective data are inserted into the 1D

elastic IMA formula, equation (2.11), then the 1^{st} integral:

$$\begin{aligned}
&\int_{z_2^{'}+\epsilon}^{\infty} dz_3^{'} B_{mj}^{(1)}(z_3^{'}) e^{i(\theta_{1m}+\theta_{1j})z_3^{'}} \\
&= \int_{-\infty}^{\infty} dz_3^{'} H(z_3^{'} - z_2^{'} - \epsilon) \cdot \left[\frac{1}{2\pi} \sum_n \tilde{R}_n \delta(z_3^{'} - z_n^{mj}) \right] e^{i(\theta_{1m}+\theta_{1j})z_3^{'}} \\
&= \frac{1}{2\pi} \sum_n \tilde{R}_n H(z_n^{mj} - z_2^{'} - \epsilon) e^{i(\theta_{1m}+\theta_{1j})z_n^{mj}}
\end{aligned} \tag{2.30}$$

the 2^{nd} integral:

$$\begin{aligned}
&\int_{-\infty}^{z_1^{'}-\epsilon} dz_2^{'} B_{lm}^{(1)}(z_2^{'}) e^{-i(\theta_{1l}+\theta_{1m})z_2^{'}} \cdot \frac{1}{2\pi} \sum_n \tilde{R}_n H(z_n^{mj} - z_2^{'} - \epsilon) e^{i(\theta_{1m}+\theta_{1j})z_n^{mj}} \\
&= \int_{-\infty}^{\infty} dz_2^{'} H\left(z_1^{'} - \epsilon - z_2^{'}\right) \cdot \left[\frac{1}{2\pi} \sum_{n'} \tilde{R}_{n'} \delta(z_2^{'} - z_{n'}^{lm}) \right] e^{-i(\theta_{1l}+\theta_{1m})z_2^{'}} \\
&\cdot \frac{1}{2\pi} \sum_n \tilde{R}_n H(z_n^{mj} - z_2^{'} - \epsilon) e^{i(\theta_{1m}+\theta_{1j})z_n^{mj}} \\
&= \frac{1}{(2\pi)^2} \sum_{n,n'} \tilde{R}_{n'} \tilde{R}_n H(z_1^{'} - \epsilon - z_{n'}^{lm}) H(z_n^{mj} - z_{n'}^{lm} - \epsilon) e^{-i(\theta_{1l}+\theta_{1m})z_{n'}^{lm}} e^{i(\theta_{1m}+\theta_{1j})z_n^{mj}}
\end{aligned} \tag{2.31}$$

The final prediction after the 3^{rd} integral is,

$$\begin{aligned}
B_{ij}^{(3)IM}(\theta_{1i}+\theta_{1j}) =& \frac{1}{(2\pi)^5} \sum_{m,l} \sum_{n,n',n''} \tilde{R}_{n''} \tilde{R}_{n'} \tilde{R}_n H(z_{n''}^{il} - z_{n'}^{lm} - \epsilon) H(z_n^{mj} - z_{n'}^{lm} - \epsilon) \\
&\cdot e^{i(\theta_{1i}+\theta_{1l})z_{n''}^{il}} e^{-i(\theta_{1l}+\theta_{1m})z_{n'}^{lm}} e^{i(\theta_{1m}+\theta_{1j})z_n^{mj}}
\end{aligned} \tag{2.32}$$

Let us discuss the Heaviside functions in the above prediction which control a "lower-higher-lower" spatial relationship among the combined sub-events by the three pseudo-depths $z_{n''}^{il}$, z_n^{mj}, and $z_{n'}^{lm}$. In another words, only the three sub-events

(three primaries) spatially satisfying the "lower-higher-lower" pseudo-depth relationship can constitute the predicted internal multiples of the 1^{st} order. Notice that the leading order internal multiples expressed in equation (2.32) are predicted at one time since the summation over all types of combination of P-leg and S-leg of sub-events satisfying spatial "lower-higher-lower" relationship. This is an amazingly powerful prediction.

Now we consider whether all the predicted 1^{st} order internal multiples have accurate arrival times. Let's examine the phase of the exponential functions in the prediction:

$$\begin{aligned} & e^{i(\theta_{1i}+\theta_{1l})z^{il}_{n''}} e^{-i(\theta_{1l}+\theta_{1m})z^{lm}_{n'}} e^{i(\theta_{1m}+\theta_{1j})z^{mj}_{n}} \\ & = e^{i(\theta_{1i}+\theta_{1l})\frac{t_{n''}}{2}\frac{2\omega}{\theta_{1i}+\theta_{1l}}} e^{-i(\theta_{1l}+\theta_{1m})\frac{t_{n'}}{2}\frac{2\omega}{\theta_{1l}+\theta_{1m}}} e^{i(\theta_{1m}+\theta_{1j})\frac{t_{n}}{2}\frac{2\omega}{\theta_{1m}+\theta_{1j}}} \end{aligned} \tag{2.33}$$

The equation analytically shows that all the reference velocities are cancelled out in the phase calculation, leaving predicted travel times independent of reference velocities. This is a surprising result which means the 1D elastic IMA has no difficulty in predicting different arrival times if we choose various incorrect reference velocities.

After performing an inverse Fourier transform over the prediction, equation (2.32) becomes,

$$\begin{aligned} B^{(3)IM}_{ij}(t) &= \frac{1}{2\pi}\int_{-\infty}^{\infty} B^{(3)IM}_{ij}(\omega)e^{-i\omega t}d\omega \\ &= \frac{1}{(2\pi)^6}\sum_{m,l}\sum_{n,n',n''} \tilde{R_{n'}}\tilde{R_{n''}}\tilde{R_n}H(z^{il}_{n''}-z^{lm}_{n'}-\epsilon)H(z^{mj}_{n}-z^{lm}_{n'}-\epsilon) \\ &\quad \cdot \delta\left[t-(t_{n''}+t_n-t_{n'})\right] \end{aligned} \tag{2.34}$$

This is the result of the prediction in time domain. In summary, the above analytic result proves that the 1D elastic IMA algorithm is independent of reference velocity

chosen and accurately predicts all the 1^{st} order internal multiples for the normal incidence case.

2.3.2 Analytic analysis (part II): 1D non-normal incidence

In this section, I will analytically prove that for 1D non-normal incidence case (see the layout of the experiment in figure 2.2), the 1D elastic IMA is also independent of reference velocity and predicts the accurate arrival times of all leading-order internal multiples.

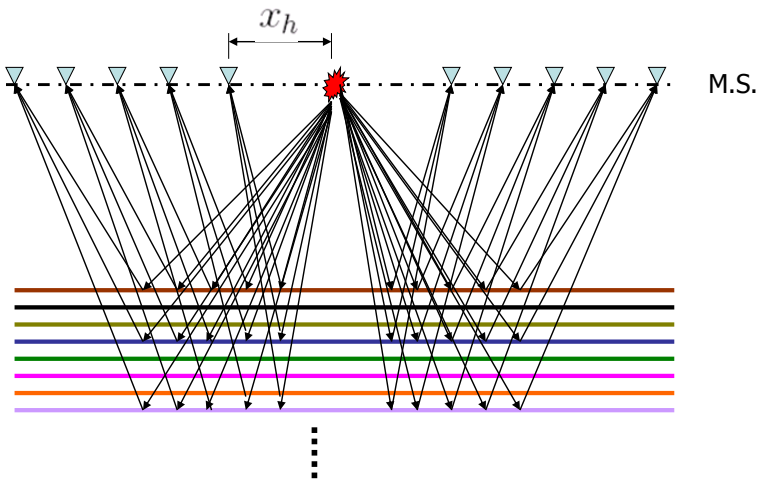

Figure 2.2: *A cartoon picture of the experiment layout for a 1D non-normal incidence elastic case: x_h is the offset between sources and geophones.*

For non-normal incidence case, the pre-stack analytical data is expressed as the following equation,

$$D_{mj}(x_h, 0; \omega) = \frac{1}{2\pi} \int_{-\infty}^{\infty} dk_h^{mj} \frac{\sum_n \tilde{R}_n^{mj} e^{i\omega t_n^v}}{iq_s^m} e^{ik_h^{mj} x_h} \tag{2.35}$$

where $\tilde{R}_n^{mj}$ is the n^{th} event amplitude including transmission and reflection coefficients, and t_n^v is the vertical travel-time of the n^{th} event, which satisfies the following relationship for primary events:

$$\omega t_n^v = \sum_{d=0}^{n} k_{z,d}^{mj}(z_d - z_{d-1}), d = 1, 2, 3, ...n \quad (z_0 \equiv 0) \tag{2.36}$$

where $k_{z,d}^{mj} = q_{g,d}^j + q_{s,d}^m$ is the vertical wavenumber for the real earth in the d^{th} layer with real depth at z_d. And $x_h = \frac{x_g - x_s}{2}$ is the source-receiver offset, and k_h^{mj} is its corresponding Fourier conjugate and expressed in the following equation,

$$k_h^{mj} = k_g^j + k_s^m = \sqrt{\left(\frac{\omega}{c_j}\right)^2 - \theta_{1j}^2} + \sqrt{\left(\frac{\omega}{c_m}\right)^2 - \theta_{1m}^2} \tag{2.37}$$

c_j and c_m are two real P-wave or S-wave velocities in the acquisition layer, θ_{1j} and θ_{1m} are two vertical wavenumbers in the measurement layer.

Performing an inverse Fourier transform over k_0^{mj} to define it in the pseudo-depth domain as,

$$B_{mj}^{(1)}(k_g, k_s, z) = \sum_n \tilde{R}_n^{mj} \delta(z - z_n^{mj}) \delta(k_g^j - k_s^m). \tag{2.38}$$

For 1D earth, $k_g^j = k_g = k_s^m = k_s$. We rewrite the above effective data as the following form to input into the IMA algorithm,

$$B_{mj}^{(1)}(k_4, k_2, z_3^{'}) = \sum_n \tilde{R}_n^{mj} \delta(z_3^{'} - z_n^{mj}) \delta(k_4 - k_2). \tag{2.39}$$

Following the similar procedure as above, we can define other component effective data as,

$$B_{il}^{(1)}(k_1, k_3, z_1^{'}) = \sum_{n^{'}} \tilde{R}_{n^{'}}^{il} \delta(z_1^{'} - z_{n^{'}}^{il}) \delta(k_1 - k_3). \tag{2.40}$$

where $z_{n^{'}}^{il} = \frac{c_0^{il} t_{n^{'}}^v}{2}$, $c_0^{il} = \frac{2\omega}{\theta_{1i} + \theta_{3l}}$, and,

$$\omega t_{n^{'}}^v = \sum_{d^{'}=0}^{n^{'}} k_{z,d^{'}}^{il} (z_{d^{'}} - z_{d^{'}-1}), d^{'} = 1, 2, 3, ...n^{'} \quad (z_0 \equiv 0). \tag{2.41}$$

And,

$$B_{lm}^{(1)}(k_3, k_4, z_2^{'}) = \sum_{n^{''}} \tilde{R}_{n^{''}}^{lm} \delta(z_2^{'} - z_{n^{''}}^{lm}) \delta(k_3 - k_4). \tag{2.42}$$

where $z_{n^{''}}^{lm} = \frac{c_0^{lm} t_{n^{''}}^v}{2}$, $c_0^{lm} = \frac{2\omega}{\theta_{3l} + \theta_{4m}}$, and,

$$\omega t_{n^{''}}^v = \sum_{d^{''}=0}^{n^{'}{}^{''}} k_{z,d^{''}}^{lm} (z_{d^{''}} - z_{d^{''}-1}), d^{''} = 1, 2, 3, ...n^{''} \quad (z_0 \equiv 0). \tag{2.43}$$

For 1D earth and $z_g = z_s$, the above multi-component effective data is inserted into the elastic IMA formula:

$$\begin{aligned} B_{ij}^{(3)IM}(k_1, k_2, \theta_{1i} + \theta_{2j}) = & \frac{1}{(2\pi)^2} \int_{-\infty}^{\infty} dk_3 \int_{-\infty}^{\infty} dk_4 \int_{-\infty}^{\infty} dz_1^{'} B_{il}^{(1)}(k_1, k_3, z_1^{'}) e^{i(\theta_{1i} + \theta_{3l}) z_1^{'}} \\ & \cdot \int_{-\infty}^{z_1^{'} - \epsilon} dz_2^{'} B_{lm}^{(1)}(k_3, k_4, z_2^{'}) e^{-i(\theta_{3l} + \theta_{4m}) z_2^{'}} \\ & \cdot \int_{z_2^{'} + \epsilon}^{\infty} dz_3^{'} B_{mj}^{(1)}(k_4, k_2, z_3^{'}) e^{i(\theta_{4m} + \theta_{2j}) z_3^{'}}. \end{aligned} \tag{2.44}$$

After using the same mathematical calculation as the normal incidence case, the

final result is:

$$\begin{aligned} B_{ij}^{(3)IM}(k_1,k_2,\theta_{1i}+\theta_{2j}) =& \frac{1}{(2\pi)^2}\sum_{m,l}\sum_{n,n',n''}\tilde{R}_{n'}^{il}\tilde{R}_{n''}^{lm}\tilde{R}_{n}^{mj} \\ & \cdot H\left(z_n^{mj}-z_{n''}^{lm}-\epsilon\right)H\left(z_{n'}^{il}-z_{n''}^{lm}-\epsilon\right)\delta(k_1-k_2) \\ & \cdot e^{i(\theta_{1i}+\theta_{1l})z_{n'}^{il}}e^{-i(\theta_{1l}+\theta_{1m})z_{n''}^{lm}}e^{i(\theta_{1m}+\theta_{1j})z_n^{mj}}. \end{aligned} \tag{2.45}$$

or,

$$\begin{aligned} B_{ij}^{(3)IM}(k_1,k_2,\theta_{1i}+\theta_{2j}) =& \frac{1}{(2\pi)^2}\sum_{m,l}\sum_{n,n',n''}\tilde{R}_{n'}^{il}\tilde{R}_{n''}^{lm}\tilde{R}_{n}^{mj} \\ & \cdot H\left(z_n^{mj}-z_{n''}^{lm}-\epsilon\right)H\left(z_{n'}^{il}-z_{n''}^{lm}-\epsilon\right)\delta(k_g-k_s) \\ & \cdot e^{i(\theta_{1i}+\theta_{1l})z_{n'}^{il}}e^{-i(\theta_{1l}+\theta_{1m})z_{n''}^{lm}}e^{i(\theta_{1m}+\theta_{1j})z_n^{mj}}. \end{aligned} \tag{2.46}$$

Now we will examine the predicted arrival times of all 1^{st} order internal multiples by calculating the phase in the above exponential functions. The pseudo-depths expression are substituted into it, then

$$\begin{aligned} & e^{i(\theta_{1i}+\theta_{1l})z_{n'}^{il}}e^{-i(\theta_{1l}+\theta_{1m})z_{n''}^{lm}}e^{i(\theta_{1m}+\theta_{1j})z_n^{mj}} \\ &= e^{i(\theta_{1i}+\theta_{1l})\frac{t_{n'}^v}{2}\frac{2\omega}{\theta_{1i}+\theta_{1l}}}e^{-i(\theta_{1l}+\theta_{1m})\frac{t_{n''}^v}{2}\frac{2\omega}{\theta_{1l}+\theta_{1m}}}e^{i(\theta_{1m}+\theta_{1j})\frac{t_n^v}{2}\frac{2\omega}{\theta_{1m}+\theta_{1j}}} \\ &= e^{i\omega\left(t_{n'}^v+t_n^v-t_{n''}^v\right)} \end{aligned} \tag{2.47}$$

In the above result, the reference velocities are cancelled out in the calculation of predicting the arrival times of the 1^{st} order internal multiples. This means that the vertical-travel times of predicted multiples are independent of reference velocities. This is same result seen in the normal incidence case.

The above result is inserted back to the final prediction result and a Fourier transform is performed over k_h to get the prestack version of the predicted internal

multiples as,

$$B_{ij}^{(3)pred_{IM}}(x_h,0;\omega) = \frac{1}{(2\pi)^3}\int_{-\infty}^{\infty} dk_h^{ij}\frac{e^{ik_h^{ij}x_h}}{iq_s}\cdot\sum_{m,l}\sum_{n,n',n''}\tilde{R}_{n'}^{il}\tilde{R}_{n''}^{lm}\tilde{R}_{n}^{mj} \cdot H\left(z_n^{mj}-z_{n''}^{lm}-\epsilon\right)H\left(z_{n'}^{il}-z_{n''}^{lm}-\epsilon\right)e^{i\omega\left(t_{n'}^{v}+t_{n}^{v}-t_{n''}^{v}\right)}. \tag{2.48}$$

where $k_h^{ij}=k_g^j+k_s^i=\sqrt{\left(\frac{\omega}{c_j}\right)^2-\theta_{1j}^2}+\sqrt{\left(\frac{\omega}{c_i}\right)^2-\theta_{1i}^2}$.

2.4 Numerical tests

In the previous section, I provide a theoretical analysis on both normal and non-normal incidence cases for a laterally invariant elastic medium that the 1D elastic IMA algorithm can accurately predict the arrival times of all the 1^{st} order internal multiples without depending on the accuracy of used reference velocities. This is a surprising but encouraging result since it solves a practical issue due to near surface complexity for land exploration. Meanwhile, note that the amplitude of the predicted multiples contains extra transmission coefficients of the two deeper primaries convolved in the algorithm, so the predicted amplitude is attenuated by such extra transmission effect, and hence an adaptive subtraction is needed to eliminate the 1^{st} internal multiples from whole data.

2.4.1 Tests on acoustic over elastic media

Hsu and Weglein (2008) analytically demonstrated that the 1D acoustic IMA developed by ISS, equation (2.10), is insensitive to reference velocity in the prediction

of all 1^{st} order internal multiples, so a reasonable and interesting question will be whether we can implement the acoustic IMA into acoustic over elastic media, or in another words, whether the acoustic IMA accurately predicts converted internal multiples with both p-legs and s-legs. The answer to this question is important since the result of acoustic IMA can be a supplimental tool in land seismic data processing in which internal multiples are very hard to identify and near-surface property is complicated. In this part, I test the 1D acoustic IMA in acoustic over isotropic and anisotropic elastic media, to provide further confidence of implementation of both 1D acoustic and elastic IMA into land seismic exploration.

To get a sense of the accuracy of 1D acoustic IMA prediction, I first test it on a 5-layer acoustic medium with p-wave velocity, density, and Q variation. The predicted internal multiples and a comparison with the original input shot gather are shown in figure 2.3. The acoustic IMA algorithm precisely predicts all arrival times of the 1^{st} order internal multiples with only p-legs since this is an acoustic medium. All the primaries are not predicted and not touched. Even the primary very close to one of the predicted internal multiples is not predicted in the result, as highlighted by the yellow parabolic dashed line in the picture. This result examines and confirms the validity and effectiveness of the acoustic IMA algorithm.

A closer zoom-in comparison (see figure 2.4) between the predicted internal multiples and the input shot gather shows that both the amplitude and wavelet of the prediction are different from the input data. This is because the combination of using sub-events ("lower-higher-lower" constitution of three primary events) leads to an extra transmission effect (two more transmission coefficients of the two deeper

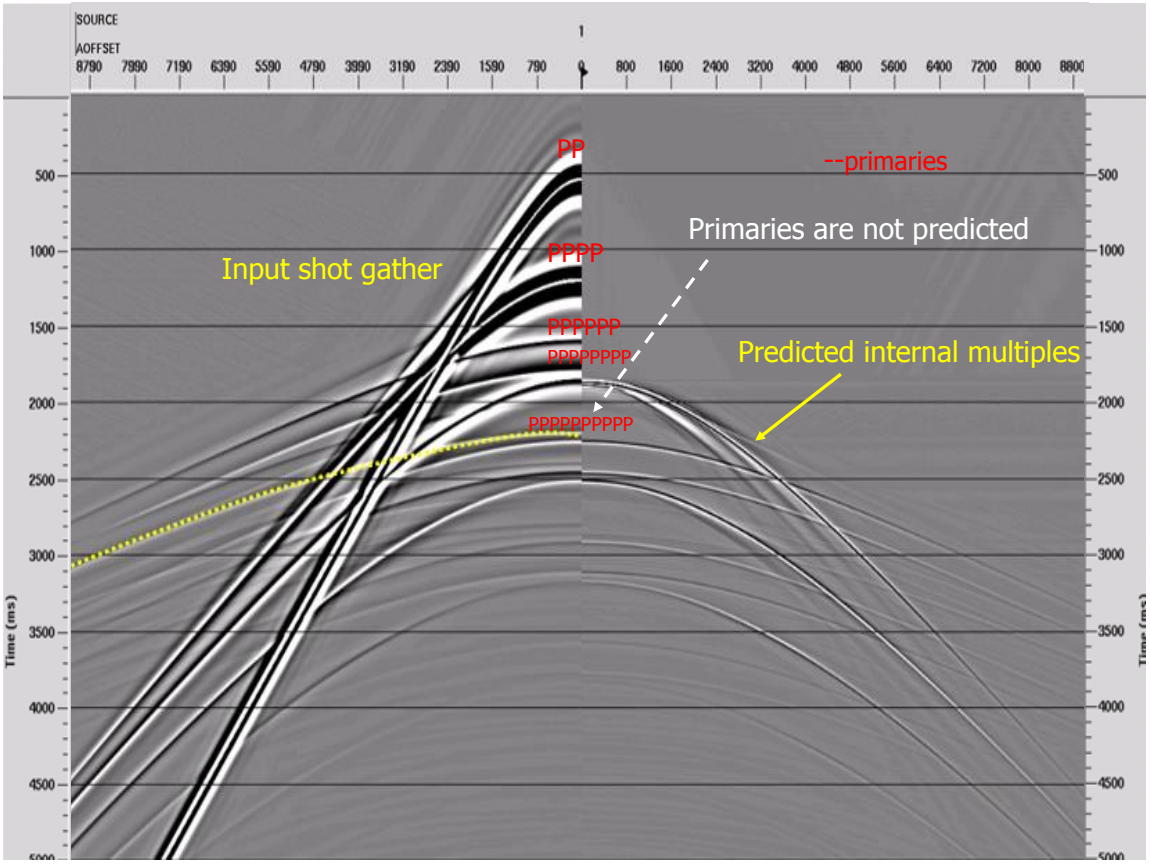

Figure 2.3: *Predicted* 1^{st} *order internal multiples on a 5-layer acoustic medium: left-hand side is the input shot gather where all* 5 *p-leg primaries are denoted by red letters, and the right-hand side is the prediction of the* 1^{st} *order internal multiples.*

primaries are multiplied in the final amplitude, and hence lead to an attenuated prediction of the internal multiple's amplitude), and result in the wavelet convolution of three sub-events (A convolution of three events are definitely different from the original one if the wavelet is not 1.). Thus an adaptive subtraction is needed for a further operation after the prediction so as to eliminate the coherent noise.

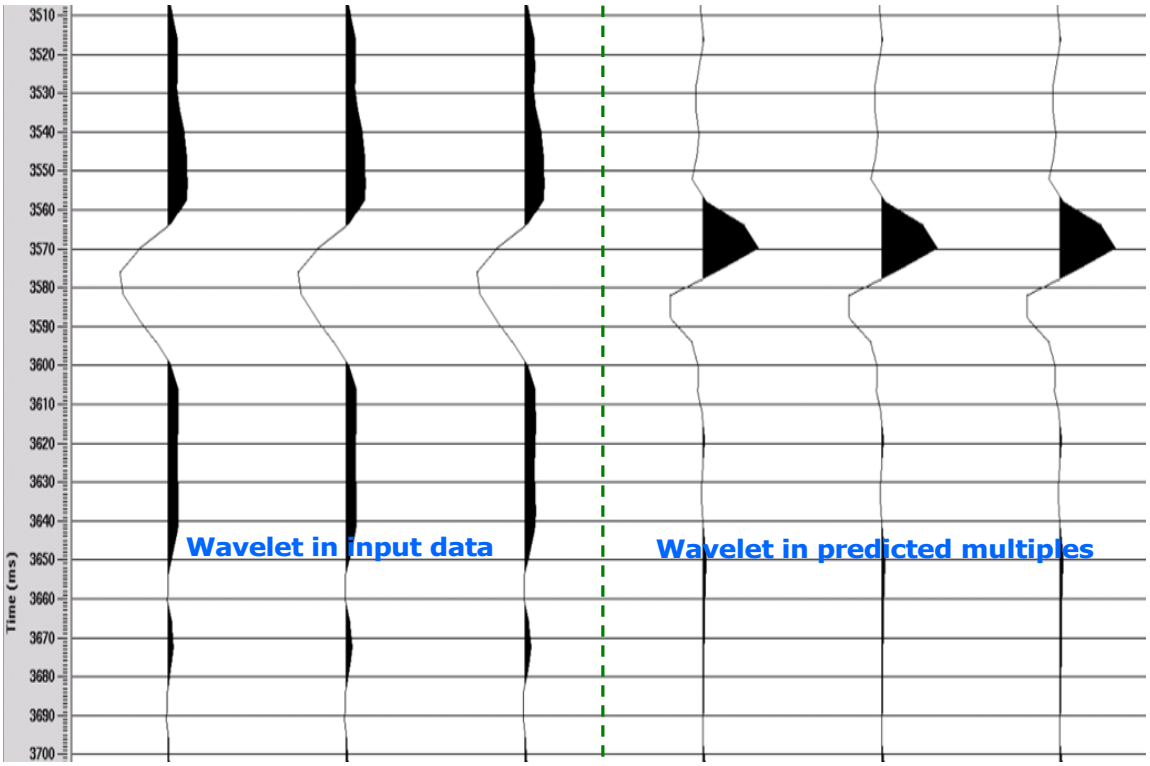

Figure 2.4: *A zoom-in comparison of amplitude prediction and wavelet difference between predicted* 1^{st} *order internal multiples and input shot gather.*

After the examination of the acoustic IMA, I use it to test acoustic over elastic media to check the extent of its validity and gain confidence before it is implemented into multi-component land data. Figure 2.5 shows the prediction and comparison

with input shot gather for a 3-layer acoustic over isotropic elastic medium with variation of p-wave velocity, s-wave velocity, density, and Q compensation. The prediction result is encouraging: all 1^{st} order internal multiples (denoted by yellow letters in the picture) including the converted s-leg internal multiples are accurately predicted. This test result demonstrates that the 1D acoustic ISS IMA can be effectively used for a medium with both acoustic and elastic properties. This is in accordance with the theory behind IMA since IMA uses three sub-events to reconstruct internal multiples, no matter whether the three sub-events are compressional waves or converted waves. However, there is still the problem of predicted amplitude and wavelet which can be addressed by a further adaptive subtraction skill or by using the elimination algorithm developed by M-OSRP.

Where anisotropic medium can be present as a real situation, I also implement the 1D acoustic IMA to an acoustic over elastic anisotropic VTI medium. The result is displayed in figure 2.6. I use the same 5-layer acoustic over elastic model but add an anisotropic velocity variation (VTI) instead of the original isotropic velocity. The VTI effect can be clearly observed in the far offset ends where vertical velocity is apparently slower than the previous isotropic case for the same primary events. Again, the arrival times of all 1^{st} order (and 2^{nd} order due to using the code which includes the prediction of it) internal multiples are correctly predicted, including the all p-leg and the converted internal multiples. The weakened amplitude and wavelet correction still requires further attention before applying subtraction to the original input data. Figure 2.7 displays the prediction after NMO[3] operation, so

[3]NMO stands for normal moveout. NMO is the procedure in seismic processing that compensates for the effects of the separation between seismic sources and receivers in the case of a horizontal

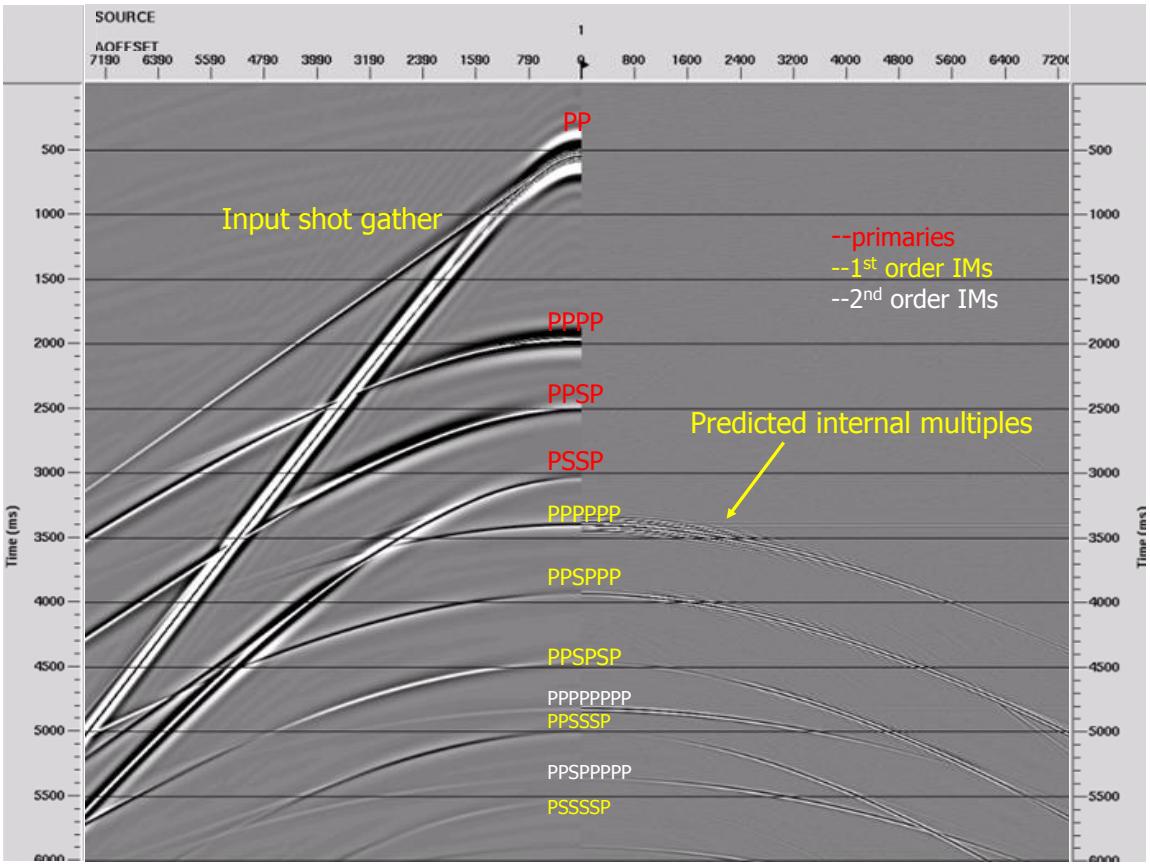

Figure 2.5: *A comparison between the input shot gather and the predicted internal multiples for an acoustic over isotropic elastic medium: for a clearer further comparison, the* 2^{nd} *order internal multiples denoted by white letters are also predicted by using the 1D acoustic IMA code which has included the prediction.*

the characteristic "*hockey-stick effect*"[4] (see figure 2.7 for an example) for the VTI medium is present. But the time prediction is also correct at far offsets for the VTI medium.

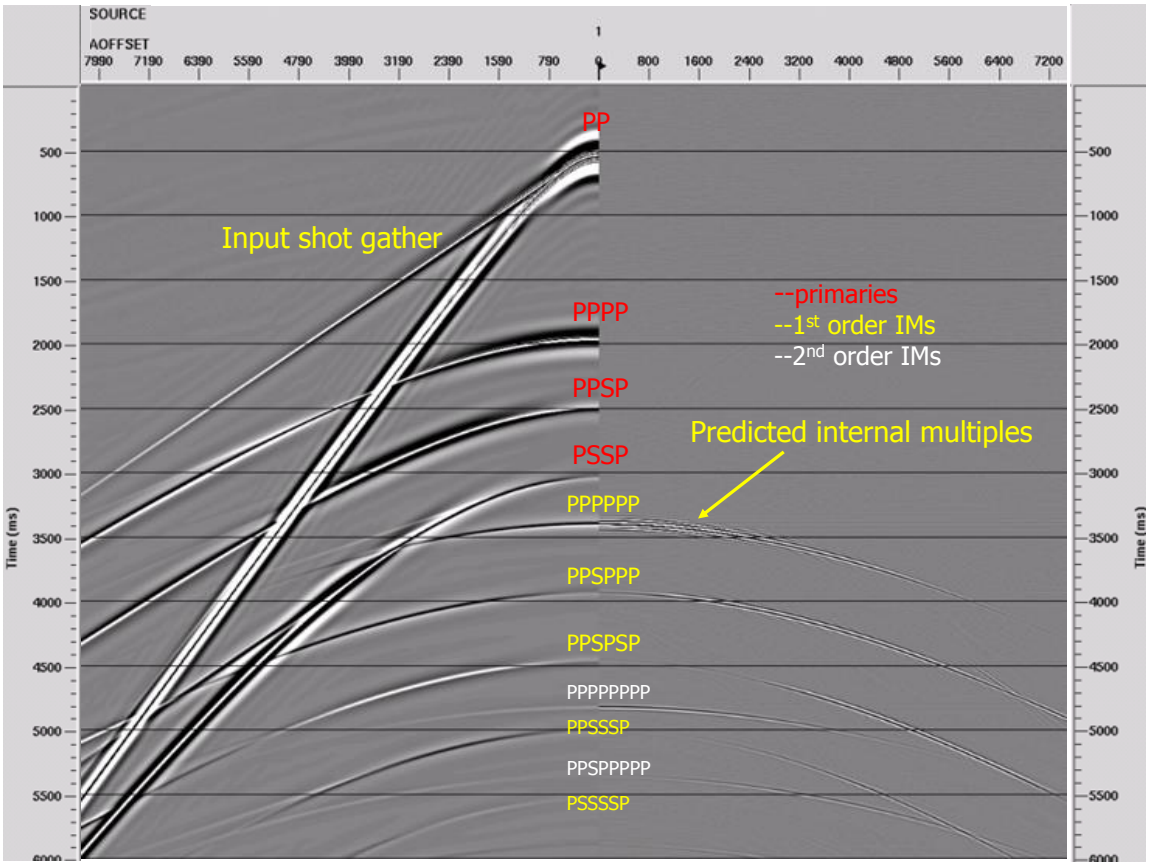

Figure 2.6: *The IMA prediction for an acoustic over anisotropic elastic VTI medium*

reflector. -From Schlumberger Oilfield Glossary: http://www.glossary.oilfield.slb.com

[4]VTI anisotropy caused by horizontal layering in the geology results in seismic velocities that vary with source-receiver offset or angle and produces the well known hockey stick effect on the far offsets.

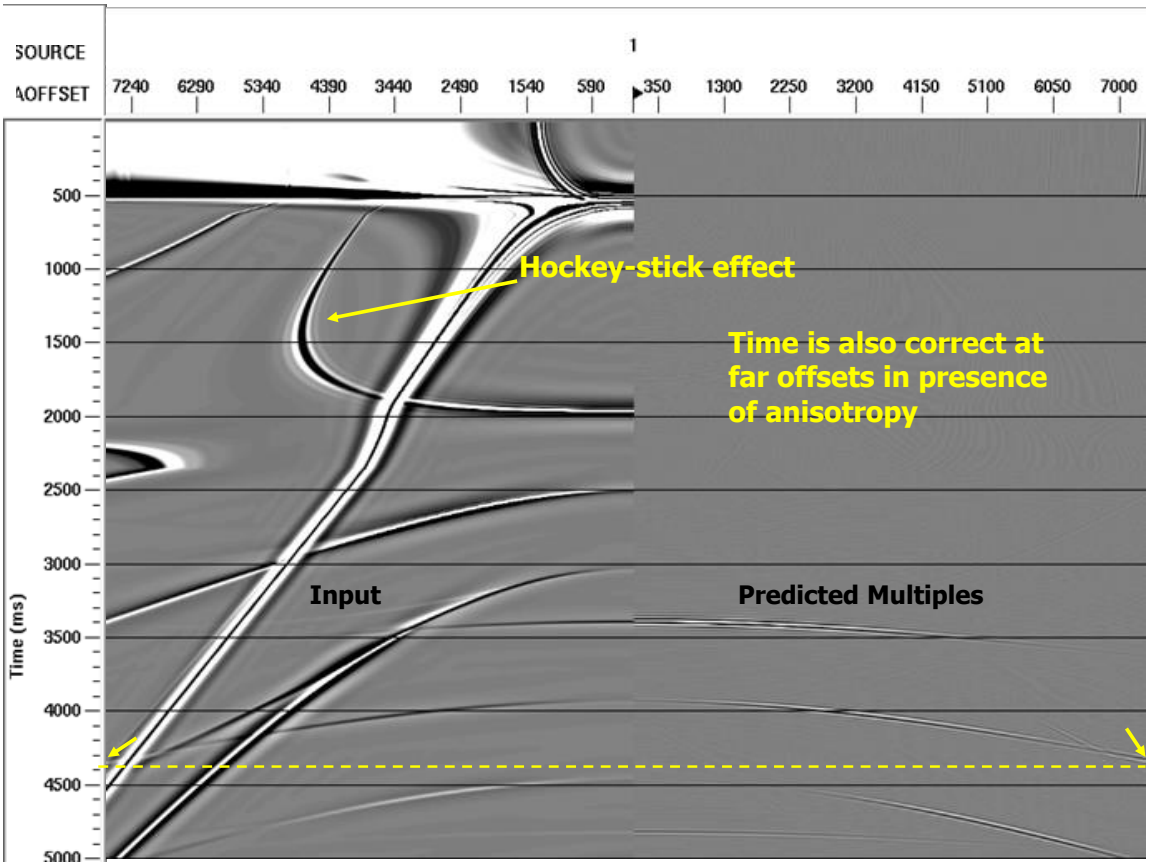

Figure 2.7: *The same prediction result of previous VTI medium with NMO: the arrival time prediction at far offsets is also accurate, as denoted by the yellow dashed horizontal line.*

2.4.2 Tests on elastic multi-component geophone data

In this section, I will numerically show the prediction results by diliberately using two different sets of reference velocity: one test is to use a correct P-wave velocity in the model's first layer as the reference velocity, while the other is to use a wrong reference as a comparison. The tested model below, shown in figure 2.8, is the one designed by Matson in his PhD thesis (Matson, 1997) where he used correct p-wave velocity and shear velocity as reference velocities for predicting elastic internal multiples including converted waves.

The multi-component seismic data are collected by (X, Y, Z) three directions, termed as inline, crossline and vertical orientation. I show here the predicted internal multiples of the data in XX and YY directions, respectively, for the above 3-layer elastic model. As a comparison, I tested the algorithm by using two reference velocities ($c_0 = 1500m/s$ and $c_0 = 1000m/s$). The results are shown in the following figures (2.9, 2.10, 2.11, and 2.12). Through the comparison among those predictions, we can determine the arrival times of the 1^{st} order internal multiples are accurately predicted, regardless of the reference velocities used in the algorithm. Since the algorithm is an attenuator, higher than the 1^{st} order internal multiples are not predicted. But amplitude of them are altered, and the amplitude of the 1^{st} order internal multiples is also weaker than the actual one, due to extra transmission coefficients of deeper subevents used to construct internal multiples in the algorithm.

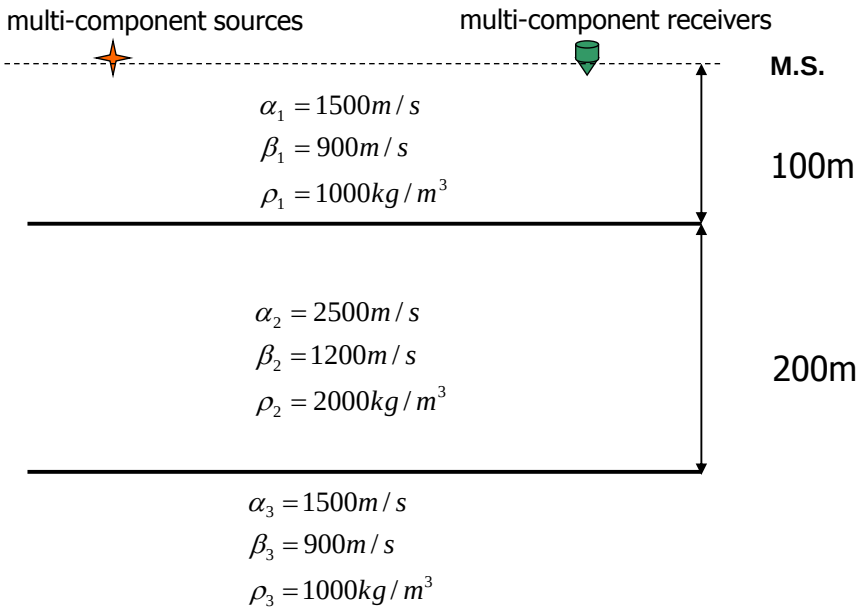

Figure 2.8: *A 3-layer elastic model to test reference velocity insensitivity: in the model, p-wave velocity, s-wave velocity and density are all varied to simulate an approximated earth structure for multi-component data.*

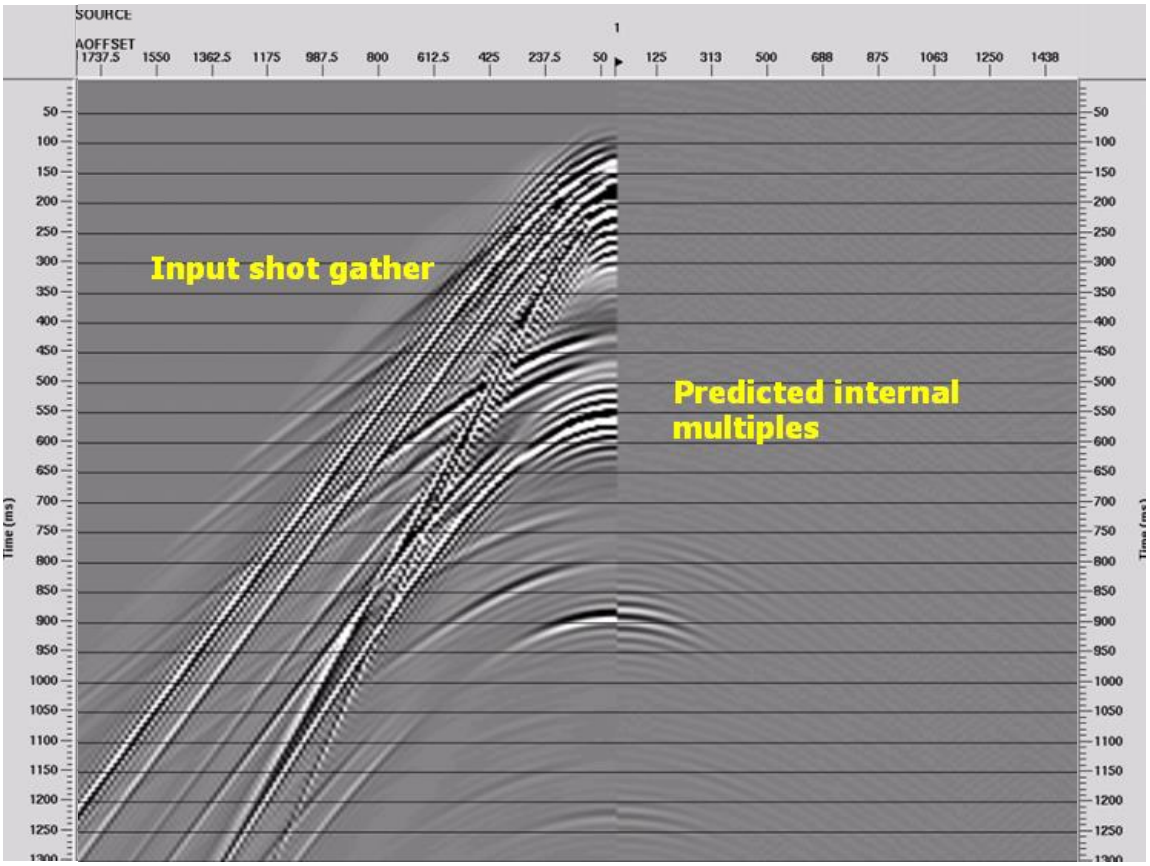

Figure 2.9: *Predicted* 1^{st} *order internal multiples in XX direction using* $c_0 = 1500m/s$*: left-hand side is the XX direction input shot gather, and the right-hand side is the prediction.*

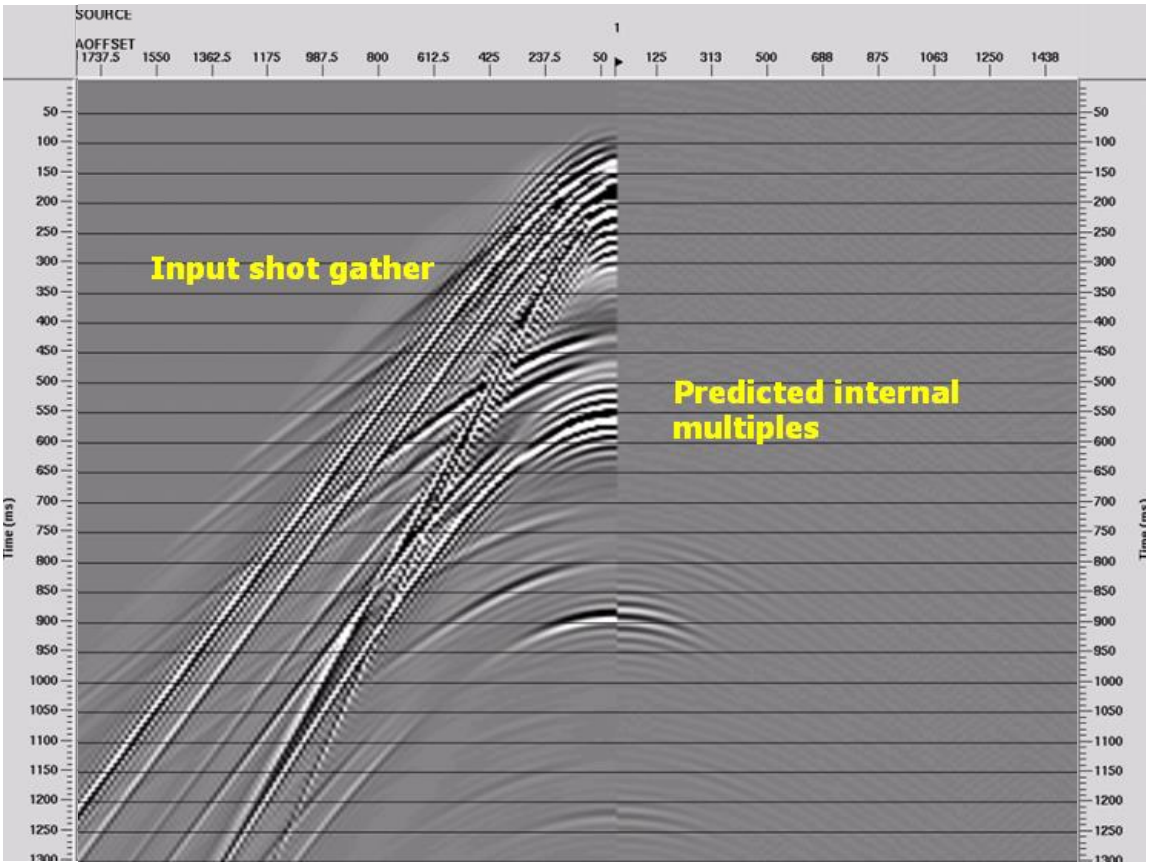

Figure 2.10: *Predicted* 1^{st} *order internal multiples in XX direction using* $c_0 = 1000m/s$*: left-hand side is the XX direction input shot gather, and the right-hand side is the prediction.*

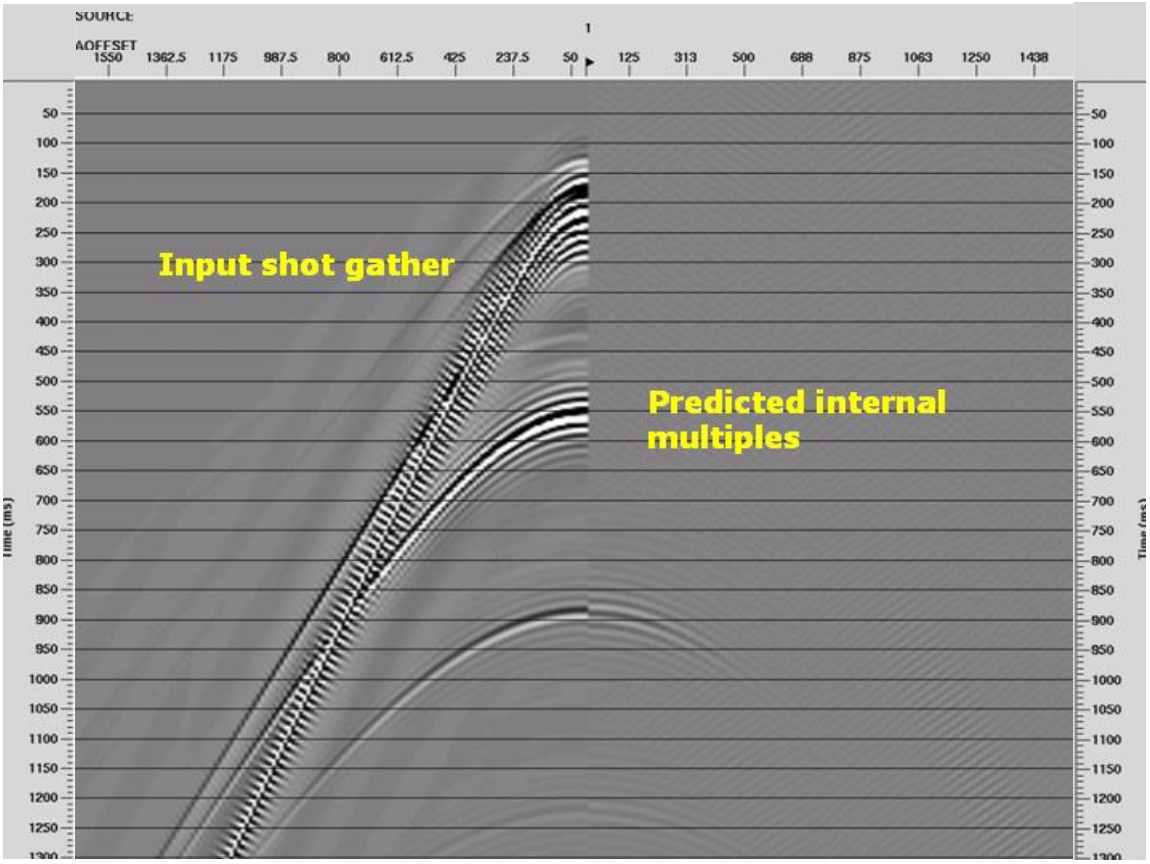

Figure 2.11: *Predicted* 1^{st} *order internal multiples in YY direction using* $c_0 = 1500m/s$*: left-hand side is the YY direction input shot gather, and the right-hand side is the prediction.*

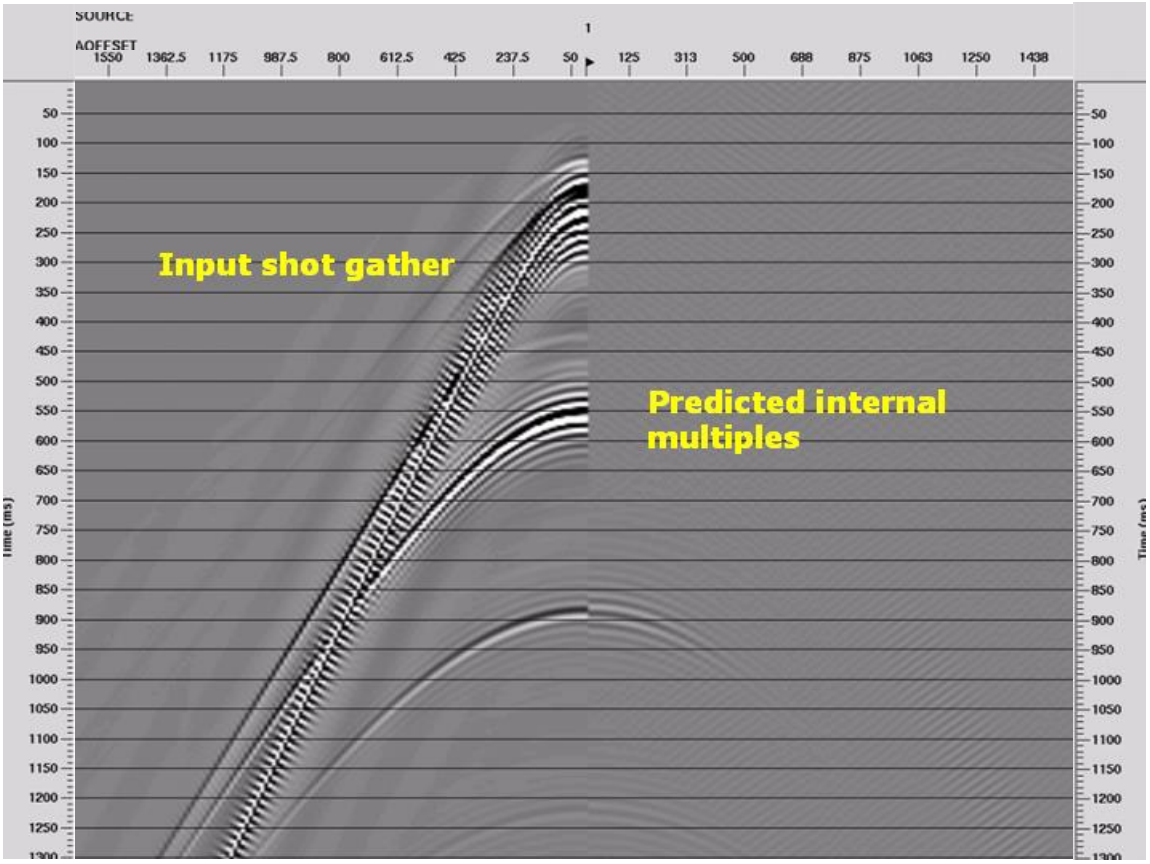

Figure 2.12: *Predicted* 1^{st} *order internal multiples in YY direction using* $c_0 = 1000m/s$*: left-hand side is the YY direction input shot gather, and the right-hand side is the prediction.*

2.5 Conclusion

In this chapter, I prove that 1D elastic inverse scattering series (*ISS*) internal multiple attenuator (*IMA*), equation (2.9) in Matson (1997) is insensitive to reference velocity by providing step-by-step analytic calculation for a laterally invariant elastic medium at normal and non-normal incidence cases. In land seismic exploration, the near-surface property can be heterogeneous and complicated to approximate, which in turn introduces complexity to suggest a proper reference background medium representing the near-surface overall property. The insensitivity to reference velocity for the ISS IMA excludes the above concern and provides validity when implementing the elastic IMA algorithm into land data processing. It also keeps the advantage and demultiple capability of ISS IMA without knowing any subsurface information.

The insensitivity property of the 1D elastic IMA also indicates that 1D acoustic IMA can be implemented for the elastic case, or acoustic over complicated elastic media (isotropic and anisotropic VTI), and still offers value for predicting internal multiples arrival times accurately. The successful numerical tests, displayed in the later part of this chapter, convince us of the added value of 1D acoustic IMA. A multi-component geophone dataset is also tested successfully in the last part, which directly demonstrates the confidence to implement the ISS IMA to the land case, and eventually to field datasets.

Chapter 3

Multi-parameter imaging algorithms using inverse scattering series

3.1 Chapter overview

Imaging challenges in a complex earth can be a significant obstacle to seismic effectiveness. The purpose of the research presented here is to extend the velocity only varying acoustic leading- and higher-order imaging methods of F. Liu (Shaw et al., 2002; Shaw and Weglein, 2003; Shaw, 2005; Liu et al., 2004, 2005; Liu, 2006) to a multi-parameter earth. In this chapter, I will first give a brief *background introduction* to the imaging research project delivered by the pioneers in the M-OSRP, and describe the roles and connection of the multi-parameter imaging research

in the whole imaging project. In the following section *algorithm development*, a clear analytic derivation of a two-parameter imaging algorithm is shown for a 1D acoustic medium with both velocity and density variations. The analytic calculation of the 3^{rd} ISS term leads to a closed form of the leading order multi-parameter imaging which justifies the imaging conjectures by Weglein (Jiang and Weglein, 2008). To further gain full confidence of the effectiveness and efficiency of the implementation of the conjectured multi-parameter imaging algorithms, a series of numerical tests using both analytic data (Jiang et al., 2009) and synthetic data are conducted, examined, compared, and discussed in the section of *algorithm tests*. A short *discussion and conclusion* will then be presented in the last section of this chapter.

3.2 Background introduction

Many pressing challenges in current seismic exploration can be addressed by using the inverse scattering series (*ISS*) (Weglein, 1985; Weglein et al., 1997, 2003). For instance, depth imaging using *ISS* proceeds without knowing any subsurface information (subsurface velocity fields, for example). The development of depth imaging algorithm at M-OSRP proceeds in stages:

Stage (1) - for a 1D one parameter (velocity variation only) acoustic medium, a leading order imaging sub-series ($LOIS$) is identified and tested in Weglein et al. (2000), Shaw et al. (2002),Shaw and Weglein (2003), and Shaw (2005). It works for a layered medium with small velocity contrasts, because this imaging series is a partial capture of the whole imaging series. The $LOIS$ can be written as a closed form.

Stage (2) - for a multi-D one parameter (velocity variation only) acoustic medium, a laterally-variant acoustic medium with large velocity contrasts is considered. The calculation of the *ISS* terms in the multi-D medium leads to more imaging terms including new imaging terms that can not be identified in the 1D medium. These terms deal with the lateral variations of the medium. By capturing more imaging terms than the *LOIS* in the 1D acoustic case, a higher order imaging sub-series (*HOIS*) and corresponding closed form are identified and numerically tested on a salt model with lateral variation and large velocity contrasts (Liu et al., 2004, 2005; Liu, 2006). The numerical test result indicates the *HOIS* imaging algorithm works very well for a multi-dimensional acoustic medium with velocity variation only. The logic connection and understanding between the *LOIS* and *HOIS* closed forms for depth-imaging have been analyzed in Zhang et al. (2007).

Stage (3) - To advance the *ISS* imaging algorithm application to the real earth which is a multi-parameter medium, it is necessary to derive a multi-parameter (velocity, density variation etc.) *ISS* imaging algorithm. In this stage, starting with the simplest model, a multi-parameter 1D acoustic medium is studied. An imaging-only term is identified in Zhang and Weglein (2005) for a layered acoustic medium with both velocity and density variations. Following the philosophy of identifying the *LOIS* and *HOIS* algorithm, a conjectured imaging algorithm for the 1D two-parameter acoustic medium was proposed by Weglein in 2007. This was further extended to multi-D multi-parameter acoustic and elastic cases. The extension is done by substituting the integral in the imaging-only term of the one-parameter case with the integral of the imaging-only term under the multi-parameter case. The

final expression of the imaging formula for a multi-parameter medium (either acoustic or elastic) is expressed as a shifted data-set scaled by a constant subjected to the imaged seismic model. For example, for the 1D two-parameter acoustic medium, the conjectured imaging algorithm indicates that the two parameters will be imaged together as a composite. In other words, the imaging task does not distinguish which parameter, either velocity or density, should be recognized to image, but recognizes them as a combined form linear to the measured data set - a "composite". If there is no variation in the velocity parameter of the medium, then the imaging algorithm will shut down automatically. To justify the conjectured imaging algorithm, higher *ISS* terms need to be calculated so that higher order imaging-only terms can be identified and collected to develop an imaging algorithm in the multi-parameter case.

Stage (4), stage (5) and stage (6) respectively, are for a multi-D multi-parameter acoustic medium, for a 1D/multi-D multi-parameter elastic medium, and for a model type independent depth imaging algorithm. The imaging algorithm development for the former two stages will be continued following stage (3) in the way to justify Weglein's imaging conjectures. The last stage is the ultimate objective to develop the *ISS* imaging algorithm - the model type independent *ISS* imaging algorithm which means to image the medium by using the same algorithm without interference from the underlying imaged medium whether it is acoustic, elastic, or inelastic.

It is important to mention that all of the imaging algorithms have been developed or will be developed without knowledge of any priori information of the subsurface – to image directly the subsurface medium using only the data set collected on the measurement surface and the chosen reference wavefield (Weglein et al., 2003).

The research in this chapter presents an effort to advance research within stage (3). As a starting point, a laterally-invariant acoustic medium with both velocity and density variation (two parameters) will be considered and studied here.

3.2.1 1D two-parameter acoustic medium

To study a 1D two-parameter acoustic medium, let us first consider the 3D acoustic wave equations in the actual and reference medium (Zhang and Weglein, 2005),

$$\begin{aligned}\left[\frac{\omega^2}{K(\mathbf{r})}+\nabla\cdot\frac{1}{\rho(\mathbf{r})}\nabla\right]G(\mathbf{r},\mathbf{r_s};\omega)&=\delta(\mathbf{r}-\mathbf{r_s}),\\ \left[\frac{\omega^2}{K_0(\mathbf{r})}+\nabla\cdot\frac{1}{\rho_0(\mathbf{r})}\nabla\right]G_0(\mathbf{r},\mathbf{r_s};\omega)&=\delta(\mathbf{r}-\mathbf{r_s}).\end{aligned} \tag{3.1}$$

where G and G_0 are the actual and reference Green's functions, or wavefields, respectively, for a single temporal frequency, ω. $K=c^2\rho$, is P-bulk modulus, c is P-wave velocity and ρ is the density. The quantities with subscript "0" are in the reference medium, otherwise, they are in the actual medium.

The perturbation operator is therefore defined as,

$$V=L_0-L=\frac{\omega^2\alpha}{K_0(\mathbf{r})}+\nabla\cdot\frac{\beta}{\rho_0(\mathbf{r})}\nabla, \tag{3.2}$$

where $\alpha=1-\frac{K_0}{K}$, $\beta=1-\frac{\rho_0}{\rho}$.

Similar to operator V, we also expand α and β in orders of the data, considering a 1D acoustic medium,

$$\begin{aligned}\alpha(z)&=\alpha_1(z)+\alpha_2(z)+...\\ \beta(z)&=\beta_1(z)+\beta_2(z)+...\end{aligned} \tag{3.3}$$

3.2.2 Results of the first two ISS terms

Using the expansions of α and β, and inserting equation (3.2) into the *ISS*, equation (1.7) and equation (1.8), yields the 1^{st} order and 2^{nd} order approximations to the two parameters (Zhang and Weglein, 2005):

$$D(z,\theta) = -\frac{\rho_0}{4}\left[\frac{1}{\cos^2\theta}\alpha_1(z) + \left(1-\tan^2\theta\right)\beta_1(z)\right], \tag{3.4}$$

and,

$$\begin{aligned}
&\frac{1}{\cos^2\theta}\alpha_2(z) + \left(1-\tan^2\theta\right)\beta_2(z) \\
&= -\frac{1}{2}\frac{1}{\cos^4\theta}\alpha_1^2(z) - \frac{1}{2}\left(\tan^4\theta+1\right)\beta_1^2(z) + \frac{\tan^2\theta}{\cos^2\theta}\alpha_1(z)\beta_1(z) \\
&- \frac{1}{2}\frac{1}{\cos^4\theta}\alpha_1{}'(z)\int_{-\infty}^{z}\left[\alpha_1(z')-\beta_1(z')\right]dz' + \frac{1}{2}\left(\tan^4\theta-1\right)\beta_1{}'(z)\int_{-\infty}^{z}\left[\alpha_1(z')-\beta_1(z')\right]dz'.
\end{aligned} \tag{3.5}$$

Here we have already made an inverse Fourier transform with respect to $-2q_g$ from the original equation, and set $z_g = z_s = 0$ for simplicity. For the two parameters case, the imaging-only terms were identified in equation (3.5) as the integral terms in Zhang and Weglein (2005).

3.2.3 Conjectured multi-parameter imaging algorithms

In this section, a series of conjectured imaging algorithms, first proposed by Weglein, for both acoustic and elastic multi-parameter media are introduced, and the logic behind the development of those algorithms is described.

Let us take a retrospect on the *LOIS* imaging algorithm development of the 1D velocity-only acoustic medium at normal incidence (Weglein et al., 2000; Shaw et al.,

2002; Shaw and Weglein, 2003; Shaw, 2005). The first three orders imaging-only terms captured in the *LOIS* imaging algorithm are respectively,

$$\alpha_1(z), \quad -\frac{1}{2}\frac{d\alpha_1(z)}{dz}\int_{-\infty}^{z}\alpha_1(z')dz', \quad \frac{1}{8}\frac{d^2\alpha_1(z)}{dz^2}\left[\int_{-\infty}^{z}\alpha_1(z')dz'\right]^2.$$

In the above three terms, the z is a pseudo-depth obtained by re-scaling time with a reference velocity (for example water speed). The derivatives outside the integrals are analyzed as "*attention-needed terms*", and the integrals are "*attention-provided terms*"(proposed and discussed by Weglein in 2005/2006 M-OSRP annual reports). The attention-needed term indicates the local amplitude variation of the imaged parameter with respect to depth z. (The parameter is the velocity for the 1D acoustic medium considered above, for instance.) This local amplitude variation examination will show the local medium property variations (including real velocity change) of the seismic model. If the local properties changed, this term puts the attention light on. If and only if the reference velocity used to locate the parameter to the pseudo-depth z is different from the real velocity in the seismic model, then the "attention-provided term" will be turned on to correct the migration effect by using the wrong reference velocity. The correction will be accumulated from the above medium down to the current pseudo-depth z by doing the integral of the velocity difference in the 1^{st} order. For example, in the above three terms, $\alpha_1(z)$ is the 1^{st} order of the velocity parameter. The derivative of $\alpha_1(z)$ indicates at pseudo-depth z the velocity parameter needs "attention" by comparing the local velocity with the reference velocity. If the local velocity is different from the reference velocity used in the inverse scattering series, then, the integral term will provide "attention" by summing together the velocity difference down to the current pseudo-depth z. In

another words, if the used reference velocity is exactly the velocity of the underlying imaged medium, the integral term shuts down, therefore no imaging task is needed: the imaging result is correct by using reference velocity.

By adding together all of the leading order imaging-only terms like the above three terms in the higher order *ISS* terms, the leading order imaging sub-series closed form was obtained,

$$\alpha^{LOIS}(z) = \alpha_1 \left(z - \frac{1}{2} \int_{-\infty}^{z} \alpha_1(z')dz' \right). \tag{3.6}$$

The closed form above is a shifted "attention-needed term" by a quantity of the "attention-provided term".

Now let us take a look at the imaging-only term for the multi-parameter acoustic medium in equation (3.5). Rewritten in the following form:

$$-\frac{1}{2}\frac{1}{\cos^2\theta}\left[\frac{1}{\cos^2\theta}\alpha_1(z) + \left(1-\tan^2\theta\right)\beta_1(z)\right]\int_{-\infty}^{z}\left[\alpha_1(z') - \beta_1(z')\right]dz'$$

The "*attention-needed terms*" turn out to be the combination term of the two parameters $\alpha_1(z)$ and $\beta_1(z)$ in the bracket, and the corresponding "*attention-provided term*" is the integral of $\alpha_1(z) - \beta_1(z)$ which only takes care of the velocity change (Zhang and Weglein, 2005). If there is no velocity change in the medium, the integral shuts down and the imaging task is not needed. The logic here is following the same logic as we stated above for the 1D one-parameter acoustic medium case. So, based

on this logic comparison, Weglein's imaging conjecture is proposed for the 1D two-parameter acoustic medium:

$$\begin{aligned}\mathscr{D}^{LOIS}(z,\theta) &= \frac{1}{\cos^2\theta}\alpha_1\left(z-\frac{1}{2}\frac{1}{\cos^2\theta}\int_{-\infty}^{z}\left(\alpha_1(z')-\beta_1(z')\right)dz'\right)\\ &\quad+\left(1-\tan^2\theta\right)\beta_1\left(z-\frac{1}{2}\frac{1}{\cos^2\theta}\int_{-\infty}^{z}\left(\alpha_1(z')-\beta_1(z')\right)dz'\right)\\ &= -\frac{4}{\rho_0}D^{PP}\left(z-\frac{1}{2}\frac{1}{\cos^2\theta}\int_{-\infty}^{z}\left(\alpha_1(z')-\beta_1(z')\right)dz',\theta\right)\end{aligned} \tag{3.7}$$

where $D^{PP}(z,\theta)$ is PP-only data (compressional wave only) for an acoustic medium, and expressed in equation (3.4).

Following the same philosophy and logic of the "*attention-needed term*" and the "*attention-provided term*", the above conjecture was extended to a multi-D multi-parameter acoustic and elastic media, by directly substituting the original one-parameter "*attention-provided term*" with the multi-parameter "*attention-provided term*" expressed in the multi-parameter shifted "*attention-needed term*".

The following formula are conjectured *LOIS* imaging closed forms and their extended *HOIS* imaging algorithms for both acoustic and elastic cases.

1. Extended 1D three-parameter elastic PP data only *LOIS* algorithm:

$$\mathscr{D}^{LOIS}(z,\theta) = -4D^{PP}\left(z-\frac{1}{2}\frac{1}{\cos^2\theta}\int_{-\infty}^{z}\left(a^1_\gamma(z')-a^1_\rho(z')\right)dz'\right) \tag{3.8}$$

where $D^{PP}(z,\theta)$ is the PP component data in this elastic case, and is expressed as,

$$D^{PP}(z,\theta) = -\frac{1}{4}\left(1+\tan^2\theta\right)a^1_\gamma(z)-\frac{1}{4}\left(1-\tan^2\theta\right)a^1_\rho(z)+2\frac{\beta_0^2\sin^2\theta}{\alpha_0^2}a^1_\mu(z). \tag{3.9}$$

where $a^1_\rho(z), a^1_\gamma(z), a^1_\mu(z)$ are the 1^{st} order approximations of density, bulk modulus and shear modulus variations, respectively. More details regarding the definitions of these parameters can be found in Zhang and Weglein (2006).

2. Extended 1D multi-parameter *HOIS* algorithms:

   (i). for a 1D two-parameter acoustic medium,

$$\mathscr{D}^{HOIS}\left(z+\frac{1}{2}\int_{-\infty}^{z}\frac{\alpha_1(z')-\beta_1(z')}{\cos^2\theta-0.25\left(\alpha_1(z')-\beta_1(z')\right)}dz'\right)=D^{PP}(z,\theta) \tag{3.10}$$

   where $D^{PP}(z,\theta)$ is expressed as,

$$D^{PP}(z,\theta)=-\frac{\rho_0}{4}\left(\frac{1}{\cos^2\theta}\alpha_1(z)+\left(1-\tan^2\theta\right)\beta_1(z)\right). \tag{3.11}$$

   (ii). for a 1D three-parameter elastic PP data only case,

$$\mathscr{D}^{HOIS}\left(z+\frac{1}{2}\int_{-\infty}^{z}\frac{a^1_\gamma(z')-a^1_\rho(z')}{\cos^2\theta-0.25\left(a^1_\gamma(z')-a^1_\rho(z')\right)}dz'\right)=D^{PP}(z,\theta) \tag{3.12}$$

   where the PP data is defined in equation (3.9).

   It is quite straightforward to extend the above 1D acoustic and elastic *HOIS* closed forms to a multi-D multi-parameter acoustic and elastic imaging closed forms.

3. For an acoustic medium,

$$\mathscr{D}^{HOIS}\left(x,y,z+\frac{1}{2}\int_{-\infty}^{z}\frac{\alpha_1(x,y,z')-\beta_1(x,y,z')}{\cos^2\theta-0.25\left(\alpha_1(x,y,z')-\beta_1(x,y,z')\right)}dz'\right)=D^{PP}(x,y,z,\theta) \tag{3.13}$$

4. For PP data in an elastic medium,

$$\mathscr{D}^{HOIS}\left(x,y,z+\frac{1}{2}\int_{-\infty}^{z}\frac{a_{\gamma}^{1}(x,y,z')-a_{\rho}^{1}(x,y,z')}{\cos^{2}\theta-0.25\left(a_{\gamma}^{1}(x,y,z')-a_{\rho}^{1}(x,y,z')\right)}dz'\right)=D^{PP}(x,y,z,\theta) \tag{3.14}$$

The multi-D dataset $D(x,y,z,\theta)$, for the acoustic case, is PP only data; for ocean bottom measurements and an elastic medium, it can be a multi-component PP, PS, SP, or SS dataset.

To justify Weglein's imaging conjecture, I will examine it on the 1D two-parameter acoustic medium by calculating and capturing higher imaging-only *ISS* terms in the following section. Due to an exponential increase in the complexity of the calculation for higher and higher *ISS* terms, a good method is to calculate as few *ISS* terms as possible, identify a similar mathematical pattern in higher order terms, and then conclude an imaging sub-series and closed form from those similar terms. The following sections are based on this idea and examine the conjectured imaging algorithm for the two-parameter acoustic medium.

3.3 Derivation of two-parameter acoustic imaging algorithms

This section aims to identify a multi-parameter imaging algorithm by analytically calculating and capturing some imaging-only terms hidden in the higher order *ISS* terms for a laterally-invariant two-parameter acoustic medium, so as to justify the conjecture philosophy and the corresponding conjectured imaging form of

equation (3.7).

3.3.1 Analytic derivation of the 3^{rd} order *ISS* term

Let me start with the calculation of the *ISS* third term,

$$-G_0V_3G_0 = G_0V_2G_0V_1G_0 + G_0V_1G_0V_2G_0 + G_0V_1G_0V_1G_0V_1G_0. \tag{3.15}$$

where,

$$G_0V_3G_0 = \iint_{-\infty}^{\infty} dx'dz' G_0(x_g, z_g; x', z')\hat{V}_3(x', z')G_0(x', z'; x_s, z_s) \tag{3.16}$$

$$\begin{aligned} G_0V_2G_0V_1G_0 &= \iint_{-\infty}^{\infty} dx'dz' \iint_{-\infty}^{\infty} dx''dz'' G_0(x_g, z_g; x', z')\hat{V}_2(x', z')G_0(x', z'; x'', z'') \\ &\cdot\hat{V}_1(x'', z'')G_0(x'', z''; x_s, z_s) \end{aligned} \tag{3.17}$$

$$\begin{aligned} G_0V_1G_0V_2G_0 &= \iint_{-\infty}^{\infty} dx'dz' \iint_{-\infty}^{\infty} dx''dz'' G_0(x_g, z_g; x', z')\hat{V}_1(x', z')G_0(x', z'; x'', z'') \\ &\cdot\hat{V}_2(x'', z'')G_0(x'', z''; x_s, z_s) \end{aligned} \tag{3.18}$$

$$\begin{aligned} G_0V_1G_0V_1G_0V_1G_0 &= \iint_{-\infty}^{\infty} dx'dz' \iint_{-\infty}^{\infty} dx''dz'' \iint_{-\infty}^{\infty} dx'''dz''' \\ &G_0(x_g, z_g; x', z')\hat{V}_1(x', z')G_0(x', z'; x'', z'')\hat{V}_1(x'', z'') \\ &G_0(x'', z''; x''', z''')\hat{V}_1(x''', z''')G_0(x''', z'''; x_s, z_s). \end{aligned} \tag{3.19}$$

For the 1D two-parameter acoustic medium, the perturbation defined in equation (3.2) becomes,

$$\hat{V}_n(x', z') = \frac{\omega^2}{K_0}\alpha_n(z') + \frac{\beta_n(z')}{\rho_0}\frac{\partial^2}{\partial x'^2} + \frac{1}{\rho_0}\frac{\partial}{\partial z'}\beta_n(z')\frac{\partial}{\partial z'} \qquad n = 1, 2, 3... \tag{3.20}$$

and a 2D Green's function bilinear form is used in calculation, which is defined as,

$$G_0(x', z'; x'', z'') = \frac{\rho_0}{(2\pi)^2} \iint_{-\infty}^{\infty} dk_x{}' dk_z{}' \frac{e^{ik_x{}'(x'-x'')} e^{ik_z{}'(z'-z'')}}{k^2 - \left(k_x{}'^2 + k_z{}'^2\right)}. \tag{3.21}$$

After mathematical calculation[1], the third term turns out to be,

$$\begin{aligned}
&\frac{1}{\cos^2\theta}\alpha_3(z) + \left(1 - \tan^2\theta\right)\beta_3(z) \\
&= -\frac{1}{\cos^4\theta}\left[\alpha_1(z) - \beta_1(z)\right]\left[\alpha_2(z) - \beta_2(z)\right] + \frac{1}{4}\frac{1}{\cos^2\theta}\beta_1^2(z)\left[\alpha_1(z) - \beta_1(z)\right] \\
&+ \frac{1}{8}\frac{1}{\cos^4\theta}\beta_1(z)\left[\alpha_1(z) - \beta_1(z)\right]^2 - \frac{5}{16}\frac{1}{\cos^6\theta}\left[\alpha_1(z) - \beta_1(z)\right]^3 \\
&- \frac{1}{2}\frac{1}{\cos^4\theta}\alpha_1{}'(z)\int_{-\infty}^{z}\left[\alpha_2(z') - \beta_2(z')\right]dz' \\
&- \frac{1}{2}\frac{1}{\cos^4\theta}\alpha_2{}'(z)\int_{-\infty}^{z}\left[\alpha_1(z') - \beta_1(z')\right]dz' \\
&+ \frac{1}{2}\left(\tan^4\theta - 1\right)\beta_1{}'(z)\int_{-\infty}^{z}\left[\alpha_2(z') - \beta_2(z')\right]dz' \\
&+ \frac{1}{2}\left(\tan^4\theta - 1\right)\beta_2{}'(z)\int_{-\infty}^{z}\left[\alpha_1(z') - \beta_1(z')\right]dz' \\
&- \frac{1}{8}\frac{1}{\cos^6\theta}\alpha_1{}''(z)\left[\int_{-\infty}^{z}(\alpha_1(z') - \beta_1(z'))dz'\right]^2 \\
&- \frac{1}{8}\frac{1}{\cos^4\theta}\left(1 - \tan^2\theta\right)\beta_1{}''(z)\left[\int_{-\infty}^{z}(\alpha_1(z') - \beta_1(z'))dz'\right]^2 \\
&- \frac{1}{4}\frac{3}{\cos^6\theta}\alpha_1(z)\alpha_1{}'(z)\int_{-\infty}^{z}\left[\alpha_1(z') - \beta_1(z')\right]dz' \\
&+ \frac{1}{4}\frac{3}{\cos^6\theta}\beta_1(z)\alpha_1{}'(z)\int_{-\infty}^{z}\left[\alpha_1(z') - \beta_1(z')\right]dz' \\
&+ \frac{1}{4}\frac{1}{\cos^4\theta}\left(3\tan^2\theta + 1\right)\alpha_1(z)\beta_1{}'(z)\int_{-\infty}^{z}\left[\alpha_1(z') - \beta_1(z')\right]dz' \\
&+ \frac{1}{4}\frac{1}{\cos^4\theta}\left(3\tan^2\theta - 1\right)\beta_1(z)\beta_1{}'(z)\int_{-\infty}^{z}\left[\alpha_1(z') - \beta_1(z')\right]dz'
\end{aligned}$$

[1]Detailed mathematical derivation can be found in the Appendix part in this dissertation.

$$
\begin{aligned}
&- \frac{1}{4}\frac{1}{\cos^4\theta}\beta_1{}'(z)\int_{-\infty}^{z}\left[\alpha_1(z')-\beta_1(z')\right]^2 dz' \\
&- \frac{1}{8}\frac{1}{\cos^6\theta}\left[\alpha_1{}'(z)-\beta_1{}'(z)\right]\int_{-\infty}^{z}\left[\alpha_1(z')-\beta_1(z')\right]^2 dz' \\
&+ MUL. \qquad (3.22)
\end{aligned}
$$

where $MUL.$ term is the multiple-related term expressed as the following equation,

$$
\begin{aligned}
MUL. = &- \frac{1}{16}\frac{1}{\cos^6\theta}\int_{-\infty}^{z}\alpha_1{}'(z')\int_{-\infty}^{z}\alpha_1{}'(z'')\alpha_1(z'+z''-z)dz''dz' \\
&- \frac{1}{8}\left(\frac{1}{\cos^4\theta}-\frac{1}{2}\frac{1}{\cos^6\theta}\right)\int_{-\infty}^{z}\alpha_1{}'(z')\int_{-\infty}^{z}\alpha_1{}'(z'')\beta_1(z'+z''-z)dz''dz' \\
&- \frac{1}{4}\left(\frac{1}{\cos^4\theta}-\frac{1}{2}\frac{1}{\cos^6\theta}\right)\int_{-\infty}^{z}\alpha_1{}'(z')\int_{-\infty}^{z}\beta_1{}'(z'')\alpha_1(z'+z''-z)dz''dz' \\
&- \frac{1}{4}\left(\frac{2}{\cos^2\theta}-\frac{2}{\cos^4\theta}+\frac{1}{2}\frac{1}{\cos^6\theta}\right)\int_{-\infty}^{z}\alpha_1{}'(z')\int_{-\infty}^{z}\beta_1{}'(z'')\beta_1(z'+z''-z)dz''dz' \\
&- \frac{1}{4}\left(\frac{1}{\cos^2\theta}-\frac{1}{\cos^4\theta}+\frac{1}{4}\frac{1}{\cos^6\theta}\right)\int_{-\infty}^{z}\beta_1{}'(z')\int_{-\infty}^{z}\beta_1{}'(z'')\alpha_1(z'+z''-z)dz''dz' \\
&+ \frac{1}{4}\left(\frac{3}{\cos^2\theta}-\frac{3}{2}\frac{1}{\cos^4\theta}+\frac{1}{4}\frac{1}{\cos^6\theta}\right)\int_{-\infty}^{z}\beta_1{}'(z')\int_{-\infty}^{z}\beta_1{}'(z'')\beta_1(z'+z''-z)dz''dz'. \qquad (3.23)
\end{aligned}
$$

where the $'$ denotes a derivative of the argument in that function.

3.3.2 Examination on the one-parameter case

Now we have already obtained the complicated mathematical expression for the 3^{rd} *ISS* term. How good is the calculation? Let us check the 3^{rd} term result under a 1D acoustic medium with velocity variation only at normal incidence case.

Under the above assumptions,

$$\beta_1 = 0, \qquad \theta = 0 \ (then,\ \cos\theta = 1 \ and \ \tan\theta = 0).$$

By using the above two values, we can further simplify the 3^{rd} term,

$$L.H.S. = \alpha_3(z).$$

$$\begin{aligned} R.H.S. = & -\alpha_1(z)\alpha_2(z) - \frac{5}{16}{\alpha_1}^3(z) \\ & - \frac{1}{2}{\alpha_1}'(z)\int_{-\infty}^{z}\alpha_2(z')dz' - \frac{1}{2}{\alpha_2}'(z)\int_{-\infty}^{z}\alpha_1(z')dz' \\ & - \frac{1}{8}{\alpha_1}''(z)\left[\int_{-\infty}^{z}\alpha_1(z')dz'\right]^2 + \frac{3}{4}\alpha_1(z){\alpha_1}'(z)\int_{-\infty}^{z}\left(-\alpha_1(z')\right)dz' \\ & - \frac{1}{16}\int_{-\infty}^{z}{\alpha_1}'(z')\int_{-\infty}^{z}{\alpha_1}'(z'')\alpha_1(z'+z''-z)dz''dz'. \end{aligned} \tag{3.24}$$

To get the final expression of the right-hand side (R.H.S.) term, we will substitute into the above equation the expression of α_2 in Shaw et al. (2002) for the one-parameter case.

$$\alpha_2(z) = -\frac{1}{2}\left[{\alpha_1}^2(z) + {\alpha_1}'(z)\int_{-\infty}^{z}\alpha_1(z')dz'\right]. \tag{3.25}$$

Substituting equation (3.25) back into equation (3.24), we find,

$$\begin{aligned} R.H.S. = & \frac{1}{2}\alpha_1(z)\left[{\alpha_1}^2(z) + {\alpha_1}'(z)\int_{-\infty}^{z}\alpha_1(z')dz'\right] - \frac{5}{16}{\alpha_1}^3(z) \\ & + \frac{1}{4}{\alpha_1}'(z)\int_{-\infty}^{z}dz'\left[{\alpha_1}^2(z') + {\alpha_1}'(z')\int_{-\infty}^{z'}\alpha_1(z'')dz''\right] \\ & + \frac{1}{4}\frac{d}{dz}\left[{\alpha_1}^2(z) + {\alpha_1}'(z)\int_{-\infty}^{z}\alpha_1(z')dz'\right]\int_{-\infty}^{z}\alpha_1(z')dz' - \frac{1}{8}{\alpha_1}''(z)\left[\int_{-\infty}^{z}\alpha_1(z')dz'\right]^2 \\ & - \frac{3}{4}\alpha_1(z){\alpha_1}'(z)\int_{-\infty}^{z}\alpha_1(z')dz' - \frac{1}{16}\int_{-\infty}^{z}{\alpha_1}'(z')\int_{-\infty}^{z}{\alpha_1}'(z'')\alpha_1(z'+z''-z)dz''dz'. \end{aligned} \tag{3.26}$$

After collecting the same terms and using derivative skills, and letting the R.H.S. equal the left-hand side (L.H.S.), we obtain,

$$\begin{aligned}\alpha_3(z) =& \frac{3}{16}{\alpha_1}^3(z) + \frac{3}{4}\alpha_1(z)\frac{d\alpha_1(z)}{dz}\int_{-\infty}^{z}\alpha_1(z'))dz' \\ &+ \frac{1}{8}\frac{d^2\alpha_1(z)}{dz^2}\left[\int_{-\infty}^{z}\alpha_1(z')dz'\right]^2 - \frac{1}{8}\frac{d\alpha_1(z)}{dz}\int_{-\infty}^{z}{\alpha_1}^2(z')dz' \\ &- \frac{1}{16}\int_{-\infty}^{z}{\alpha_1}'(z')\int_{-\infty}^{z}{\alpha_1}'(z'')\alpha_1(z'+z''-z)dz''dz'.\end{aligned} \tag{3.27}$$

Equation (3.27) is exactly $\alpha_3(z)$ for the 1D one-parameter acoustic medium at normal incidence case in Shaw (2005), which indicates the calculation of the 3^{rd} order term is effective.

3.3.3 Leading order imaging series and its closed form

In the following calculation, we try to further simplify some integrals in equation (3.22) by collecting some similar terms and using the 2^{nd} term result, equation (3.5).

We consider the following two integrals in equation (3.22),

$$\begin{aligned}&-\frac{1}{2}\frac{1}{\cos^4\theta}{\alpha_2}'(z)\int_{-\infty}^{z}\left[\alpha_1(z')-\beta_1(z')\right]dz' + \frac{1}{2}\left(\tan^4\theta-1\right){\beta_2}'(z)\int_{-\infty}^{z}\left[\alpha_1(z')-\beta_1(z')\right]dz' \\ &= -\frac{1}{2}\frac{1}{\cos^2\theta}\left(\tan^2\theta+1\right){\alpha_2}'(z)\int_{-\infty}^{z}\left[\alpha_1(z')-\beta_1(z')\right]dz' \\ &\quad + \frac{1}{2}\frac{1}{\cos^2\theta}\left(\tan^2\theta-1\right){\beta_2}'(z)\int_{-\infty}^{z}\left[\alpha_1(z')-\beta_1(z')\right]dz' \\ &= -\frac{1}{2}\frac{1}{\cos^2\theta}\frac{d}{dz}\left[\frac{1}{\cos^2\theta}\alpha_2(z)+\left(1-\tan^2\theta\right)\beta_2(z)\right]\int_{-\infty}^{z}\left[\alpha_1(z')-\beta_1(z')\right]dz'.\end{aligned} \tag{3.28}$$

where we notice that the total derivative part outside the integral is exactly the ISS 2^{nd} term, equation (3.5).

Now substituting equation (3.5) into equation (3.28),

$$\begin{aligned}
&-\frac{1}{2}\frac{1}{\cos^4\theta}{\alpha_2}'(z)\int_{-\infty}^{z}\left[\alpha_1(z')-\beta_1(z')\right]dz' \\
&+\frac{1}{2}\left(\tan^4\theta-1\right){\beta_2}'(z)\int_{-\infty}^{z}\left[\alpha_1(z')-\beta_1(z')\right]dz' \\
&=\frac{3}{4}\frac{1}{\cos^4\theta}\left[\alpha_1(z)-\beta_1(z)\right]\frac{d\mathcal{D}(z,\theta)}{dz}\int_{-\infty}^{z}\left[\alpha_1(z')-\beta_1(z')\right]dz' \\
&+\frac{1}{2}\frac{1}{\cos^2\theta}\beta_1(z)\frac{d\mathcal{D}(z,\theta)}{dz}\int_{-\infty}^{z}\left[\alpha_1(z')-\beta_1(z')\right]dz' \\
&-\frac{1}{2}\frac{1}{\cos^4\theta}\left[\alpha_1(z)-\beta_1(z)\right]\frac{d\beta_1(z)}{dz}\int_{-\infty}^{z}\left[\alpha_1(z')-\beta_1(z')\right]dz' \\
&+\frac{1}{4}\frac{1}{\cos^4\theta}\frac{d^2\mathcal{D}(z,\theta)}{dz^2}\left[\int_{-\infty}^{z}(\alpha_1(z')-\beta_1(z'))dz'\right]^2.
\end{aligned} \tag{3.29}$$

where we define a new quantity $\mathcal{D}(z,\theta)$ in the above result, called the"imaging composite" and expressed as,

$$\mathcal{D}(z,\theta)\equiv\frac{1}{\cos^2\theta}\alpha_1(z)+\left(1-\tan^2\theta\right)\beta_1(z). \tag{3.30}$$

This new quantity $\mathcal{D}(z,\theta)$ is the linear term, equation (3.4), except for a constant.

Similarly, we also notice the following integrals in equation (3.22),

$$\begin{aligned}
&-\frac{1}{8}\frac{1}{\cos^6\theta}{\alpha_1}''(z)\left[\int_{-\infty}^{z}(\alpha_1(z')-\beta_1(z'))dz'\right]^2 \\
&+\frac{1}{8}\frac{1}{\cos^4\theta}\left(\tan^2\theta-1\right){\beta_1}''(z)\left[\int_{-\infty}^{z}(\alpha_1(z')-\beta_1(z'))dz'\right]^2 \\
&=-\frac{1}{2}\frac{1}{\cos^4\theta}\frac{d^2\mathcal{D}(z,\theta)}{dz^2}\left[\int_{-\infty}^{z}(\alpha_1(z')-\beta_1(z'))dz'\right]^2.
\end{aligned} \tag{3.31}$$

and,

$$\begin{aligned}
&-\frac{1}{4}\frac{1}{\cos^4\theta}{\beta_1}'(z)\int_{-\infty}^{z}\left[\alpha_1(z')-\beta_1(z')\right]^2dz' \\
&-\frac{1}{8}\frac{1}{\cos^6\theta}\left[{\alpha_1}'(z)-{\beta_1}'(z)\right]\int_{-\infty}^{z}\left[\alpha_1(z')-\beta_1(z')\right]^2dz' \\
&=-\frac{1}{\cos^4\theta}\frac{d\mathcal{D}(z,\theta)}{dz}\int_{-\infty}^{z}\left[\alpha_1(z')-\beta_1(z')\right]^2dz'.
\end{aligned} \tag{3.32}$$

Substituting all of the above equations back into the equation (3.22) and combining similar terms, we obtain the 3^{rd} term in terms of the new defined imaging composite $\mathcal{D}(z,\theta)$,

$$
\begin{aligned}
&\frac{1}{\cos^2\theta}\alpha_3(z) + \left(1-\tan^2\theta\right)\beta_3(z) \\
&= -\frac{1}{\cos^4\theta}\left[\alpha_1(z)-\beta_1(z)\right]\left[\alpha_2(z)-\beta_2(z)\right] + \frac{1}{4}\frac{1}{\cos^2\theta}{\beta_1}^2(z)\left[\alpha_1(z)-\beta_1(z)\right] \\
&+ \frac{1}{8}\frac{1}{\cos^4\theta}\beta_1(z)\left[\alpha_1(z)-\beta_1(z)\right]^2 - \frac{5}{16}\frac{1}{\cos^6\theta}\left[\alpha_1(z)-\beta_1(z)\right]^3 \\
&- \frac{1}{2}\frac{1}{\cos^2\theta}\frac{d\mathcal{D}(z,\theta)}{dz}\int_{-\infty}^{z}\left[\alpha_2(z')-\beta_2(z')\right]dz' \\
&+ \frac{3}{4}\frac{1}{\cos^4\theta}\left[\alpha_1(z)-\beta_1(z)\right]\frac{d\mathcal{D}(z,\theta)}{dz}\int_{-\infty}^{z}\left[\alpha_1(z')-\beta_1(z')\right]dz' \\
&+ \frac{1}{2}\frac{1}{\cos^2\theta}\beta_1(z)\frac{d\mathcal{D}(z,\theta)}{dz}\int_{-\infty}^{z}\left[\alpha_1(z')-\beta_1(z')\right]dz' \\
&- \frac{1}{8}\frac{1}{\cos^4\theta}\frac{d\mathcal{D}(z,\theta)}{dz}\int_{-\infty}^{z}\left[\alpha_1(z')-\beta_1(z')\right]^2dz' \\
&+ \frac{1}{8}\frac{1}{\cos^4\theta}\frac{d^2\mathcal{D}(z,\theta)}{dz^2}\left[\int_{-\infty}^{z}\left(\alpha_1(z')-\beta_1(z')\right)dz'\right]^2 \\
&- \frac{1}{2}\frac{1}{\cos^4\theta}\left[\alpha_1(z)-\beta_1(z)\right]\frac{d\beta_1(z)}{dz}\int_{-\infty}^{z}\left[\alpha_1(z')-\beta_1(z')\right]dz' \\
&+ \frac{1}{4}\frac{1}{\cos^4\theta}\left(3\tan^2\theta+1\right)\alpha_1(z)\frac{d\beta_1(z)}{dz}\int_{-\infty}^{z}\left[\alpha_1(z')-\beta_1(z')\right]dz' \\
&+ \frac{1}{4}\frac{1}{\cos^4\theta}\left(3\tan^2\theta-1\right)\beta_1(z)\frac{d\beta_1(z)}{dz}\int_{-\infty}^{z}\left[\alpha_1(z')-\beta_1(z')\right]dz' \\
&- \frac{3}{4}\frac{1}{\cos^6\theta}\alpha_1(z)\frac{d\alpha_1(z)}{dz}\int_{-\infty}^{z}\left[\alpha_1(z')-\beta_1(z')\right]dz' \\
&+ \frac{3}{4}\frac{1}{\cos^6\theta}\beta_1(z)\frac{d\alpha_1(z)}{dz}\int_{-\infty}^{z}\left[\alpha_1(z')-\beta_1(z')\right]dz' \\
&+ MUL.
\end{aligned}
\tag{3.33}
$$

where the multiple-related term $MUL.$ is expressed in equation (3.23).

The examination on the imaging-only terms shown in the 2^{nd} order results (Zhang

and Weglein, 2005) indicates that only the integral terms of the difference between the two parameters, in the 3^{rd} order *ISS* term, will contribute to the imaging algorithm. The philosophy of collecting similar but higher order imaging-only terms leads to the consideration of the following term in equation (3.33):

$$\frac{1}{8}\frac{1}{\cos^4\theta}\frac{d^2\mathcal{D}(z,\theta)}{dz^2}\left[\int_{-\infty}^{z}(\alpha_1(z')-\beta_1(z'))\,dz'\right]^2$$

Similarly, we can rewrite equation (3.4) and the 2^{nd} order imaging-only term in equation (3.5) in terms of the defined imaging composite $\mathcal{D}(z,\theta)$:

$$-\frac{4}{\rho_0}D(z,\theta)=\mathcal{D}(z,\theta). \tag{3.34}$$

$$-\frac{1}{2}\frac{1}{\cos^2\theta}\frac{d\mathcal{D}(z,\theta)}{dz}\int_{-\infty}^{z}[\alpha_1(z')-\beta_1(z')]\,dz'$$

The above three terms are imaging terms identified from the first three *ISS* terms that are going to be collected and taken as the basis to identify the following imaging sub-series. An observation through the first three imaging terms provides a mathematical pattern, called "leading order imaging sub-series" (*LOIS*):

$$\mathscr{D}^{LOIS}(z,\theta)=\sum_{n=0}^{\infty}\frac{\left(-\frac{1}{2}\frac{1}{\cos^2\theta}\right)^n}{n!}\frac{d^n\mathcal{D}(z,\theta)}{dz^n}\left[\int_{-\infty}^{z}(\alpha_1(z')-\beta_1(z'))\,dz'\right]^n. \tag{3.35}$$

Every term in this *LOIS* is an imaging-only term and appears in the higher *ISS* terms with increasing n.

Employing the same mathematical procedure as Shaw (2005), the *LOIS* is a Taylor expansion series of the following imaging function, called as "leading order

imaging closed form":

$$\sum_{n=0}^{\infty} \frac{\left(-\frac{1}{2}\frac{1}{\cos^2\theta}\right)^n}{n!} \frac{d^n \mathcal{D}(z,\theta)}{dz^n} \left[\int_{-\infty}^{z} \left(\alpha_1(z') - \beta_1(z')\right) dz'\right]^n$$
$$= \mathcal{D}\left(z - \frac{1}{2}\frac{1}{\cos^2\theta}\int_{-\infty}^{z} \left(\alpha_1(z') - \beta_1(z')\right) dz'\right). \tag{3.36}$$

Noticing the quantity $\mathcal{D}$ defined in equation (3.30), the above leading order imaging closed form is exactly the conjectured imaging algorithm proposed by Weglein in equation (3.7).

Shutting down the density variation, namely, letting $\beta(z) = 0$, and therefore, $\beta_1(z) = 0$, equation (3.36) will be simplified as,

$$\sum_{n=0}^{\infty} \frac{\left(-\frac{1}{2}\frac{1}{\cos^2\theta}\right)^n}{n!} \frac{d^n \alpha_1(z)}{dz^n} \left[\int_{-\infty}^{z} \alpha_1(z') dz'\right]^n$$
$$= \alpha_1\left(z - \frac{1}{2}\frac{1}{\cos^2\theta}\int_{-\infty}^{z} \alpha_1(z') dz'\right). \tag{3.37}$$

This equation is exactly the leading order imaging sub-series and closed form for the 1D velocity-only changed acoustic medium (Shaw et al., 2002; Shaw, 2005). For the one parameter case, the imaging algorithm recognizes the one parameter (velocity) as the imaging object, and the shifted quantity in the $\alpha_1(z)$ depends on the integral of the 1^{st} order approximation of the velocity parameter to the uncorrected location.

Unlike the one parameter case, there are two parameters to be imaged for the acoustic medium with both density and velocity variations. So which one should be imaged? Or, should both be imaged, in the way as the above one parameter case? The leading order imaging closed form, equation (3.36), answers these questions: it recognizes the imaging of the two parameters as an imaging composite $\mathcal{D}(z,\theta)$. In

fact, the imaging composite $\mathcal{D}(z,\theta)$ is related with the seismic data in the pseudo-depth domain, presenting in equation (3.34). Therefore, the closed form can be further identified as a shifted seismic data set in the re-scaled time domain using reference velocity, called as pseudo-depth domain, i.e.,

$$\begin{aligned}&\mathcal{D}\left(z-\frac{1}{2}\frac{1}{\cos^2\theta}\int_{-\infty}^{z}\left(\alpha_1(z')-\beta_1(z')\right)dz'\right)\\&=-\frac{4}{\rho_0}D\left(z-\frac{1}{2}\frac{1}{\cos^2\theta}\int_{-\infty}^{z}\left(\alpha_1(z')-\beta_1(z')\right)dz'\right).\end{aligned}\tag{3.38}$$

This imaging result is valuable and indicates that for multi-parameter medium imaging, the algorithm itself will recognize the existence of different parameters in the medium, since reflection happens when medium properties change. The inverse scattering imaging algorithm captures the medium property changes as a composite change, in other words, it images the medium structure in the composite when medium property changes occur. Meanwhile, the shifted quantity in the above imaging algorithm is expressed as the integral of the difference between the 1^{st} order approximations of the two parameters, which is only taking care of the velocity change (Zhang and Weglein, 2005). It will be automatically shut down when there is no velocity variation in the medium (then there is no imaging necessity). This indicates the fact that inverse scattering theory is a purposeful perturbation theory – tasks will 'wake up' only when needed by the medium. Another surprising capability of the *ISS* imaging algorithm is that it will shut down each imaging term at the first step when it knows there is no velocity change, i.e. when $\alpha_1(z)-\beta_1(z)=0$, and hence each imaging term related with the integral of the difference will be dead to zero, immediately. This indicates the *ISS* is an instantly responsive series.

3.4 Analytic analyses

In this section, as follow-up multiparameter imaging research, a series of initial analytic analyses for a laterally invariant two-parameter (velocity and density) acoustic medium are presented to examine how effectively the 1D acoustic two-parameter *LOIS* and *HOIS* imaging algorithms, equation (3.7) and equation (3.10), are working towards a satisfactory level in the multiparameter imaging toolbox.

3.4.1 1D two-parameter acoustic model

The model to be tested is shown in Figure 3.1. We will consider only two primaries reflected from the 1^{st} interface and the 2^{nd} interface, since the *ISS* imaging task has assumed that all seismic events other than primaries have already been removed. Next we will analytically write out primaries-only data based on this model.

3.4.2 1D analytic data preparation

Since both the *LOIS* and *HOIS* multi-parameter imaging algorithms are data-driven algorithms, we will first prepare analytic data for the above three layer's 1D acoustic model. The derivation of the imaging algorithms assumes an experiment with line sources and line receivers. The data expressed in the end of this subsection is after plane wave decomposition, which is an immediate and proper input to the imaging algorithms to be tested.

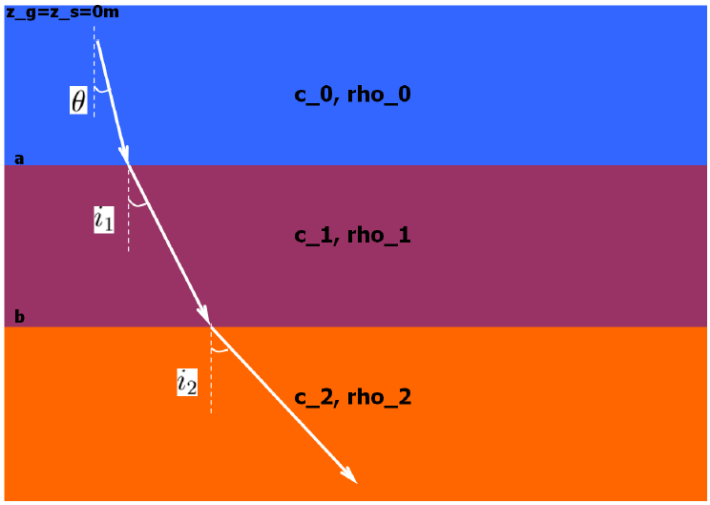

Figure 3.1: *A 1D acoustic model with both velocity*(c_0, c_1, c_2) *and density* (ρ_0, ρ_1, ρ_2) *variations in the three layers, where* θ, i_1, i_2 *are three incident angles in the layers, respectively;* a *and* b *are two constants to express the real depths of the two interfaces. For simplicity, both source depth* z_s *and receiver depth* z_g *are set to zero.*

We will first write down the analytic reflection and transmission coefficients first according to the different impedance in the three layers. For plane wave incidence at different incident angles, the impedance can be expressed as,

$$\begin{aligned} I_0 &= \frac{c_0\rho_0}{\cos\theta} \\ I_1 &= \frac{c_1\rho_1}{\cos i_1} \\ I_2 &= \frac{c_2\rho_2}{\cos i_2} \end{aligned} \tag{3.39}$$

For 1D layered media, Snell's law says that the value of the horizontal slowness p is constant through different layers, and hence provides the following relation among

the three incident angles in the three layers of the medium.

$$p = \frac{\sin\theta}{c_0} = \frac{\sin i_1}{c_1} = \frac{\sin i_2}{c_2} \tag{3.40}$$

Employing the above relation, we can rewrite the above impedance as,

$$\begin{aligned} I_0 &= \frac{c_0\rho_0}{\cos\theta} = \frac{c_0\rho_0}{\sqrt{1-c_0^2p^2}} = \frac{c_0\rho_0}{x_0} \\ I_1 &= \frac{c_1\rho_1}{\cos i_1} = \frac{c_1\rho_1}{\sqrt{1-c_1^2p^2}} = \frac{c_1\rho_1}{x_1} \\ I_2 &= \frac{c_2\rho_2}{\cos i_2} = \frac{c_2\rho_2}{\sqrt{1-c_2^2p^2}} = \frac{c_2\rho_2}{x_2} \end{aligned} \tag{3.41}$$

where $x_i = \sqrt{1-c_i^2p^2}, \quad i = 0, 1, 2.$

Now we can express the reflection and transmission coefficients as,

$$\begin{aligned} R_0(\theta) &= \frac{I_1 - I_0}{I_1 + I_0} \\ R_1(\theta) &= \frac{I_2 - I_1}{I_2 + I_1} \\ T_{01}(\theta) &= 1 - R_0 = \frac{2I_0}{I_1 + I_0} \\ T_{10}(\theta) &= 1 + R_0 = \frac{2I_1}{I_1 + I_0} \end{aligned} \tag{3.42}$$

We will write down the analytic data in the frequency domain.

$$\widetilde{D}^{PP}(\omega,\theta) = \rho_0 R_0(\theta)\frac{e^{2i\nu_g a}}{4\pi i\nu_g} + \rho_0 T_{01}(\theta)R_1(\theta)T_{10}(\theta)\frac{e^{2i\nu_g a + 2iq_g(b-a)}}{4\pi i\nu_g} \tag{3.43}$$

where the two vertical wave vectors in the first two layers are expressed as,

$$\nu_g = \frac{\omega\cos\theta}{c_0} = \frac{\omega}{c_0}\sqrt{1-c_0^2p^2} = \frac{\omega}{c_0}x_0 \tag{3.44}$$

and,

$$q_g = \frac{\omega\cos i_1}{c_1} = \frac{\omega}{c_1}\sqrt{1-c_1^2p^2} = \frac{\omega}{c_1}x_1 \tag{3.45}$$

Performing an inverse Fourier transform w.r.t. ν_g, we can obtain the PP data in the pseudo-depth domain,

$$D^{PP}(z,\theta) = -\rho_0 R_0(\theta) H(z-a) - \rho_0 R_1'(\theta) H(z-b'(\theta)) \tag{3.46}$$

where the variable z is the Fourier conjugator of ν_g, and

$$\begin{aligned} b'(\theta) &= a + (b-a)\frac{c_0\sqrt{1-c_1^2p^2}}{c_1\sqrt{1-c_0^2p^2}} = a + (b-a)\frac{c_0 x_1}{c_1 x_0} \\ R_1'(\theta) &= T_{01}(\theta) R_1(\theta) T_{10}(\theta) \end{aligned} \tag{3.47}$$

Equation (3.46) is the analytic data we prepared for the purpose of the following tests on the two-parameter *LOIS* and *HOIS* imaging algorithms. The data in equation (3.46) is expressed in the pseudo-depth domain since it is migrated with a constant reference velocity, c_0, which is in agreement with the velocity in the first layer. Generally the value of c_0 is the water speed (1500 m/s). After the constant velocity migration, the water bottom, i.e. the 1^{st} interface, is located exactly since we have correct migration velocity for the 1^{st} layer, but the 2^{nd} interface is wrongly located to $b'(\theta)$ instead of its real depth of b. It is understandable since we used a wrong migration velocity, c_0, instead of its real velocity c_1. To understand whether $b'(\theta)$ is deeper or shallower than its real depth b, we need to do further analysis on this quantity.

Let us rewrite the expression of $b'(\theta)$ in equation (3.47) by using equation (3.40),

$$b'(\theta) = a + (b-a)\frac{c_0}{c_1}\sqrt{1 + \frac{c_0^2 - c_1^2}{c_0^2}\tan^2\theta} \tag{3.48}$$

We will discuss two cases:

(1). for $c_0 < c_1$, $c_0^2 - c_1^2 < 0$. Then, $b'(\theta) < b$ and $b'(\theta) \downarrow$ with $\theta \uparrow$;

(2). for $c_0 > c_1$, $c_0^2 - c_1^2 > 0$. Then, $b'(\theta) > b$ and $b'(\theta) \uparrow$ with $\theta \uparrow$.

In another words, the migrated depth of the 2^{nd} interface is shallower than its real depth when the migration velocity is slower than its real velocity, and deeper than its real depth when the migration velocity is faster than its real velocity. It is a reasonable result since constant velocity migration is a linear migration, i.e. rescaling the time axis of the data set to depth axis by a constant velocity. We emphasize this point here to show a difference between the constant velocity migration and the *ISS LOIS* and *HOIS* imaging shown later where the relation between time domain and depth domain of the migration is no longer linear since the later imaging occurrs in a non-linear world. More details on this point will be discussed in the following subsections.

3.4.3 Analytic calculation of *LOIS* closed form

Now we can use the data prepared in equation (3.46) as an input to the *LOIS* two-parameter imaging algorithm. Recall that in Zhang and Weglein (2005),

$$D^{PP}(z,\theta) = -\frac{\rho_0}{4}\left[\frac{1}{\cos^2\theta}\alpha_1(z) + \left(1-\tan^2\theta\right)\beta_1(z)\right] \tag{3.49}$$

The above equation is solved to obtain $\alpha_1(z) - \beta_1(z)$, using two separate incident angles,

$$\alpha_1(z) - \beta_1(z) = -\frac{4}{\rho_0}\frac{D^{PP}(z,\theta_1) - D^{PP}(z,\theta_2)}{\tan^2(\theta_1) - \tan^2(\theta_2)} \tag{3.50}$$

Then we insert the analytic expression of the data with different incident angles prepared in the previous subsection,

$$\begin{aligned}\alpha_1(z)-\beta_1(z)=\frac{4}{\tan^2(\theta_1)-\tan^2(\theta_2)}[&(R_0(\theta_1)-R_0(\theta_2))\,H(z-a)\\&+R_1'(\theta_1)H(z-b'(\theta_1))\\&-R_1'(\theta_2)H(z-b'(\theta_2))]\end{aligned}\tag{3.51}$$

Now we can calculate the integral with the above equation as the integrand, and hence get the shifted quantity,

$$\begin{aligned}\triangle z_{shift}&=\frac{1}{2\cos^2\theta}\int_{-\infty}^{z}dz'\,(\alpha_1(z')-\beta_1(z'))\\&=\frac{2}{\tan^2(\theta_1)-\tan^2(\theta_2)}\frac{1}{\cos^2\theta}[(R_0(\theta_1)-R_0(\theta_2))\,(z-a)H(z-a)\\&+R_1'(\theta_1)(z-b'(\theta_1))H(z-b'(\theta_1))-R_1'(\theta_2)(z-b'(\theta_2))H(z-b'(\theta_2))]\end{aligned}\tag{3.52}$$

Therefore, the migration result, i.e. the imaging composite equation (3.30), using the *LOIS* closed form is an *FK Migration* of the data set *shifted by a quantity as a function of* "z", i.e.

$$\begin{aligned}\mathscr{D}^{LOIS}(z,\theta)&=-\frac{4}{\rho_0}D^{PP}(z-\triangle z_{shift},\theta)\\&=4R_0(\theta)H(z-\triangle z_{shift}-a)+4R_1'(\theta)H(z-\triangle z_{shift}-b'(\theta))\end{aligned}\tag{3.53}$$

3.4.4 Analysis on the shifted quantity

Now we will perform some analysis on the above *LOIS* migration result.

(1). If $z\le a$, then

$$\triangle z_{shift}\equiv 0.\tag{3.54}$$

(2). If $a < z \leq b'(\theta_1)$ *and* $z \leq b'(\theta_2)$, then

$$\triangle z_{shift} = \frac{2}{\tan^2(\theta_1) - \tan^2(\theta_2)} \frac{1}{\cos^2\theta} \left[(z-a) \left(R_0(\theta_1) - R_0(\theta_2) \right) \right]. \tag{3.55}$$

(3). If $z > a$ *and* $b'(\theta_1) < z \leq b'(\theta_2)$, then

$$\triangle z_{shift} = \frac{2}{\tan^2(\theta_1) - \tan^2(\theta_2)} \frac{1}{\cos^2\theta} \left[(z-a) \left(R_0(\theta_1) - R_0(\theta_2) \right) + (z - b'(\theta_1)) R_1'(\theta_1) \right]. \tag{3.56}$$

(4). If $z > a$ *and* $b'(\theta_2) < z \leq b'(\theta_1)$, then

$$\triangle z_{shift} = \frac{2}{\tan^2(\theta_1) - \tan^2(\theta_2)} \frac{1}{\cos^2\theta} \left[(z-a) \left(R_0(\theta_1) - R_0(\theta_2) \right) - (z - b'(\theta_2)) R_1'(\theta_2) \right]. \tag{3.57}$$

(5). If $z > a$, $z > b'(\theta_1)$ *and* $z > b'(\theta_2)$, then

$$\begin{aligned} \triangle z_{shift} = & \frac{2}{\tan^2(\theta_1) - \tan^2(\theta_2)} \frac{1}{\cos^2\theta} [(z-a) \left(R_0(\theta_1) - R_0(\theta_2) \right) \\ & + (z - b'(\theta_1)) R_1'(\theta_1) - (z - b'(\theta_2)) R_1'(\theta_2)]. \end{aligned} \tag{3.58}$$

Let us check the above shifted quantity for a simple 1D acoustic model with constant velocity, i.e. $c_0 = c_1 = c_2$, but with varied density. For this model, the reflection and transmission coefficients, recalling expressions in equation (3.41) and equation (3.42), will be simplified ,

$$\begin{aligned} R_0 &= \frac{\rho_1 - \rho_0}{\rho_1 + \rho_0} \\ R_1 &= \frac{\rho_2 - \rho_1}{\rho_2 + \rho_1} \\ T_{01} &= 1 - R_0 \\ T_{10} &= 1 + R_0 \end{aligned} \tag{3.59}$$

Notice that the reflection and transmission coefficients are independent of θ. This leads to the following relation,

$$R_0(\theta_1) = R_0(\theta_2) \quad R_1'(\theta_1) = R_1'(\theta_2) \tag{3.60}$$

Similarly, the pseudo-depth expression of equation (3.48) becomes,

$$b'(\theta) = a + (b - a) = b \tag{3.61}$$

The pseudo-depth is also independent of θ, and it is equal to the real depth of the 2nd interface, since the velocities for all three layers are the same in this case and equal to the reference velocity of the migration.

Therefore, the shifted quantities in the above five cases are all zero, i.e.

$$\triangle z_{shift} \equiv 0. \tag{3.62}$$

This means that for the 1D acoustic model with constant velocity but varied density, the dataset after *FK migration with constant velocity,* c_0*,* has correctly located all interfaces. It is reasonable since all layers in this case have the same and correct velocity c_0.

What about the case with three different velocities in three layers? From the math expression of the shifted quantity shown in the above five cases, we can tell the value of the shifted quantity is actually dependent on the reflection and transmission coefficients at two different incident angles; in other words, when the reference velocity is different from the real velocity, the *ISS LOIS* imaging algorithm will *use velocity information* "buried" in the reflection and transmission coefficients through

their *non-linear communication* at two different incident angles, and this *non-linear communication* will be carried on through a depth duration wherever its real velocity is different from the reference velocity. As discussed in the Appendix of Zhang and Weglein (2005), the integrand of the shifted quantity is a linear estimate of velocity changes in the media. Therefore, the more accurate the linear estimate of the velocity changes, the closer the migrated interfaces are to their real depths.

3.4.5 Numerical evaluations using analytic data

For a 1D acoustic model with both density and velocity variation, it is not easy to "read" from the analytic expression of the shifted quantity how well it is for locating the real depths. In this section, we will do some numerical evaluations on the above three-layer acoustic medium using the *ISS LOIS* imaging algorithm expressed in equation (3.7), and the extended acoustic *ISS HOIS* imaging algorithm expressed in equation (3.10) by varying the values of density and velocity in the models.

First, we will demonstrate how sensitive the *LOIS* imaging algorithm is to the changes of the velocity parameter, and then we will show the imaging improvement using the *HOIS* imaging algorithm by comparing its results with the *LOIS* results. Further, we will study how sensitive the *LOIS* and *HOIS* imaging algorithms are to the changes in the density parameter. Finally, the effect of depth duration in the model on the imaging capability of both imaging algorithms will be studied in the end of this section.

We will first fix the two interface depths a=200 m and b=400 m in the models.

In Figure 3.2, we show a comparison of imaging results between constant velocity migration in the left most panel and the *ISS LOIS* imaging algorithm in the middle panel. For the model we tested, both methods exactly located the 1^{st} interface and mislocated the 2^{nd} interface - the constant velocity migration method undermigrated the 2^{nd} interface since it assumed a constant velocity (c_0=1500 m/s) which is less than its real velocity (c_1=1600 m/s) in the 2^{nd} layer, while the *ISS LOIS* imaging algorithm overmigrated the 2^{nd} interface although the method also employs the same constant reference velocity (c_0=1500 m/s) with the former method. Again, this result indicates that the *ISS LOIS* imaging algorithm developed from a *non-linear* series is conceptually different from the conventional migration method, the constant velocity migration for example, which originated from a *linear* imaging world. It is apparent that the *ISS LOIS* imaging algorithm pushed its imaging 2^{nd} interface much closer to its real depth than the constant velocity migration result, especially within the small incident angle range.

To show the purposeful perturbation of the *ISS LOIS* imaging algorithm, we also present the imaging result of a model with no velocity changes but only density changes in the right most panel of Figure 3.2. The result shows both interfaces are exactly located, since a right velocity model ($c_0 = c_1 = c_2 = 1500$ m/s) is provided in which case the *ISS LOIS* imaging algorithm will shut down immediately, and the dataset of water-speed FK migration result has exactly located the reflectors in the 1^{st} term of the *ISS*.

In the following tests, we will demonstrate the sensitivity of the *ISS LOIS* imaging algorithm to the changes of velocity parameter in the models. In Figure 3.3, the *LOIS*

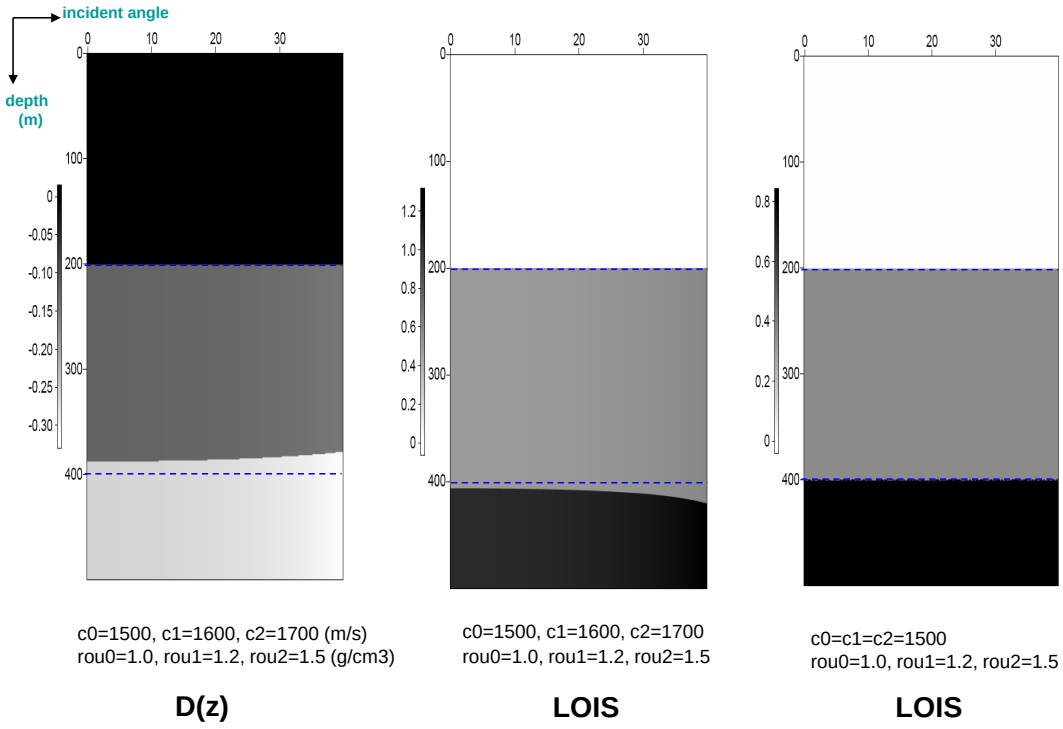

Figure 3.2: *Imaging comparison 1: left figure is a result of constant velocity (c_0=1500 m/s) migration, middle and right figures are results using two-parameter ISS LOIS imaging algorithm, where the blue dashed lines are the real depths of the two interfaces in the model. The color scale beside each graph denotes the value of reflection amplitude in each layer.*

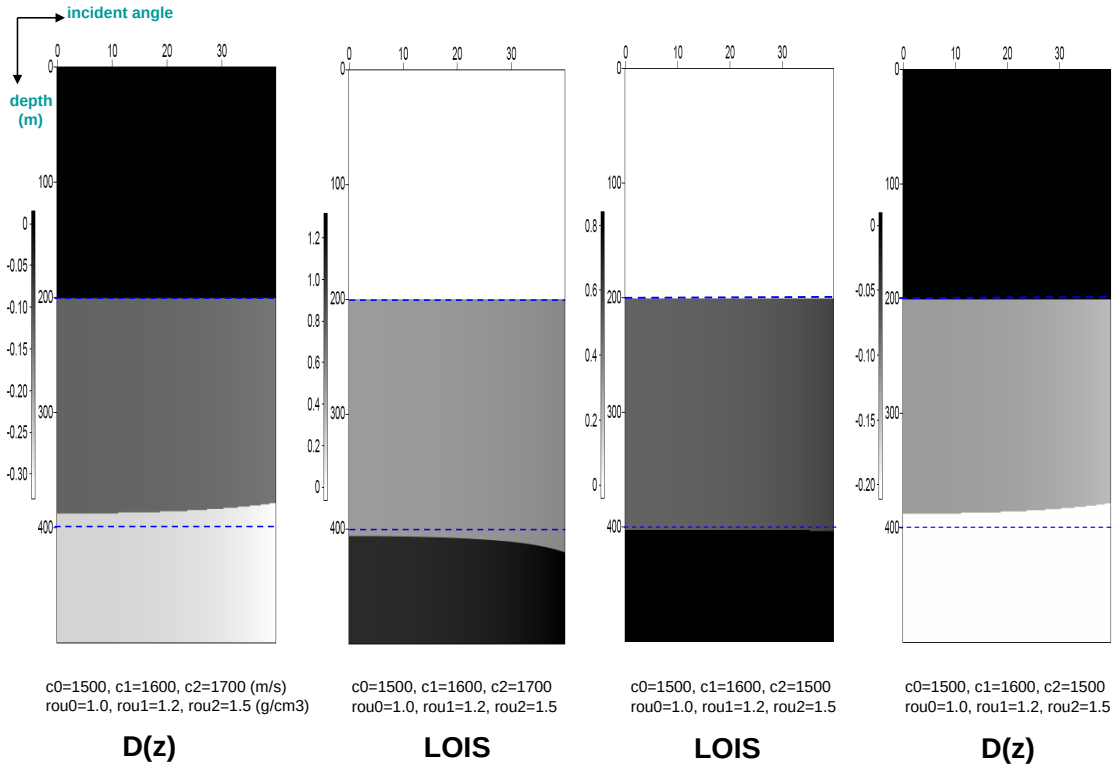

Figure 3.3: *Imaging comparison 2: the outer two figures are the results of constant velocity (c_0=1500 m/s) migration, the inner two figures are the corresponding results using two-parameter ISS LOIS imaging algorithm, where the blue dashed lines are the real depths of the two interfaces in the model. The color scale beside each graph denotes the value of reflection amplitude in each layer.*

result comparison between the middle two panels shows that the *ISS LOIS* imaging algorithm used amplitude information from deeper layers, since the velocities are the same in the first two layers but different in the third layer - one is faster than the first layer velocity, the other is same with the first layer velocity. It seems the *ISS LOIS* imaging algorithm preferrs the latter velocity model. But both results of the *LOIS* are better than the constant velocity migration results for locating the 2^{nd} reflector, as can be seen from the direct comparison among the results in the four panels of Figure 3.3.

The imaging results in Figure 3.4 demonstrate that for a velocity model of "slow/faster/same as 1^{st} layer", the *ISS LOIS* imaging algorithm preferrs a larger velocity contrast in the sense of locating the 2^{nd} reflector, especially within small incident angles. This observation further indicates that the *ISS LOIS* imaging algorithm used amplitude information of deeper events. For comparison purpose, the constant velocity migration result is also put in the figure 3.4.

Figure 3.5 and Figure 3.6 show the imaging results for a velocity model of "faster/slower/same as 1^{st} layer", in which case the *ISS LOIS* imaging algorithm shows a weaker imaging capability for a model with larger velocity contrast than smaller velocity contrast. Again, it demonstrates the amplitude information of deeper events is involved into the imaging algorithm.

We mentioned in previous section that $\alpha_1 - \beta_1$ is a linear estimate of the velocity changes between the real velocity model and the reference velocity. When there are no velocity changes, $\alpha_1 - \beta_1$ is zero, and the *ISS LOIS* imaging algorithm shuts down immediately. The result in the most right panel in Figure 3.7 demonstrates this key

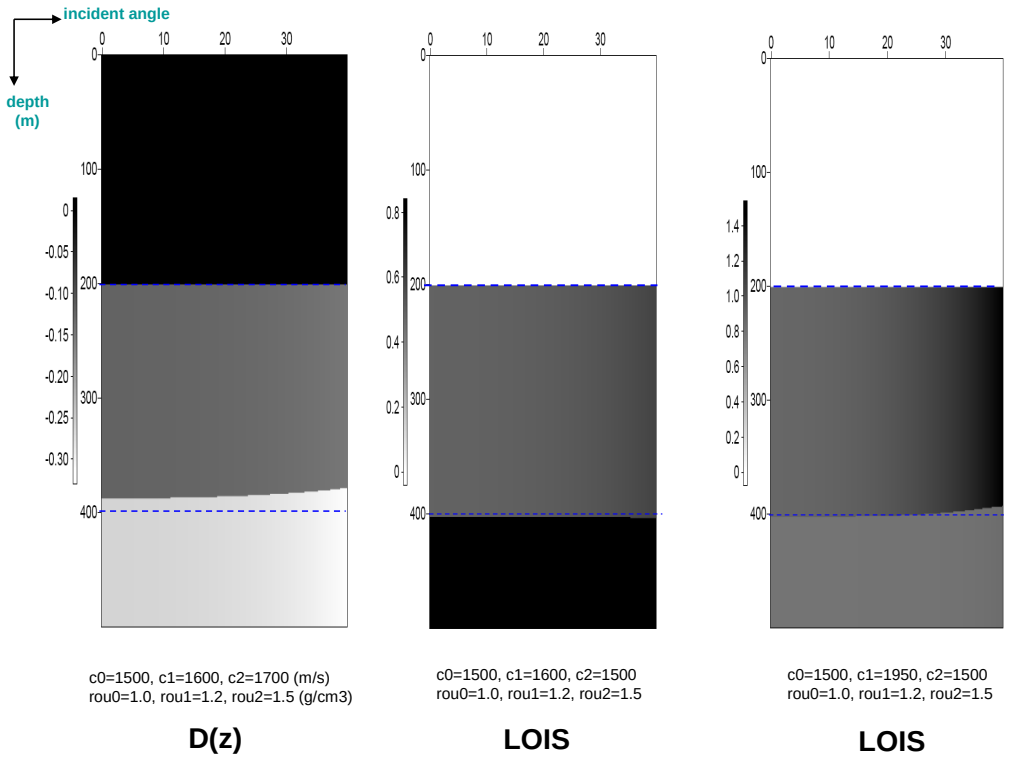

Figure 3.4: *Imaging comparison 3: left figure is a result of constant velocity (c_0=1500 m/s) migration, middle and right figures are results using two-parameter ISS LOIS imaging algorithm, where the blue dashed lines are the real depths of the two interfaces in the model. The color scale beside each graph denotes the value of reflection amplitude in each layer.*

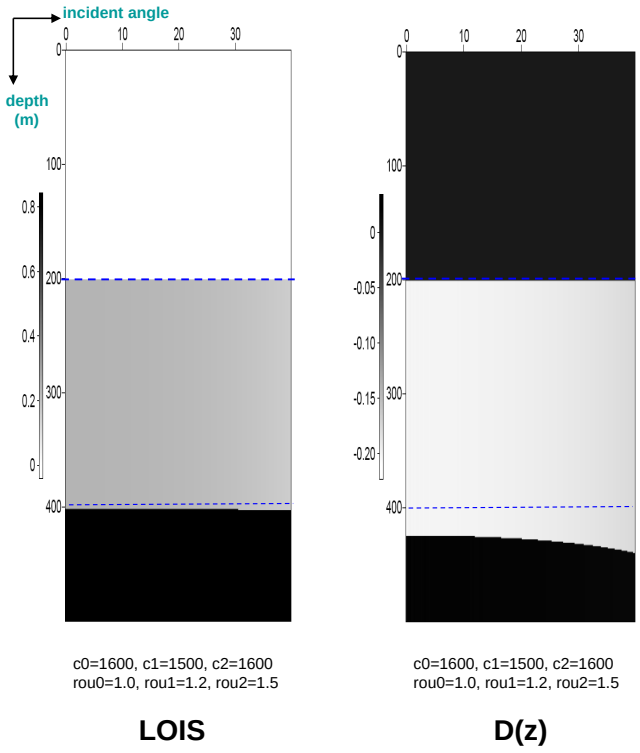

Figure 3.5: *Imaging comparison 4: right figure is a result of constant velocity (c_0=1600 m/s) migration, left figure is the result using two-parameter ISS LOIS imaging algorithm, where the blue dashed lines are the real depths of the two interfaces in the model. The color scale beside each graph denotes the value of reflection amplitude in each layer.*

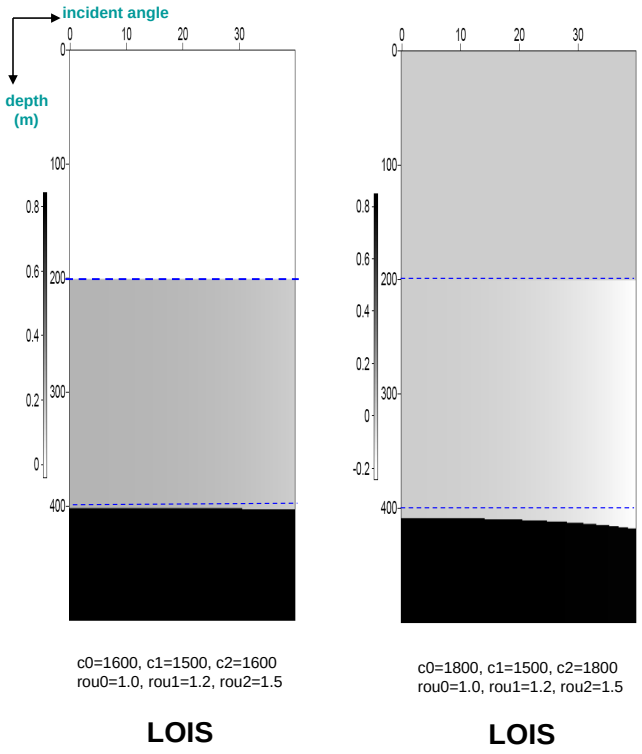

Figure 3.6: *Imaging comparison 5: both figures are results using two-parameter ISS LOIS imaging algorithm, where the blue dashed lines are the real depths of the two interfaces in the model. The color scale beside each graph denotes the value of reflection amplitude in each layer.*

point immediately. For interested reader to check this kind of linear estimation of velocity changes, the results of $\alpha_1 - \beta_1$ are also plotted in Figure 3.7.

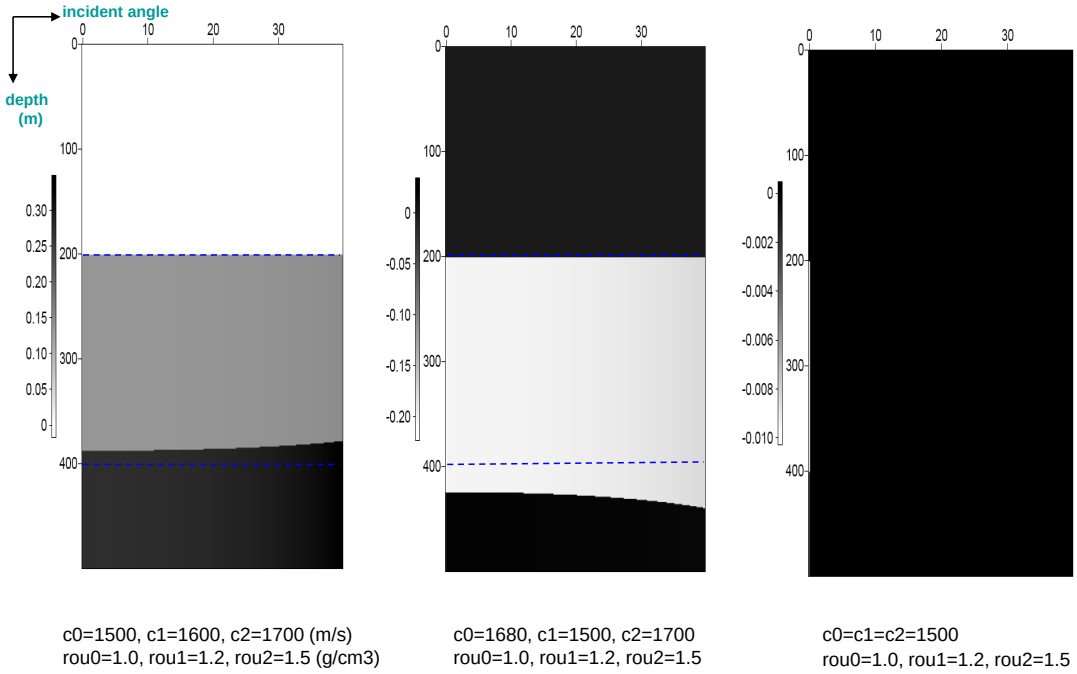

Figure 3.7: *Results of $\alpha_1(z,\theta) - \beta_1(z,\theta)$ for the three different models, where the blue dashed lines are the real depths of the two interfaces in the model. The color scale beside each graph denotes the value of reflection amplitude in each layer.*

Since the *ISS LOIS* imaging algorithm partially captures the imaging terms in the two-parameter *ISS* formalism, it is reasonalbe that it has a limited imaging capability. The extended *ISS HOIS* imaging algorithm in equation (3.10) captures more imaging terms than the *LOIS*, and it should have a better imaging capability. To demonstrate this assumption, a numerical evaluation using the *ISS HOIS* imaging

algorithm is a good starting point. Figure 3.8 and Figure 3.9 show the results of the *ISS HOIS* , *ISS LOIS* and constant velocity migration. For the smaller velocity contrast in Figure 3.8, the *ISS HOIS* algorithm located the 2^{nd} interface, much better than the other two methods. For the larger velocity contrast in Figure 3.9, the *ISS HOIS* algorithm shows a better tolerance of velocity contrast than the *ISS LOIS* and constant velocity migration method.

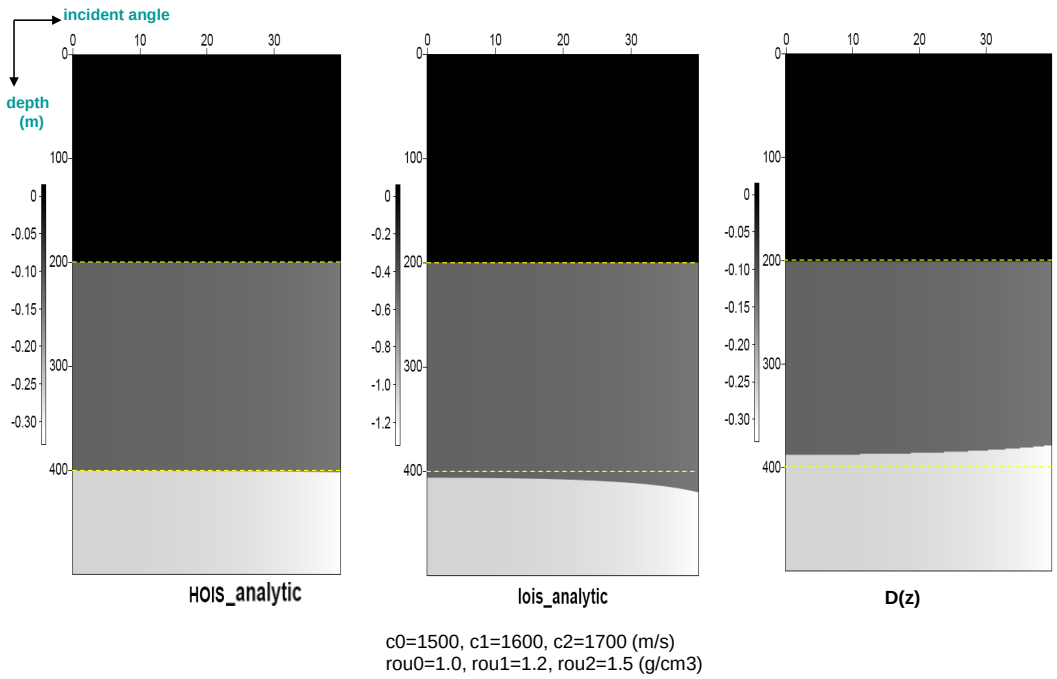

Figure 3.8: *Imaging comparison 6: right figure is a result of constant velocity (c_0=1500 m/s) migration, middle and left figures are results using two-parameter ISS LOIS and HOIS imaging algorithms, respectively, where the yellow dashed lines are the real depths of the two interfaces in the model. The color scale beside each graph denotes the value of reflection amplitude in each layer.*

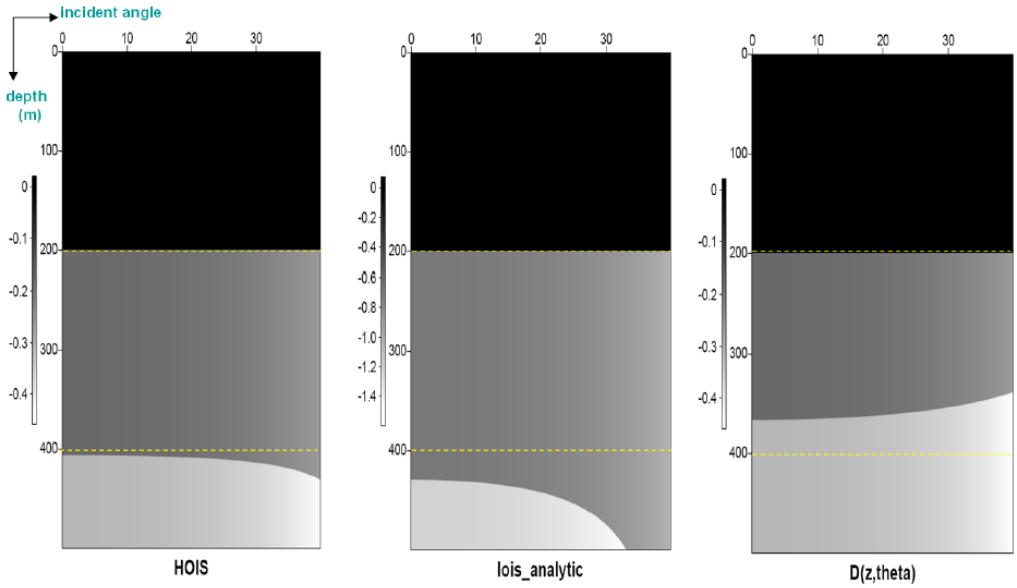

Figure 3.9: *Imaging comparison 7: right figure is a result of constant velocity (c_0=1500 m/s) migration, middle and left figures are results using two-parameter ISS LOIS and HOIS imaging algorithms, respectively, where the yellow dashed lines are the real depths of the two interfaces in the model. The color scale beside each graph denotes the value of reflection amplitude in each layer.*

To demonstrate how sensitive both *ISS LOIS* and *ISS HOIS* algorithms are to the changes in the density parameter, Figure 3.10 and Figure 3.11 show that the *ISS HOIS* imaging algorithm is much less affected by the density changes than the *ISS LOIS*, for the certain velocity model ("slower/faster/faster").

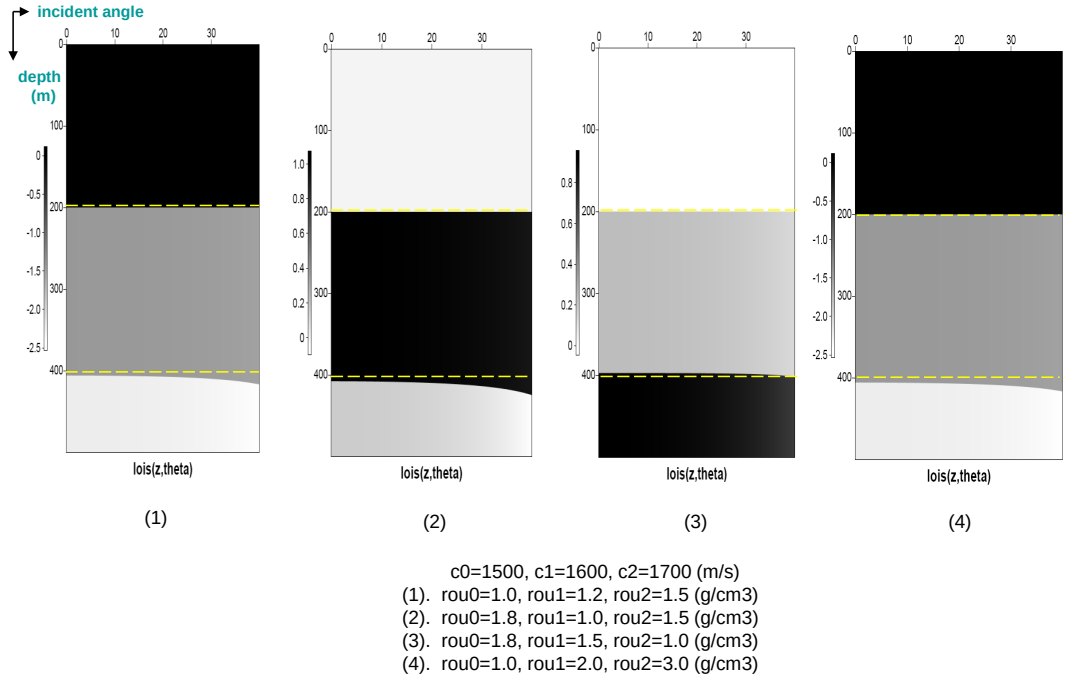

Figure 3.10: *The sensitivity of density changes to the result of the two-parameter ISS LOIS imaging algorithm: velocity model keeps same in all models. The yellow dashed lines are the real depths of the two interfaces in the model. The color scale beside each graph denotes the value of reflection amplitude in each layer.*

In the end of this section, we present a study to show how much effect the depth duration in the model will bring to the both imaging algorithms. The results are

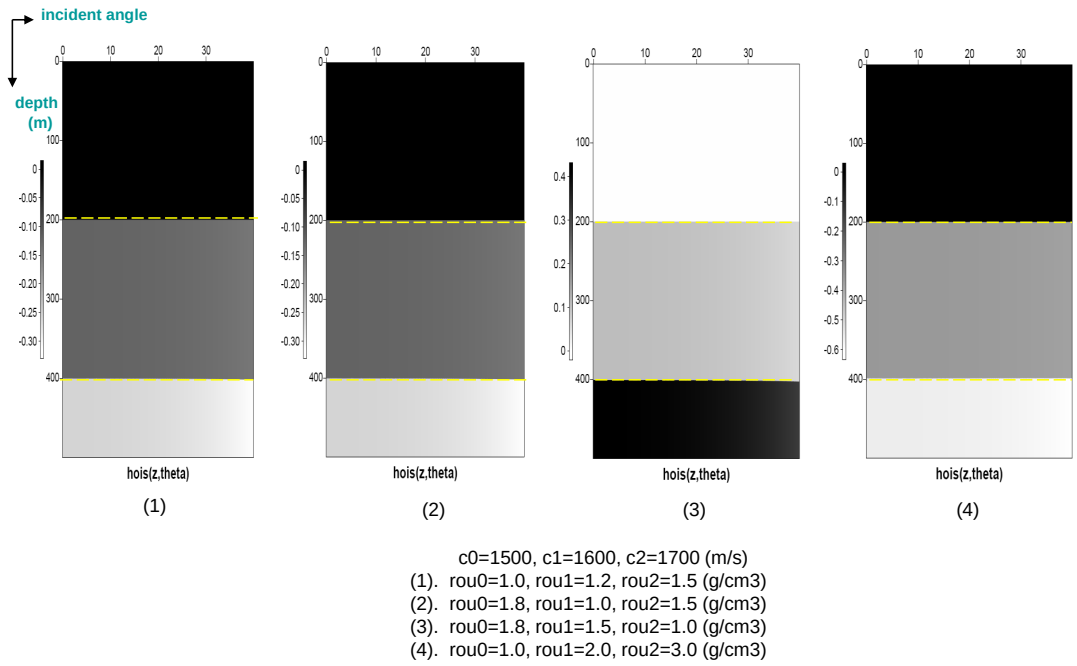

Figure 3.11: *The sensitivity of density changes to the result of the two-parameter ISS HOIS imaging algorithm: velocity model keeps same in all models. The yellow dashed lines are the real depths of the two interfaces in the model. The color scale beside each graph denotes the value of reflection amplitude in each layer.*

shown in Figure 3.12 where the 1^{st} interface depth is fixed at $a = 75$ m, but the 2^{nd} interface is varied depth from $b = 150$ m to $b = 400$ m. From the plotted results, we observe that the *ISS HOIS* imaging algorithm is more robust to the bigger depth duration than the *ISS LOIS* imaging algorithm, for the considered velocity and density configuration.

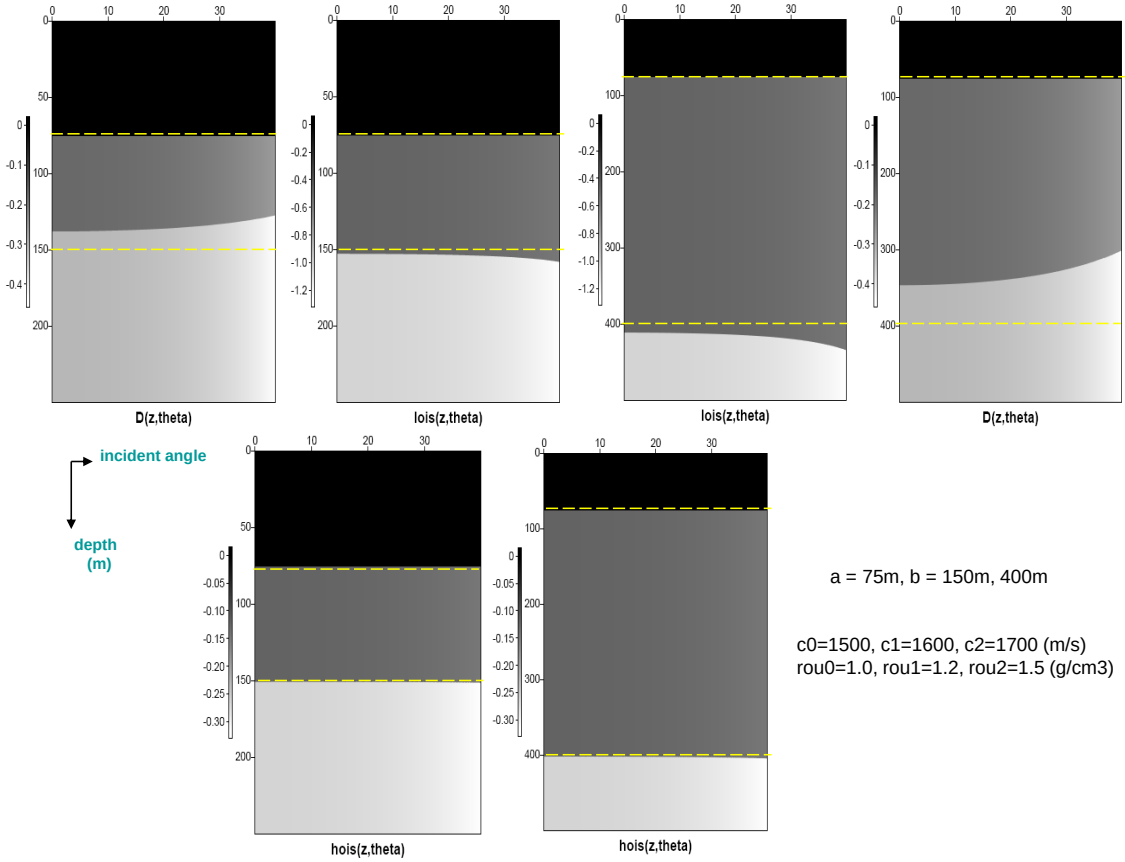

Figure 3.12: *Effect of depth duration changes to the results of constant velocity migration and the two-parameter ISS LOIS/HOIS imaging algorithms: for all models,density and velocity values are same in each layer. The yellow dashed lines are the real depths of the two interfaces. The color scale beside each graph denotes the value of reflection amplitude in each layer.*

3.5 Synthetic tests

In the previous section, I tested the imaging capability of both 1D *ISS LOIS* and *ISS HOIS* two-parameter acoustic imaging algorithms by using analytic data, which are called "perfect data" with full-band frequency. As I demonstrated mathematically, the *ISS LOIS* and *ISS HOIS* imaging algorithms perform migration without knowing any subsurface information (including actual velocity models about the layers beneath), but actually taking full advantage of reference velocity and the amplitude information imbedded in dataset. Therefore, dataset with full bandwidth, such as analytic data, definitely optimize the most potential of the tested two imaging algorithms, which also isolate the numerical issues of the algorithms from the issue of the multi-parameter imaging theory for easily examing the effectiveness of the *ISS LOIS* and *ISS HOIS* imaging algorithms.

However, the goal of the imaging algorithms developed here is to eventually implement the algorithms in the real seismic exploration world where field data, generally band-limited, is the input. Band-limited data means the amplitude of events is damaged to some extent. So how well will the two imaging algorithms developed in this chapter work for band-limited datasets? In this section, I will use a Dennis Corrigan's 1D two-parameter acoustic reflectivity code to generate two different band-limited datasets to clearly show how the *ISS LOIS* and *ISS HOIS* imaging algorithms will be influenced by the low frequency in the datasets tested, and I will compare the imaging capabilities of them between band-limited case and analytic case. For synthetic data, the zero-crossing imaging issue will also be investigated in the polarity

reversal test on the *ISS HOIS* imaging algorithm.

3.5.1 Imaging with band-limited data

The model to generate the bandlimited datasets is shown in Figure 3.13 which is a laterally invariant 4-layer acoustic medium with both velocity and density variation. The depths for the three interfaces are set, respectively, as $z_0 = 410$ m, $z_1 = 1020$ m, and $z_2 = 1520$ m. For the purpose to test the influence of dataset bandwidth on the imaging algorithms, the model is set with a moderate velocity contrast but significant density contrast, as demonstrated in the cartoon.

Two synthetic datasets are generated for the model with bandwidths of 1.0 hz $\sim$ 60 hz and 0.01 hz $\sim$ 60 hz, respectively, and with numerical sampling rates as 4 ms and 1 ms, respectively. The 1D reflectivity code generate the two datasets with both primaries and internal multiples as shown in Figure 3.14 and Figure 3.15. Both datasets are expressed in $(\tau - p)$ domain and in $(z - p)$ domain. In the $(z - p)$ domain, it is clear to tell that the waterbotoms are very well located after the constant velocity (here 1500 m/s is used.) migration, but the other two interfaces are misplaced and undermigrated, especially for large horizontal slowness values (big values of p), since the real velocities in the layer are faster than the reference velocity. Also, we notice that with different low frequency content in the two datasets, the richness of their reflectivity amplitude information is also different.

Next, I use the two synthetic datasets as the input to the *LOIS* and *HOIS* algorithms, respectively, and examine how well the two deeper interfaces are migrated.

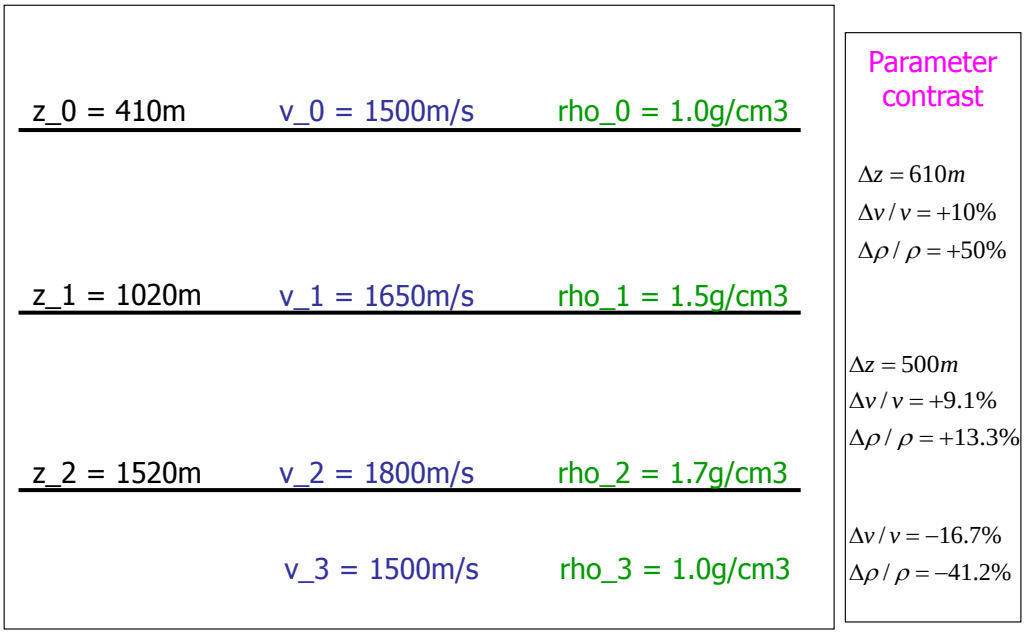

Figure 3.13: *A reflectivity model used to generate bandlimited datasets for a 1D two-parameter acoustic medium with specific parameter contrast.*

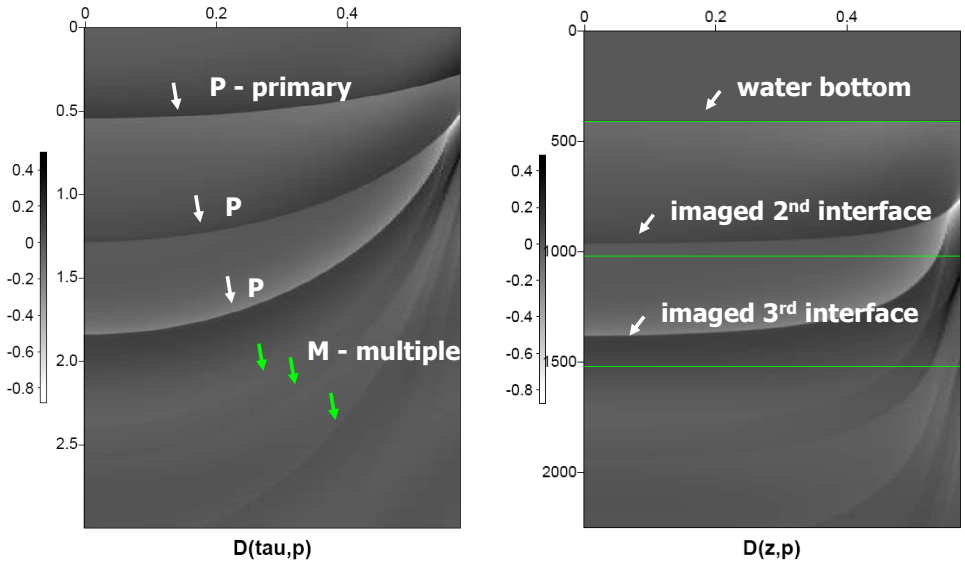

Figure 3.14: *Dataset with bandwidth of 1.0 hz $\sim$ 60 hz expressed in $(\tau - p)$ domain and in $(z - p)$ domain: the green lines in the graphs indicate the actual depths of the three interfaces in the model, and primaries and internal multiples are identified by the arrows. The color scale beside each graph denotes the value of each seismic event's (primary's or multiple's) reflection amplitude in each layer.*

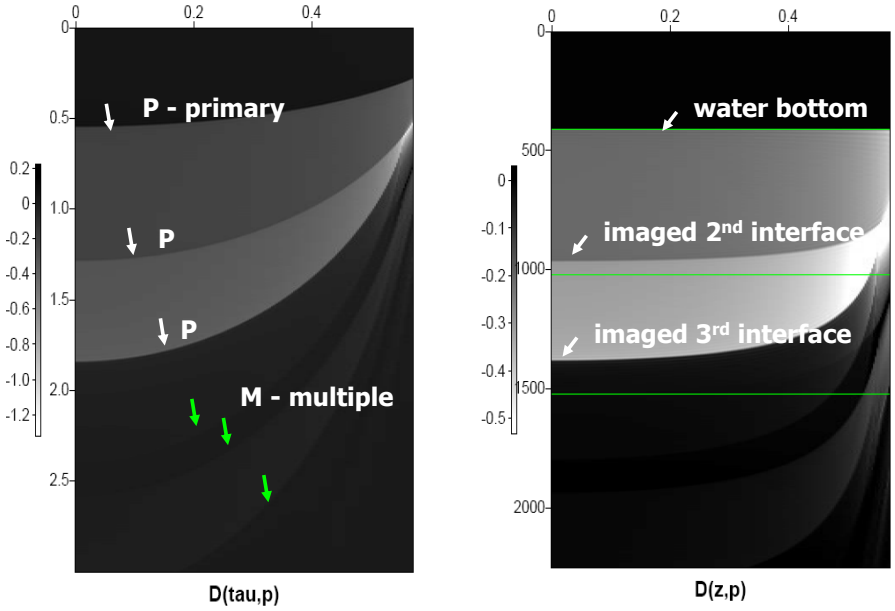

Figure 3.15: *Dataset with bandwidth of 0.01 hz $\sim$ 60 hz expressed in $(\tau - p)$ domain and in $(z - p)$ domain: the green lines in the graphs indicate the actual depths of the three interfaces in the model, and primaries and internal multiples are identified by the arrows. The color scale beside each graph denotes the value of each seismic event's (primary's or multiple's) reflection amplitude in each layer.*

The imaging results are illustrated in Figure 3.16 and Figure 3.17. In both figures, the *HOIS* imaging is better than *LOIS* imaging which is better than constant velocity migration result. We notice that the low frequency end in the bandwidth of the two datasets definitely brings impact on the imaging results. The lower frequency the dataset contains, the better the imaging result is, for both *LOIS* and *HOIS* imaging algorithms. This is a reasonable observation since the algorithms migrate the mislocated interfaces by using amplitude information in the data which is highly influenced by the low frequency content: the missing of lower frequency brings more severe damage to the amplitude of reflectivity. In addition, for great values of p (corresponding to large incident angles), the *ISS HOIS* results are not stable as indicated in the figures. This instability might be caused by the fact that the *HOIS* algorithm is more sensitive to band-limited dataset, since the input to the *HOIS* algorithm is the mathematical difference of the same dataset at different incident angles divided by the tangential difference between two incident angles, which provide the value of $\alpha_1(z,\theta) - \beta_1(z,\theta)$ as defined by the equation (3.50). But a further investigation needs to be done on this instability issue.

To further illustrate the importance of low frequency content in the input dataset to the two-parameter *LOIS* and *HOIS* algorithms, I compare the migration results of Figure 3.17 with imaging result of *HOIS* by using analytic data (see Figure 3.18). For incident angles below 30°, we notice that the *HOIS* analytic result is the best among them since the input data is full bandwidth (including zero frequency).

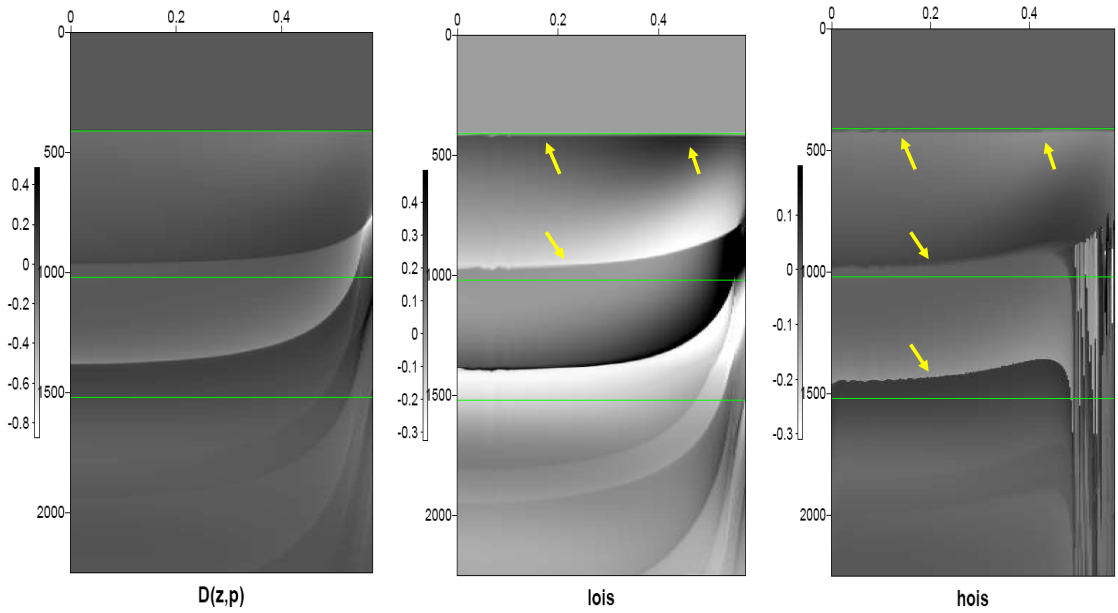

Figure 3.16: *Imaging results comparison among constant velocity migration, LOIS and HOIS for band-limited dataset of 1.0 hz ∼ 60 hz: the green lines in the graphs indicate the actual depths of the three interfaces in the model. The color scale beside each graph denotes the value of each seismic event's (primary's or multiple's) reflection amplitude in each layer.*

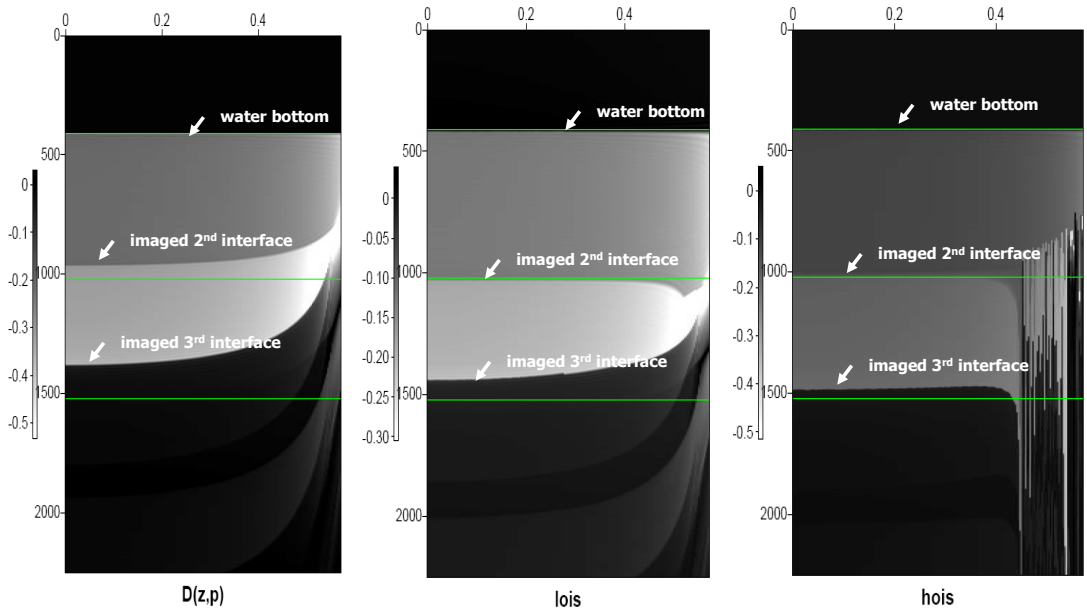

Figure 3.17: *Imaging results comparison among constant velocity migration, LOIS and HOIS for band-limited dataset of 0.01 hz ∼ 60 hz: the green lines in the graphs indicate the actual depths of the three interfaces in the model. The color scale beside each graph denotes the value of each seismic event's (primary's or multiple's) reflection amplitude in each layer.*

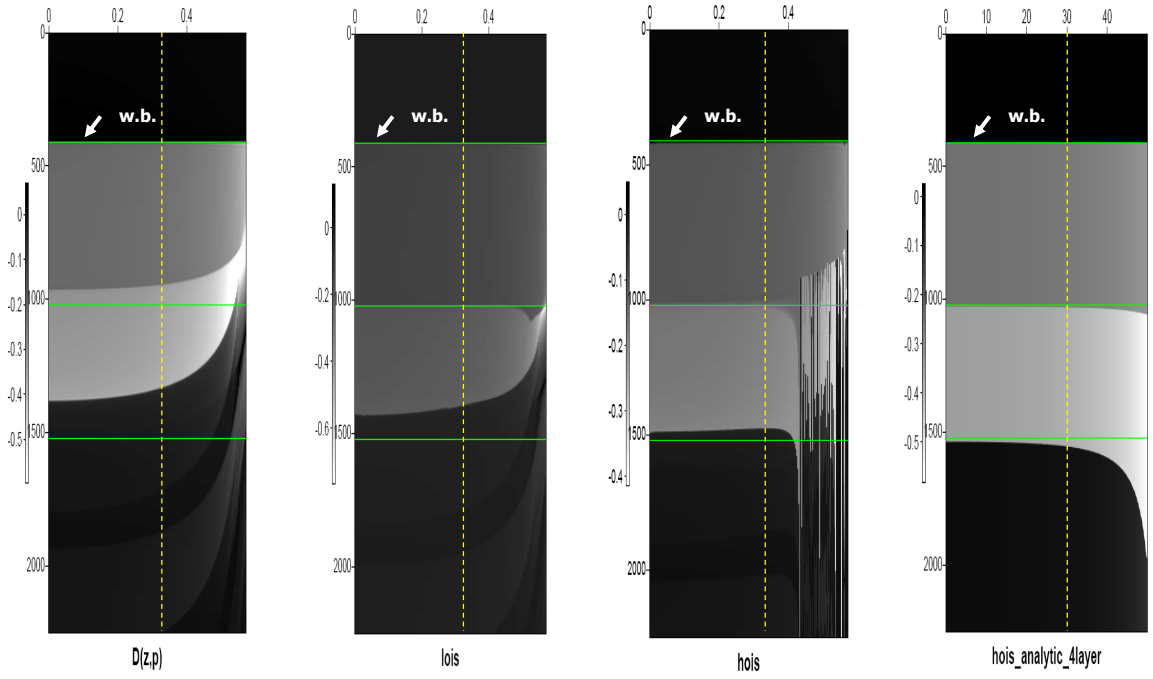

Figure 3.18: *A further imaging comparison among constant velocity migration, LOIS, HOIS for band-limited dataset of 0.01 hz $\sim$ 60 hz and HOIS by using full bandwidth data: the green lines in the graphs indicate the actual depths of the three interfaces in the model; the yellow lines show the location of horizontal slowness value with good results corresponding incicent angles below* 30°. *The color scale beside each graph denotes the value of each seismic event's (primary's or multiple's) reflection amplitude in each layer.*

3.5.2 Polarity reversal test

A polarity reversal refers to a phase transition from positive to negative values with offset (incident angles) in the reflection coefficients of the seismic reflection data, so a zero-crossing value of reflection coefficient may occur at some specific offsets. There are several important reasons to investigate polarity reversals in seismic exploration (Keys, 1989). For example, traditional AVO (Amplitude Versus Offset) analysis uses information of amplitude versus angles in seismic reflection coefficients to obtain subsurface property information (velocity and density variations, for example), and especially for identifying type I and type II AVO targets when the value of reflection coefficients has a sign change. But velocity analysis generally brings damage to the zero-crossing amplitude before flattening the AVO common imaging gather (CIG). However, the serious issue is lessened by a by-product of the multi-parameter imaging algorithms, since the *ISS LOIS/HOIS* algorithms very well preserve the zero-crossing polarity reversal information while obtaining far-offset flattened common imaging gathers.

In this section, I will first design a specific 4-layer two-parameter acoustic model (shown in Figure 3.19) to cause polarity reversals on the two deeper interfaces (as illustrated by the pink-color-dashed box area). In this model, the actual depths of three interfaces are $z_0 = 150$ m,$z_1 = 460$ m, and $z_2 = 610$ m, respectively; the actual velocity variation for the 4 layers are respectively: $v_0 = 1500$ m/s, $v_1 = 1600$ m/s, $v_2 = 1200$ m/s, and $v_3 = 1500$ m/s, with density contrast as: $\rho_0 = 1.0\ g/cm^3$, $\rho_1 = 1.1\ g/cm^3$, $\rho_2 = 2.5\ g/cm^3$, and $\rho_3 = 1.5\ g/cm^3$. The layers having polarity reversals satisfy the following conditions:

1. Increase in density but decrease in velocity with depth from layer 1 to layer 2, with acoustic impedence increasing with depth,

$$A = \rho_2/\rho_1 = 2.72 > 1; C = v_2/v_1 = 0.75 < 1; AC = I_2/I_1 = 2.04 > 1$$

2. Decrease in density but increase in velocity with depth from layer 2 to layer 3, with acoustic impedence decreasing with depth,

$$A = \rho_3/\rho_2 = 0.6 < 1; C = v_3/v_2 = 1.25 > 1; AC = I_3/I_2 = 0.75 < 1$$

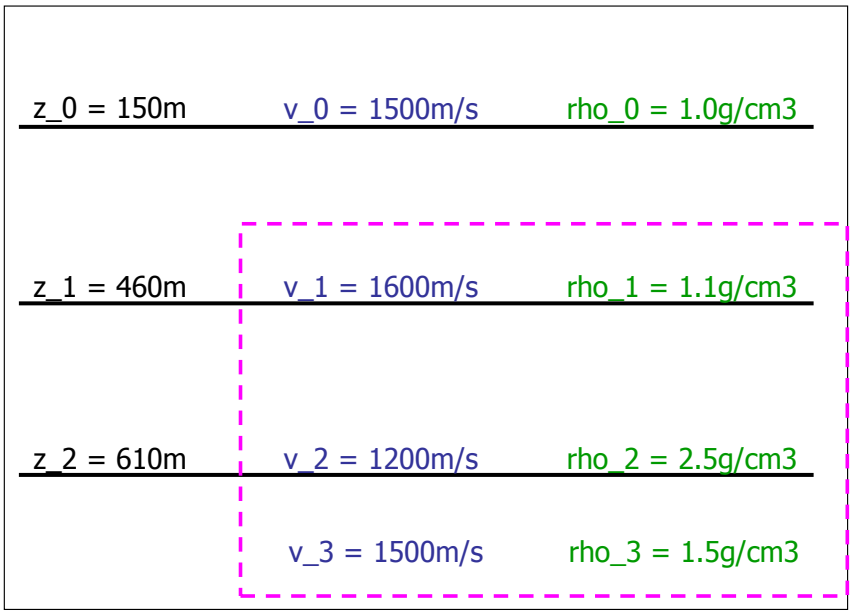

Figure 3.19: *An acoustic two-parameter 1D model specifically designed to test the polarity reversals*

Using the above model, the synthetic dataset is generated and imaged after constant velocity migration. Then this synthetic dataset is input to the acoustic two-parameter *ISS HOIS* imaging algorithm. Both imaging results are compared and shown in Figure 3.20. The imaging quality from *ISS HOIS* is improved, especially for large p values (large offsets) where *ISS HOIS* output tries to flatten the common imaging gathers (*CIG*) automatically. Recall that the *CIG* is what traditional AVO analysis needs to obtain subsurface information for identifying different types of targets. Let's now take a closer look at the zero-crossing preservation of the reflection coefficients for the two deeper reflectors in the after-migration results (see Figure 3.21). From the zoom-in graph of the ISS HOIS migration result, the two polarity reversals for the 2^{nd} and 3^{rd} interfaces occur at large incidence angles respectively at $\theta = 57.5°$ and $\theta = 56.2°$.

3.6 Conclusion and discussion

In this chapter, a much more complicated 3^{rd} order *ISS* term for a 1D two-parameter acoustic medium is calculated for the first time, which leads to an imaging pattern identified as a leading order imaging subseries (*LOIS*), and which justifies the logic of Weglein's imaging conjectures for multi-parameter media.

The derived imaging algorithm can be expressed as a shifted seismic dataset. The shifted quantity is an integral of the difference between the two first order approximations of the two parameters in the medium, which is integrated to zero when there is no velocity variation in the medium. The examination and justification

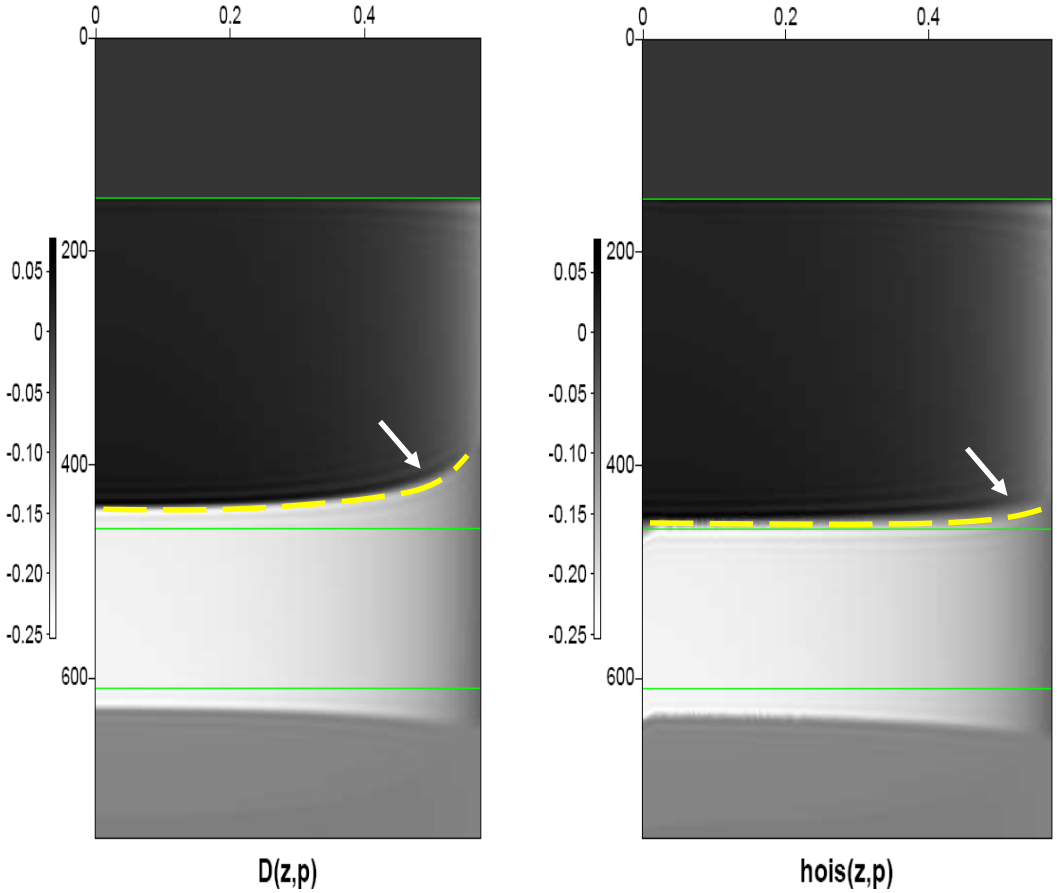

Figure 3.20: *Imaging comparison between water-speed velocity migration and ISS HOIS results over the synthetic dataset with two deeper layers of polarity reversals: green lines in the graphs indicate the actual location of all interfaces; yellow dashed lines indicate the* 2^{nd} *interfaces after two migration methods. Improved image for far-offset is denoted by the two white arrows. The color scale beside each graph denotes the value of reflection amplitude in each layer.*

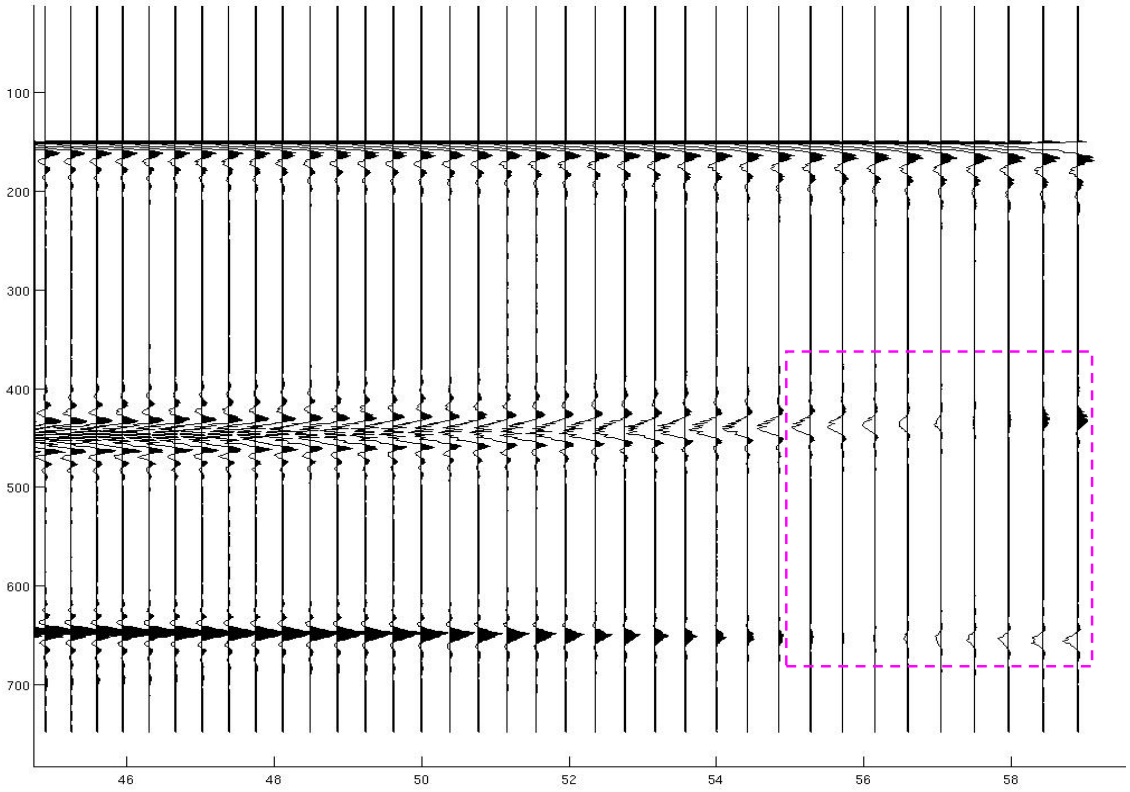

Figure 3.21: *A zoom-in ISS HOIS imaging result for the polarity reversal model: reflection coefficients' phases transit the zero value boxed in the pink dash line*

of the logic developed by Weglein in his imaging conjectures by deriving the leading order imaging algorithm in this report presents a framework to develop the ultimate *ISS* model-type independent imaging algorithm step by step. The logic steps are: For a specific model, find the "attention-needed term" which linearly relates with the measured seismic data set, then the "attention-needed term" provides the multi-parameter imaging composite which is migrated with an *ISS* reference velocity and will be shifted in the final imaging algorithm with a quantity of the "attention-provided term"–an integral of the difference among the first order approximations of the multi-parameters in that medium, which only takes care of the velocity variation of that medium.

The *LOIS* imaging algorithm derived from inverse scattering theory and its corresponding conjectured *HOIS* imaging algorithm are then tested by using both analytic data and bandlimited data for an acoustic layered models with both velocity and density variation. Numerical tests show the effectiveness and validity of both algorithms work to differently satisfying levels. Through the analytic tests, I investigated both algorithms use angle-dependent reflection amplitude information to locate subsurface interfaces without knowing an accurate velocity model but using a constant water speed reference background. Both algorithms provide better imaging results than constant velocity migration; *HOIS* is better than *LOIS* in locating deeper reflectors, and has more tolerance for depth duration and magnitude contrast in velocity and density parameters. The synthetic tests show that both imaging algorithms are sensitive to the low frequency in data spectrum, which result in a relatively poor imaging capability when compared with the performance by using

full-band analytic data. A by-product from the multi-parameter imaging algorithm is also demonstrated and discussed for polarity reversal case when amplitude of reflectivity experience a zero-crossing value with offset variation. The synthetic test shows that amplitude information are very well preserved in the imaging result of polarity reversal interfaces, where zero-crossing occur at some offset in the common imaging gathers flattened automatically at large offset by the *HOIS* imaging algorithm. This added value avoids the serious issue in traditional AVO analysis in which amplitude is damaged after velocity analysis is done to flatten common imaging gathers.

The initial numerical tests done in this chapter provide confidence of the imaging conjectures and further indications of research on the elastic multiparameter *LOIS* and *HOIS* algorithms when applied to elastic medium where multicomponent datasets will be studied for providing amplitude information to the algorithms. However, the research done in this thesis indicates that the elastic imaging multiparameter imaging could be a daunting task.

Chapter 4

Summary

In this dissertation, I used inverse scattering series (*ISS*) completing two research topics: one topic is to investigate the sensitivity of a 1D internal multiple attenuation (*IMA*) algorithm to reference velocity for land application, and the other is to develop and test the multi-parameter imaging algorithms for a 1D acoustic medium with both velocity and density variation.

As discussed in the introduction part of Chapter 1, M-OSRP has developed and delivered to the oil industry the ISS IMA algorithm with stand-alone capability of accurate prediction of all internal multiples without knowing any subsurface information but only using recorded data and a constant reference medium. For the marine case, where all sources and receivers are located in the water column, the selection of a pure water background as the reference medium for the ISS IMA algorithm is reasonable and restricts the perturbation to below the measurement surface (as required by the mathematical derivation of the algorithm). However, due to the heterogeneous

and complicated property of the near surface on land, it is not possible to choose a simple constant elastic reference medium (the reference Green's function can not be easily expressed analytically in a complicated reference medium). To prove the validity of the ISS IMA when provided with a wrong reference background, I presented in Chapter 2 an analytical calculation of the 1D ISS IMA for a layered earth under normal and non-normal incidence. The data used are multi-component PP, PS, SP and SS geophone data. The computation result showed that the reference P and S velocities used to migrate the original data as an input to the algorithm, are cancelled out in the predicted exponential function, which provides the prediction of vertical arrival time of all internal multiples. The spatial "lower-higher-lower" relationship remains valid even when using a wrong reference velocity, since the pseudo-depths are just a rescaled time series in the data, and the algorithm will automatically use this spatial restriction relationship when combining three subevents in the data to reconstruct the predicted internal multiples. As long as the spatial relationship does not change, the prediction from a convolution of subevents is always correct. (Spurious events are exceptional examples due to a false combination of leading order internal multiples as subevents, as discussed in the introduction of Chapter 1.) Therefore, the 1D ISS IMA is insensitive to V_p and V_s reference velocities for land application.

In Chapter 2, I also presented numerical tests of the 1D ISS IMA algorithm on different types of media: isotropic acoustic, isotropic acoustic over elastic, anisotropic (VTI), and elastic media, respectively. The purpose of testing these models is to demonstrate the value of the IMA for land application. The prediction results from all these numerical tests demonstrated this validity.

In Chapter 3, I first described the logic behind Weglein's imaging conjecture for a 1D two-parameter (velocity and density change) acoustic medium. The one-parameter (velocity only change) leading order (*LOIS*) and higher order (*HOIS*) imaging algorithms can fail due to the model type dependence of deriving the algorithms. When two parameters (with both velocity and density varied) are considered, the wave equation and the mathematical derivation of ISS imaging algorithm are different from those in velocity only case. The computation of the second order ISS term in a two-parameter acoustic medium leads to a separation of pure inversion part and imaging-only part, as discussed in the introduction of this dissertation. The rewritten form of the imaging-only α_2, β_2 terms, when combined with the first order result (Zhang and Weglein, 2003), suggests a direct similarity between velocity only case and the two-parameter case. The two parameters, α and β, are not separately imaged but are imaged as a composite which is linear to a rescaled input water-speed-migrated dataset, the "attention-needed term. The imaging conjecture shows the shifted quantity as the integral which survives when there is velocity change in the two-parameter case. For constant velocity but variable density, the water-speed-migration of the data has already correctly positioned subsurface interfaces, and hence the imaging algorithm automatically shuts down the shifted quantity. This purposeful perturbation is well indicated in the conjectured algorithm.

Then in this chapter I showed an analytical calculation of the third order ISS term for the two-parameter case. The computation result identified a higher order imaging-only term which has a counterpart in the one-parameter case with velocity only change when shutting down density variation in the two-parameter acoustic medium.

Therefore, following the same logic of identifying the LOIS imaging algorithm in the velocity only variation case, a two-parameter LOIS was separated from the whole series. The subseries is a Taylor series which can be written in a closed form, which allowed us to recognize it as the imaging conjecture.

The numerical evaluation of the two-parameter LOIS algorithm was then performed for analytical data to fully test its imaging strength. The shifted quantity with the difference between α_1 and β_1 can be calculated by using the data at two separate incident angles. Tests showed that numerical tricks are needed to keep the two angles as close as possible so that the output result is numerically stable. Since ISS imaging algorithms assume no subsurface velocity models but uses amplitude information in the data, how well preserved the amplitude information, so the low frequency content in data, does have direct impact on the imaging output configuration. For band-limited data with muted low frequency, the LOIS has suffered from amplitude damage which weakens the algorithm's imaging accuracy. Current imaging algorithms are model-type dependent, so imaging algorithms have to collect enough frequency bandwidth to move each "box-like" event in the input data to its correct position. This shifting is inefficient and requires low frequency content in the input data. The data regularization method developed in M-OSRP has highly compensated the missing part of low frequency and proved to be effective for addressing the issue in multi-parameter imaging (Liu et al., 2010; Liu and Weglein, 2011). Future development on low frequency acquisition technology can also provide field data better suited for ISS multi-parameter imaging algorithms. The future M-OSRP imaging algorithms will be seeking a model-type independent mode which

moves “spikes” in the input dataset instead of “boxes”. In such a case, the imaging algorithm will be working on single frequency at a time just like the ISS free surface multiple algorithm.

To make a comparison, the two-parameter HOIS algorithm was also tested in Chapter 3 by using both analytical and synthetic data. Both cases demonstrated that the HOIS algorithm has better imaging capability and higher tolerance for contrast and error duration in parameters than LOIS. Both algorithms are automatically reduced to a constant water speed migration when there is no velocity change but only density variation in the 1D acoustic medium.

In conclusion, the ISS IMA insensitivity to reference velocity verified in this dissertation provided sufficient confidence for geoscientists to apply the algorithm on land, regardless of the complexity of near surface. The ISS two-parameter LOIS and HOIS imaging algorithms derived in this dissertation were proven valid and the research presented here moves the one parameter (velocity only) case a step further toward real earth application.

References

Araújo, F. V. *Linear and non-linear methods derived from scattering theory: backscattered tomography and internal multiple attenuation.* PhD dissertation, Universidade Federal da Bahia, 1994.

Carvalho, P. M. *Free-surface multiple reflection elimination method based on nonlinear inversion of seismic data.* PhD dissertation, Universidade Federal da Bahia, 1992.

Claerbout, J. F. "Toward a unified theory of reflector mapping." *Geophysics* 36 (1971): 467–481.

Coates, R. T. and A. B. Weglein. "Internal multiple attenuation using inverse scattering: Results from prestack 1 and 2D acoustic and elastic synthetics." *66th Annual International Meeting, Society of Exploration Geophysicist, Expanded Abstracts* (1996): 1522–1525.

French, William S. "Two-dimensional and three-dimensional migration of model-experiment reflection profiles." *Geophysics* 39 (1974): 265–277.

Glogovsky, V., E. Landa, and J. Paffenholz. "Integrated approach to subsalt depth imaging: Synthetic case study.." *The Leading Edge* 21 (2002): 1217–1226.

Gray, S. H., J. Etgen, J. Dellinger, and D. Whitmore. "Seismic migration problems and solutions." *Geophysics* 66 (2001): 1622–1640.

Hagedoorn, J. G. "A process of seismic reflection interpretation." *Geophysical Prospecting* 2 (1954): 85–127.

Herrera, W., C. Ma, H. Liang, and A. B. Weglein. "Isolation of an elimination subseries for the surgical removal of first-order internal multiples with downward reflection at the shallowest reflector." *Mission-Oriented Seismic Research Program (M-OSRP) Annual Report*. 2012.

Herron, D. "Pitfalls in seismic interpretation: Depth migration artifacts." *The Leading Edge* 19 (2000): 1016–1017.

Hsu, S. and A. B. Weglein. "Onshore project report I: Reference velocity sensitivity for the marine internal multiple attenuation algorithm: analytic examples." *Mission-Oriented Seismic Research Program (M-OSRP) Annual Report*. 2008.

Hsu, S.-Y., S. Jiang, and A. B. Weglein. "An analytic example examining the reference velocity sensitivity of the elastic internal multiple attenuation algorithm." *Mission-Oriented Seismic Research Program (M-OSRP) Annual Report*. 2009.

Innanen, K. A. and A. B. Weglein. "Simultaneous Imaging and Inversion with the Inverse Scattering Series." *Proceedings of the Eighth International Congress of the SBGf and Fifth Latin American Geophysical Conference*. . SBGf, 2003.

Jiang, S. and A. B. Weglein. "Deriving an imaging algorithm for a laterally invariant multiparameter acoustic medium from the inverse scattering series." *Mission-Oriented Seismic Research Program (M-OSRP) Annual Report*. 2008.

Jiang, S., A. B. Weglein, and S. A. Shaw. "Progressing multiparameter imaging using the inverse scattering series: An initial analytic test of the leading order imaging subseries (LOIS) closed form and its extended higher order imaging subseries (HOIS) closed form for a laterally invariant two-parameter acoustic medium." *Mission-Oriented Seismic Research Program (M-OSRP) Annual Report*. 2009.

Jost, Res and Walter Kohn. "Construction of a potential from a phase shift." *Phys. Rev.* (1952): 977–992.

Keys, R. G. "Polarity reversals in reflections from layered media." *Geophysics* 54 (1989): 900–905.

Li, X. *I. Multi-component direct nonlinear inversion for elastic earth properties using the inverse scattering series; II. Multi-parameter depth imaging using the inverse scattering series*. PhD dissertation, University of Houston, 2011.

Liang, H. and A. B. Weglein. "Source wavelet effects on the inverse scattering series internal-multiple leading-order-attenuation algorithm and its higher-order modification that accommodate issues that arise when treating internal multiples as subevents." *Mission-Oriented Seismic Research Program (M-OSRP) Annual Report*. 2012.

Liu, F., X. Li, and A.B. Weglein. "Addressing innate data limitations in ISS imaging algorithms." *Mission-Oriented Seismic Research Program (M-OSRP) Annual Report*. 2010.

Liu, F., B. G. Nita, A. B. Weglein, and K. A. Innanen. "Inverse Scattering Series in the presence of lateral variations." *Mission-Oriented Seismic Research Program (M-OSRP) Annual Report*. 2004.

Liu, F. and A.B. Weglein. "Part I: Addressing issues of band-limited data in multi-parameter ISS imaging; Part II: Advances in finite-difference modeling." *Mission-Oriented Seismic Research Program (M-OSRP) Annual Report*. 2011.

Liu, F., A.B. Weglein, K.A. Innanen, and B.G Nita. "Extension of the non-linear depth imaging capability of the inverse scattering series to multidimensional media: strategies and numerical results." 2005.

Liu, Fang. *Multi-Dimensional Depth Imaing without an Adequate Velocity model*. PhD dissertation, University of Houston, 2006.

Ma, C. and A. B. Weglein. "Inverse Scattering Series (ISS) leading-order internal-multiple-attenuation algorithm and higher-order modification to accommodate primaries and internal multiples as input: 1-D normal incident test on interfering events, and extension to multi-D." *Mission-Oriented Seismic Research Program (M-OSRP) Annual Report*. 2014.

Matson, K. H. "The relationship between scattering theory and the primaries and multiples of reflection seismic data." *Journal of Seismic Exploration* 5 (1996): 63–78.

Matson, K. H. *An inverse-scattering series method for attenuating elastic multiples from multicomponent land and ocean bottom seismic data*. PhD dissertation, University of British Columbia, 1997.

Morse, P. M. and H. Feshbach. *Methods of theoretical physics*. McGraw-Hill Book Co., 1953.

Nita, Bogdan G. and Arthur B. Weglein. Inverse scattering internal multiple attenuation algorithm in complex multi-d media. Technical report, Mission-Oriented Seismic Research Project, University of Houston, 2005.

Prosser, Reese T. "Formal solutions of inverse scattering problems." *Journal of Mathematical Physics* 10 (1969): 1819–1822.

Prosser, Reese T. "Formal solutions of inverse scattering problems II." *Journal of Mathematical Physics* 17 (1976): 1775–1779.

Prosser, Reese T. "Formal solutions of inverse scattering problems III." *Journal of Mathematical Physics* 21 (1980): 2648–2653.

Prosser, Reese T. "Formal solutions of inverse scattering problems IV. Error estimates." *Journal of Mathematical Physics* 23 (1982): 2127–2130.

Ramírez, A. C. and A.B. Weglein. "An inverse scattering internal multiple elimination method: Beyond attenuation, a new algorithm and initial tests." *SEG Expanded Abstracts.* (2005): 2115–2118.

Razavy, M. "Determination of the wave velocity in an inhomogeneous medium from reflection data." *Journal of the Acoustical Society of America* 58 (1975): 956–963.

Schneider, W. A. "Integral formulation for migration in two-dimensions and three-dimensions." *Geophysics* 43 (1978): 49–76.

Shaw, S. A. *An inverse scattering series algorithm for depth imaging of reflection data from a layered acoustic medium with an unknown velocity model*. PhD dissertation, University of Houston, 2005.

Shaw, S. A. and A. B. Weglein. "Imaging seismic reflection data at the correct depth without specifying an accurate velocity model: Initial examples of an inverse scattering subseries." *Frontiers of remote sensing information processing*. Ed. C. H. Chen. World Scientific Publishing Company, 2003. chapter 21, 469–484.

Shaw, S. A. and A. B. Weglein. "A leading order imaging series for prestack data acquired over a laterally invariant acoustic medium. Part II: Analysis for data missing low frequencies." *Mission-Oriented Seismic Research Program (M-OSRP) Annual Report*. 2004.

Shaw, S. A., A. B. Weglein, D. J. Foster, K. H. Matson, and R. G. Keys. "Convergence properties of a leading order depth imaging series." *73rd Annual International Meeting, Society of Exploration Geophysicist, Expanded Abstracts* (2003): 937–940.

Shaw, Simon A., A. B. Weglein, K. H. Matson, and D. J. Foster. "Cooperation of the leading order terms in an inverse-scattering subseries for imaging: 1-D analysis and evaluation.." *SEG Technical Program Expanded Abstracts* (2002): 2277–2280.

Stolt, R. H. "Migration by Fourier transform." *Geophysics* 43 (1978): 23–48.

Stolt, R. H. and A. B. Weglein. "Migration and inversion of seismic data." *Geophysics* 50 (1985): 2458–2472.

Taylor, J. R. *Scattering theory: the quantum theory of nonrelativistic collisions*. John Wiley & Sons, Inc., 1972.

Wang, Z. *Progress of ISS depth imaging without velocity for more complex cases*. PhD dissertation, University of Houston, 2011.

Weglein, A. B. "The inverse scattering concept and its seismic application." *Developments in geophysical exploration methods*. Ed. A.A. Fitch. Volume 6 . Elsevier Applied Science, (1985). 111–138.

Weglein, A. B., F. V. Araújo, P. M. Carvalho, R. H. Stolt, K. H. Matson, R. T. Coates, D. Corrigan, D. J. Foster, S. A. Shaw, and H. Zhang. "Inverse scattering series and seismic exploration." *Inverse Problems* (2003): R27–R83.

Weglein, A. B., W. E. Boyce, and J. E. Anderson. "Obtaining three-dimensional velocity information directly from reflection seismic data: An inverse scattering formalism." *Geophysics* 46 (1981): 1116–1120.

Weglein, A. B., D. J. Foster, K. H. Matson, S. A. Shaw, P. M. Carvalho, and D. Corrigan. "Predicting the correct spatial location of reflectors without knowing or determining the precise medium and wave velocity: initial concept, algorithm and analytic and numerical example." *Journal of Seismic Exploration* 10 (2002): 367–382.

Weglein, A. B., F. A. Gasparotto, P. M. Carvalho, and R. H. Stolt. "An inverse-scattering series method for attenuating multiples in seismic reflection data." *Geophysics* 62 (1997): 1975–1989.

Weglein, A. B., F. Liu, X. Li, P. Terenghi, E. Kragh, J. D. Mayhan, Z. Wang, J. Mispel, L. Amundsen, H. Liang, L. Tang, and S.-Y. Hsu. "Inverse scattering series direct depth imaging without the velocity model: first field data examples." *Mission-Oriented Seismic Research Program (M-OSRP) Annual Report.* 2011.

Weglein, A. B. and K. H. Matson. "Inverse scattering internal multiple attenuation: An analytic example and subevent interpretation." *SPIE Conference on Mathematical Methods in Geophysical Imaging* (1998): 108–117.

Weglein, A. B., K. H. Matson, D. J. Foster, P. M. Carvalho, D. Corrigan, and S. A. Shaw. "Imaging and inversion at depth without a velocity model: Theory, concepts and initial evaluation." *70th Annual International Meeting, Society of Exploration Geophysicist, Expanded Abstracts* (2000): 1016–1019.

Weglein, A.B. and W.H. Dragoset. *Multiple Attenuation.* Geophysics reprint series. Society of Exploration Geophysicist, (2005).

Zhang, H. and A. B. Weglein. "Target identification using the inverse scattering series: inversion of large-contrast, variable velocity and density acoustic media." *Mission-Oriented Seismic Research Program (M-OSRP) Annual Report.* 2003.

Zhang, H. and A. B. Weglein. "Target identification using the inverse scattering series: data requirements for the direct inversion of large-contrast, inhomogeneous

elastic media." *Mission-Oriented Seismic Research Program (M-OSRP) Annual Report*. 2004.

Zhang, H. and A. B. Weglein. "The inverse scattering series for tasks associated with primaries: depth imaging and direct non-linear inversion of 1D variable velocity and density acoustic media." *SEG Technical Program Expanded Abstracts*. (2005), 1705–1708.

Zhang, H. and A. B. Weglein. "Direct non-linear inversion of multi-parameter 1D elastic media using the inverse scattering series." *Mission-Oriented Seismic Research Program (M-OSRP) Annual Report*. (2006), 284–311.

Zhang, J., F. Liu, K. A. Innanen, and A. B. Weglein. "Comprehending and analyzing the leading order and higher order imaging closed forms derived from inverse scattering series." *SEG Technical Program Expanded Abstracts*. 2007.

Zou, Y. and A. B. Weglein. "The internal-multiple elimination algorithm for all reflectors for 1D earth. Part 1: strengths and limitations.." *Journal of Seismic Exploration* 23 (2014): 393–404.

APPENDIX

Appendix A

Mathematical derivation of α_3 and β_3 of the 3^{rd} term in the *ISS* for a 1D two-parameter acoustic medium case

I start the derivation by inserting 2D Green's bilinear form of equation (3.21) into the 3^{rd} term in the *ISS*, equation (3.15), when the medium is a 1D acoustics with both p-bulk modulus and density variations, where $\hat{V}_3$ is expressed as,

$$\hat{V}_3(x', z') = \frac{\omega^2}{K_0}\alpha_3(z') + \frac{1}{\rho_0}\beta_3(z')\frac{\partial^2}{\partial x'^2} + \frac{1}{\rho_0}\frac{\partial}{\partial z'}\beta_3(z')\frac{\partial}{\partial z'}. \tag{A.1}$$

After the partial derivative operator on the exponential function in Green's function, the left hand side of the 3^{rd} term in the *ISS* is expressed as,

$$\begin{aligned} L.H.S = &- \frac{{\rho_0}^2}{(2\pi)^4} \int \cdots \int_{-\infty}^{\infty} dx' dz' d{k_x}' d{k_z}' d{k_x}'' d{k_z}'' \frac{e^{i{k_x}'(x_g - x')} e^{i{k_z}'(z_g - z')}}{k^2 - ({k_x}'^2 + {k_z}'^2)} \\ &\cdot \left\{ \frac{\omega^2}{K_0} \alpha_3(z') + \frac{1}{\rho_0} \beta_3(z') \cdot (i{k_x}'')^2 + \frac{1}{\rho_0} \left[\beta_3'(z') \cdot (i{k_z}'') + \beta_3(z') \cdot (i{k_z}'')^2 \right] \right\} \\ &\cdot \frac{e^{i{k_x}''(x' - x_s)} e^{i{k_z}''(z' - z_s)}}{k^2 - ({k_x}''^2 + {k_z}''^2)}. \end{aligned} \tag{A.2}$$

where $\beta_3'(z')$ means a derivative over z'. Performing a Fourier transform over the x-axes of both sources and geophones on the above expression,

$$\frac{1}{(2\pi)^2} \iint_{-\infty}^{\infty} dx_g dx_s e^{-ik_g x_g} e^{-ik_s x_s} \circledast L.H.S$$

and notice the following math identity relations,

$$\frac{1}{2\pi} \int_{-\infty}^{\infty} e^{i({k_x}' - k_g)x_g} dx_g = \delta({k_x}' - k_g) \tag{A.3}$$

$$\frac{1}{2\pi} \int_{-\infty}^{\infty} e^{i(k_s - {k_x}'')x_s} dx_s = \delta({k_x}' - k_g). \tag{A.4}$$

Hence, after integration over ${k_x}'$, ${k_x}''$ and x' which leads to $k_g = k_s = {k_x}' = {k_x}''$ and $q_g = q_s$, the *L.H.S* can be written as,

$$\begin{aligned} L.H.S = &- \frac{{\rho_0}^2}{(2\pi)^4} \cdot \int \cdots \int_{-\infty}^{\infty} dz' d{k_z}' d{k_z}'' \frac{e^{i{k_z}'(z_g - z')}}{k^2 - ({k_g}^2 + {k_z}'^2)} \frac{e^{i{k_z}''(z' - z_s)}}{k^2 - ({k_g}^2 + {k_z}''^2)} \\ &\cdot \left\{ \frac{k^2}{\rho_0} \alpha_3(z') + \frac{1}{\rho_0} \beta_3(z') \cdot (ik_g)^2 + \frac{1}{\rho_0} \left[\beta_3'(z') \cdot (i{k_z}'') + \beta_3(z') \cdot (i{k_z}'')^2 \right] \right\}. \end{aligned} \tag{A.5}$$

Notice the wave numbers relation $k^2 - k_g^2 = q_g^2$, and use knowlege of contour integral and residue theorem on the following integrals,

$$\int_{-\infty}^{\infty} d{k_z}' \frac{e^{i{k_z}'(z_g - z')}}{q_g^2 - {k_z}'^2} = \frac{\pi}{iq_g} e^{iq_g|z_g - z'|} \tag{A.6}$$

$$\int_{-\infty}^{\infty} dk_z{}'' \left[\frac{\beta_3'(z')}{\rho_0} \cdot (ik_z'')\right] \frac{e^{ik_z''(z'-z_s)}}{q_g^2 - k_z{}''^2} = \frac{\beta_3'(z')}{\rho_0} \left[(iq_g) \cdot \frac{\pi}{iq_g} e^{iq_g(z'-z_s)} H(z'-z_s) - (iq_g) \cdot \frac{\pi}{iq_g} e^{-iq_g(z'-z_s)} H(z_s - z')\right] \tag{A.7}$$

$$\int_{-\infty}^{\infty} dk_z{}'' \left[\frac{\beta_3(z')}{\rho_0} \cdot (ik_z'')^2\right] \frac{e^{ik_z''(z'-z_s)}}{q_g^2 - k_z{}''^2} = \frac{\beta_3(z')}{\rho_0} \left[(iq_g)^2 \cdot \frac{\pi}{iq_g} e^{iq_g(z'-z_s)} H(z'-z_s) + (-iq_g)^2 \cdot \frac{\pi}{iq_g} e^{-iq_g(z'-z_s)} H(z_s - z')\right] \tag{A.8}$$

and considering $z' > z_g(z_s)$, the $L.H.S$ is,

$$L.H.S = -\frac{{\rho_0}^2}{(2\pi)^3} \cdot \left\{ \int_{-\infty}^{\infty} dz' \left(\frac{\pi}{iq_g}\right)^2 \left[\frac{k^2}{\rho_0} (\alpha_3(z') - \beta_3(z')) + \frac{iq_g}{\rho_0} \beta_3'(z')\right] e^{-iq_g(z_g+z_s)} e^{2iq_g z'} \right\}. \tag{A.9}$$

Therefore, after a Fourier transform, the above equation can be expressed in the wavenumber domain in a simple concise form as,

$$-G_0 V_3 G_0 = \frac{\rho_0}{4} \left[\frac{1}{cos^2\theta} \tilde{\alpha_3}(2q_g) + (1 - tan^2\theta) \tilde{\beta_3}(2q_g)\right] e^{-iq_g(z_g+z_s)} \tag{A.10}$$

where $\tilde{\alpha_3}(2q_g)$ and $\tilde{\beta_3}(2q_g)$ are two Fourier conjugates of the two variables. In the final expression, the above result will still be transformed over the variable $2q_g$ back into the pseudo-depth z domain, and expressed as:

$$-G_0 V_3 G_0 = \frac{\rho_0}{4} \left[\frac{1}{cos^2\theta} \alpha_3(z) + (1 - tan^2\theta) \beta_3(z)\right] \tag{A.11}$$

Note that the term $e^{-iq_g(z_g+z_s)}$ has been omitted since it will occur in each term of the afterwards calculation and will be cancelled out before doing a Fourier transform over $2q_g$.

Next, let's calculate the $R.H.S$ of the equation (3.15), starting with the following term: $G_0V_1G_0V_2G_0$. As the previous calculation, plug into the bilinear form of Green's function and the expressions of the two differential operators V_1 and V_2 in the similar form as equation (A.1) but with corresponding subscripts "1" and "2", and act on the functions behind them. Also, I will perform an Fourier transform over both sources x_s and geophones x_g, and integrate over the variables of ${k_x}'$ and ${k_x}'''$. Then this term will be written as:

$$
\begin{aligned}
G_0V_1G_0V_2G_0 = {} & \frac{{\rho_0}^3}{(2\pi)^6}\int\cdots\int_{-\infty}^{\infty} dx'dz'dx''dz''d{k_z}'d{k_x}''d{k_z}''d{k_z}''' \frac{e^{-ik_gx'}e^{ik_z'(z_g-z')}}{q_g^2-{k_z}'^2} \\
& \cdot\left\{\frac{\omega^2}{K_0}\alpha_1(z')+\frac{(ik_x'')^2}{\rho_0}\beta_1(z')+\frac{1}{\rho_0}\left[\beta_1'(z')\cdot(ik_z'')+\beta_1(z')\cdot(ik_z'')^2\right]\right\}\frac{e^{ik_x''(x'-x'')}e^{ik_z''(z'-z'')}}{k^2-({k_x}''^2+{k_z}''^2)} \\
& \cdot\left\{\frac{\omega^2}{K_0}\alpha_2(z'')+\frac{(ik_s)^2}{\rho_0}\beta_2(z'')+\frac{1}{\rho_0}\left[\beta_2'(z'')\cdot(ik_z''')+\beta_2(z'')\cdot(ik_z''')^2\right]\right\}\frac{e^{ik_sx''}e^{ik_z'''(z''-z_s)}}{q_s^2-{k_z}'''^2}
\end{aligned}
\tag{A.12}
$$

Similarly like the previous calculation on the $L.H.S$ and using knowledge of contour integrals and residue theorem, integrate respectively over variables of ${k_z}'$, ${k_z}'''$, x', x'', ${k_x}''$ and ${k_z}''$ in the above equation, the above $G_0V_1G_0V_2G_0$ equation can be further simplified as the following form,

$$
\begin{aligned}
G_0V_1G_0V_2G_0 = {} & \frac{{\rho_0}^3}{(2\pi)^4}\left(\frac{\pi}{\rho_0}\right)^2\frac{\pi}{iq_g}e^{-iq_g(z_g+z_s)}\iint_{-\infty}^{\infty}dz'dz''e^{iq_g(z'+z'')} \\
& \left\{\left[\beta_1'(z')+\frac{iq_g}{cos^2\theta}(\beta_1(z')-\alpha_1(z'))\right]e^{iq_g(z'-z''}H(z'-z'') \right. \\
& \left[-\beta_1'(z')+\frac{iq_g}{cos^2\theta}(\beta_1(z')-\alpha_1(z'))\right]e^{-iq_g(z'-z''}H(z''-z') \\
& \left.\cdot\left[\beta_2'(z'')+\frac{iq_g}{cos^2\theta}(\beta_2(z'')-\alpha_2(z''))\right]\right\}
\end{aligned}
\tag{A.13}
$$

After exchanging $z'\leftrightarrow z''$ for the term $...e^{-iq_g(z'-z''}H(z''-z')$, and further simplify

the term in the $\{\cdots\}$, the result is shown as:

$$
\begin{aligned}
&G_0V_1G_0V_2G_0 \\
&= \frac{\rho_0}{16\pi}e^{-iq_g(z_g+z_s)}\iint_{-\infty}^{\infty}dz'dz''e^{2iq_gz'}H(z'-z'')\left\{\frac{1}{iq_g}\Big(\beta_1'(z')\beta_2'(z'')-\beta_2'(z')\beta_1'(z'')\Big)\right. \\
&+\frac{1}{cos^2\theta}\Big[\beta_1'(z')(\beta_2(z'')-\alpha_2(z''))+\beta_2'(z')(\beta_1(z'')-\alpha_1(z''))\Big] \\
&+\frac{1}{cos^2\theta}\Big[\beta_2'(z'')(\beta_1(z')-\alpha_1(z'))-\beta_1'(z'')(\beta_2(z')-\alpha_2(z'))\Big] \\
&\left.+\frac{iq_g}{cos^4\theta}\Big[(\beta_1(z')-\alpha_1(z'))(\beta_2(z'')-\alpha_2(z''))+(\beta_1(z'')-\alpha_1(z''))(\beta_2(z')-\alpha_2(z'))\Big]\right\}
\end{aligned}
\tag{A.14}
$$

Now doing a Fourier transform over $2q_g$ on both sides of the above result,

$$\int_{-\infty}^{\infty}d(2q_g)e^{-2iq_gz}\circledast(G_0V_1G_0V_2G_0)$$

Integrate over z', and collect all the coefficients of the common terms together, we get the final result of the term $G_0V_1G_0V_2G_0$:

$$
\begin{aligned}
G_0V_1G_0V_2G_0 =&\frac{\rho_0}{8}e^{-iq_g(z_g+z_s)}\left\{-\frac{1}{cos^4\theta}\alpha_1(z)\alpha_2(z)+\frac{tan^2\theta}{cos^2\theta}\alpha_1(z)\beta_2(z)\right. \\
&-\left(\frac{1}{cos^4\theta}+2\right)\beta_1(z)\beta_2(z)+\left(\frac{tan^2\theta}{cos^2\theta}+\frac{2}{cos^2\theta}\right)\alpha_2(z)\beta_1(z) \\
&-\frac{1}{2cos^4\theta}\alpha_1'(z)\int_{-\infty}^{z}\Big[\alpha_2(z')-\beta_2(z')\Big]dz' \\
&-\frac{1}{2cos^4\theta}\alpha_2'(z)\int_{-\infty}^{z}\Big[\alpha_1(z')-\beta_1(z')\Big]dz' \\
&+\frac{1}{2}(tan^4\theta-1)\beta_1'(z)\int_{-\infty}^{z}\Big[\alpha_2(z')-\beta_2(z')\Big]dz' \\
&+\frac{1}{2}(tan^4\theta-1)\beta_2'(z)\int_{-\infty}^{z}\Big[\alpha_1(z')-\beta_1(z')\Big]dz' \\
&\left.+4\int_{-\infty}^{z}\beta_1(z')\beta_2'(z')dz'\right\}
\end{aligned}
\tag{A.15}
$$

Due to the symmetry between the terms of $G_0V_1G_0V_2G_0$ and $G_0V_2G_0V_1G_0$, we can use the same method and perform the same procedure of calculation to obtain the result of the term $G_0V_2G_0V_1G_0$ in the 3^{rd} order:

$$\begin{aligned}
G_0V_2G_0V_1G_0 =& \frac{\rho_0}{8}e^{-iq_g(z_g+z_s)}\left\{-\frac{1}{cos^4\theta}\alpha_1(z)\alpha_2(z)+\left(\frac{tan^2\theta}{cos^2\theta}+\frac{2}{cos^2\theta}\right)\alpha_1(z)\beta_2(z)\right.\\
&-\left(\frac{1}{cos^4\theta}-2\right)\beta_1(z)\beta_2(z)+\frac{tan^2\theta}{cos^2\theta}\alpha_2(z)\beta_1(z)\\
&-\frac{1}{2cos^4\theta}\alpha_1'(z)\int_{-\infty}^{z}\Big[\alpha_2(z')-\beta_2(z')\Big]dz'\\
&-\frac{1}{2cos^4\theta}\alpha_2'(z)\int_{-\infty}^{z}\Big[\alpha_1(z')-\beta_1(z')\Big]dz'\\
&+\frac{1}{2}(tan^4\theta-1)\beta_1'(z)\int_{-\infty}^{z}\Big[\alpha_2(z')-\beta_2(z')\Big]dz'\\
&+\frac{1}{2}(tan^4\theta-1)\beta_2'(z)\int_{-\infty}^{z}\Big[\alpha_1(z')-\beta_1(z')\Big]dz'\\
&\left.-4\int_{-\infty}^{z}\beta_1(z')\beta_2'(z')dz'\right\} \qquad (A.16)
\end{aligned}$$

where $'$ means a derivative over the argument of that function.

Finally it is much more complicated to calculate the last term in the 3^{rd} order $G_0V_1G_0V_1G_0V_1G_0$, however, the basic steps taken are similar. Now let's write down this term:

$$\begin{aligned}
&G_0V_1G_0V_1G_0V_1G_0\\
&=\frac{{\rho_0}^4}{(2\pi)^8}\int\cdots\int_{-\infty}^{\infty}dx'dz'dx''dz''dx'''dz'''\iint_{-\infty}^{\infty}d{k_x}'d{k_z}'\frac{e^{i{k_x}'(x_g-x')}e^{i{k_z}'(z_g-z')}}{k^2-({k_x}'^2+{k_z}'^2)}\\
&\qquad\cdot\hat{V}_1(x',z')\iint_{-\infty}^{\infty}d{k_x}''d{k_z}''\frac{e^{i{k_x}''(x'-x'')}e^{i{k_z}''(z'-z'')}}{k^2-({k_x}''^2+{k_z}''^2)}\\
&\qquad\cdot\hat{V}_1(x'',z'')\iint_{-\infty}^{\infty}d{k_x}'''d{k_z}'''\frac{e^{i{k_x}'''(x''-x''')}e^{i{k_z}'''(z''-z''')}}{k^2-({k_x}'''^2+{k_z}'''^2)}
\end{aligned}$$

$$\cdot \hat{V}_1(x''', z''') \iint_{-\infty}^{\infty} dk_x'''' dk_z'''' \frac{e^{ik_x''''(x'''-x_s)} e^{ik_z''''(z'''-z_s)}}{k^2 - (k_x''''^2 + k_z''''^2)} \tag{A.17}$$

in which the operator $\hat{V}_1$ will be replaced by V_1 function with corresponding variables changed, after it acts on the behind Green's function:

$$V_1(x', z') = \frac{\omega^2}{K_0}\alpha_1(z') + \frac{(ik_x'')^2}{\rho_0}\beta_1(z') + \frac{1}{\rho_0}\left[\beta_1'(z') \cdot (ik_z'') + \beta_1(z') \cdot (ik_z'')^2\right] \tag{A.18}$$

As previous procedure, I perform a Fourier transform ovr x_g and x_s on both sides of the above equation (A.17):

$$\frac{1}{(2\pi)^2} \iint_{-\infty}^{\infty} dx_g dx_s e^{-ik_g x_g} e^{ik_s x_s} \circledast (G_0 V_1 G_0 V_1 G_0 V_1 G_0)$$

which will result two Delta functions $\delta(k_x' - k_g)$ and $\delta(k_s - k_x'''')$, so after integration over k_x' and k_x'''', and using the following contour integrals for $z' > z_g$ and $z''' > z_s$,

$$\int_{-\infty}^{\infty} dk_z' \frac{e^{ik_z'(z_g - z')}}{q_g^2 - k_z'^2} = \frac{\pi}{iq_g} e^{iq_g(z' - z_g)} \tag{A.19}$$

$$\int_{-\infty}^{\infty} dk_z'''' \frac{e^{ik_z''''(z'''-z_s)}}{q_s^2 - k_z''''^2} = \frac{\pi}{iq_s} e^{iq_s(z'''-z_s)} \tag{A.20}$$

$$\int_{-\infty}^{\infty} dk_z'''' \frac{\beta_1'(z''')}{\rho_0}(ik_z'''') \cdot \frac{e^{ik_z''''(z'''-z_s)}}{q_s^2 - k_z''''^2} = \frac{\pi}{\rho_0}\beta_1'(z''') e^{iq_s(z'''-z_s)} \tag{A.21}$$

$$\int_{-\infty}^{\infty} dk_z'''' \frac{\beta_1'(z''')}{\rho_0}(ik_z'''')^2 \cdot \frac{e^{ik_z''''(z'''-z_s)}}{q_s^2 - k_z''''^2} = \frac{\pi}{\rho_0}\beta_1'(z''')(iq_s) e^{iq_s(z'''-z_s)} \tag{A.22}$$

and also notice the integration over x' and x''' will lead to another two more Delta functions $\delta(k_x'' - k_g)$ and $\delta(k_s - k_x''')$, so equation (A.17), after integration over k_x'' and k_x''', is simplified as,

$$G_0 V_1 G_0 V_1 G_0 V_1 G_0 = \frac{\rho_0^4}{(2\pi)^6} \int \cdots \int_{-\infty}^{\infty} dz' dx'' dz'' dz''' dk_z'' dk_z'''$$
$$\cdot \frac{\pi}{iq_g} e^{iq_g(z'-z_g)} \left\{ \frac{k^2}{\rho_0}\alpha_1(z') + \frac{(ik_g)^2}{\rho_0}\beta_1(z') + \frac{1}{\rho_0}\left[\beta_1'(z') \cdot (ik_z'') + \beta_1(z') \cdot (ik_z'')^2\right] \right\}$$

$$\cdot e^{ik_g x''}\frac{e^{ik_z{}''(z'-z'')}}{q_g^2-k_z{}''^2}\left\{\frac{k^2}{\rho_0}\alpha_1(z'')+\frac{(ik_s)^2}{\rho_0}\beta_1(z'')+\frac{1}{\rho_0}\left[\beta_1'(z'')\cdot(ik_z{}''')+\beta_1(z'')\cdot(ik_z{}''')^2\right]\right\}$$
$$\cdot e^{ik_s x''}\frac{e^{ik_z{}'''(z''-z''')}}{q_s^2-k_z{}'''^2}\left\{\frac{\pi}{iq_s}e^{iq_s(z'''-z_s)}\Big[\frac{k^2}{\rho_0}\alpha_1(z''')+\frac{(ik_s)^2}{\rho_0}\beta_1(z''')\Big]\right.$$
$$\left.+\frac{\pi}{\rho_0}\beta_1'(z''')e^{iq_s(z'''-z_s)}+\frac{\pi}{\rho_0}\beta_1(z''')\cdot(iq_s)e^{iq_s(z'''-z_s)}\right\} \tag{A.23}$$

Easily notice some quick mathematical results in the above formula,

$$\int_{-\infty}^{\infty}dx''e^{-ik_g x''}e^{ik_s x''}=2\pi\delta(k_s-k_g) \tag{A.24}$$
$$\int_{-\infty}^{\infty}dk_z{}''\frac{e^{ik_z{}''(z'-z'')}}{q_g^2-k_z{}''^2}=\frac{\pi}{iq_g}e^{iq_g|z'-z''|} \tag{A.25}$$
$$\int_{-\infty}^{\infty}dk_z{}''\frac{\beta_1'(z')}{\rho_0}(ik_z{}'')\cdot\frac{e^{ik_z{}''(z'-z'')}}{q_g^2-k_z{}''^2}=\frac{\pi}{\rho_0}\beta_1'(z')e^{iq_g|z'-z''|} \tag{A.26}$$
$$\int_{-\infty}^{\infty}dk_z{}''\frac{\beta_1(z')}{\rho_0}(ik_z{}'')^2\cdot\frac{e^{ik_z{}''(z'-z'')}}{q_g^2-k_z{}''^2}=\frac{\pi}{\rho_0}\beta_1'(z')(iq_g)e^{iq_g|z'-z''|} \tag{A.27}$$
$$\int_{-\infty}^{\infty}dk_z{}'''\frac{e^{ik_z{}'''(z''-z''')}}{q_g^2-k_z{}'''^2}=\frac{\pi}{iq_g}e^{iq_g|z''-z'''|} \tag{A.28}$$
$$\int_{-\infty}^{\infty}dk_z{}'''\frac{\beta_1'(z'')}{\rho_0}(ik_z{}''')\cdot\frac{e^{ik_z{}'''(z''-z''')}}{q_g^2-k_z{}'''^2}=\frac{\pi}{\rho_0}\beta_1'(z'')e^{iq_g|z''-z'''|} \tag{A.29}$$
$$\int_{-\infty}^{\infty}dk_z{}'''\frac{\beta_1(z'')}{\rho_0}(ik_z{}''')^2\cdot\frac{e^{ik_z{}'''(z''-z''')}}{q_g^2-k_z{}'''^2}=\frac{\pi}{\rho_0}\beta_1'(z'')(iq_g)e^{iq_g|z''-z'''|} \tag{A.30}$$

here the absolute value $|...|$ can be eliminated by using two Heaviside functions. So a further simplification after the above integrations, the term is expressed as,

$$G_0V_1G_0V_1G_0V_1G_0=\frac{{\rho_0}^4}{(2\pi)^5}\left(\frac{\pi}{\rho_0}\right)^3\frac{\pi}{iq_g}e^{-iq_g(z_g+z_s)}\iiint_{-\infty}^{\infty}dz'dz''dz'''(E_1+E_2+E_3+E_4) \tag{A.31}$$

where E_1, E_2, E_3 and E_4 are defined by the following expressions:

$$E_1 = M_1(z')M_1(z'')M_1(z''')H(z'-z'')H(z''-z''')e^{2iq_g z'} \tag{A.32}$$

$$E_2 = M_1(z')N_1(z'')M_1(z''')H(z'-z'')H(z'''-z'')e^{2iq_g(z'-z''+z''')} \tag{A.33}$$

$$E_3 = N_1(z')M_1(z'')M_1(z''')H(z''-z')H(z''-z''')e^{2iq_g z''} \tag{A.34}$$

$$E_4 = N_1(z')N_1(z'')M_1(z''')H(z''-z')H(z'''-z'')e^{2iq_g z'''} \tag{A.35}$$

and the functions N_1 and M_1 in the above expressions are defined as,

$$M_1(z) = \beta_1'(z) + \frac{iq_g}{cos^2\theta}\Big[\beta_1(z) - \alpha_1(z)\Big] \tag{A.36}$$

$$N_1(z) = -\beta_1'(z) + \frac{iq_g}{cos^2\theta}\Big[\beta_1(z) - \alpha_1(z)\Big] \tag{A.37}$$

Now I will calculate E_1, E_2, E_3 and E_4 respectively. Consider the factor $\frac{1}{iq_g}$ outside of the triple integrals in equation (A.31), then E_1 can be written as,

$$\begin{aligned}
\frac{1}{iq_g}E_1 =& \underline{\frac{1}{iq_g}}\beta_1'(z')\beta_1'(z'')\beta_1'(z''') \\
&+ \underline{\frac{1}{cos^2\theta}}\Big\{\beta_1'(z'')\beta_1'(z''')\Big[\beta_1(z') - \alpha_1(z')\Big] + \beta_1'(z')\beta_1'(z''')\Big[\beta_1(z'') - \alpha_1(z'')\Big] \\
&+\beta_1'(z')\beta_1'(z'')\Big[\beta_1(z''') - \alpha_1(z''')\Big]\Big\} \\
&+ \underline{\frac{iq_g}{cos^4\theta}}\Big\{\beta_1'(z''')\Big[\beta_1(z') - \alpha_1(z')\Big]\Big[\beta_1(z'') - \alpha_1(z'')\Big] \\
&+\beta_1'(z'')\Big[\beta_1(z') - \alpha_1(z')\Big]\Big[\beta_1(z''') - \alpha_1(z''')\Big] \\
&+\beta_1'(z')\Big[\beta_1(z'') - \alpha_1(z'')\Big]\Big[\beta_1(z''') - \alpha_1(z''')\Big]\Big\}
\end{aligned} \tag{A.38}$$

At the end of the calculation of the whole term, we'll perform a Fourier transform over $2q_g$,

$$\int_{-\infty}^{\infty} d(2q_g)e^{-2iq_g z}\,[...]$$

hence, for E_1 we will have the following integrals after performing the Fourier transform:

$$\int_{-\infty}^{\infty} d(2q_g) e^{-2iq_g z} e^{2iq_g z'} = 2\pi\delta(z - z') \tag{A.39}$$

$$\int_{-\infty}^{\infty} d(2q_g)(iq_g) e^{-2iq_g(z-z')} [...] = -\frac{1}{2}\int_{-\infty}^{\infty} d(2q_g)\frac{d}{dz}\left[e^{-2iq_g(z-z')}...\right]$$

$$= -\frac{1}{2}\frac{d}{dz}\left[2\pi\delta(z - z')...\right] \tag{A.40}$$

$$\int_{-\infty}^{\infty} d(2q_g)(iq_g)^2 e^{-2iq_g(z-z')} [...] = \frac{1}{4}\frac{d^2}{dz^2}\left[2\pi\delta(z - z')...\right] \tag{A.41}$$

$$\int_{-\infty}^{\infty} d(2q_g)\frac{1}{iq_g} e^{-2iq_g(z-z')} [...] = \int_{-\infty}^{\infty} d(2q_g)\frac{1}{iq_g}\int_{-\infty}^{z}\frac{d}{du}\left[e^{-2iq_g(u-z')}...\right] du$$

$$= -2\int_{-\infty}^{z} du\left[2\pi\delta(u - z')...\right] \tag{A.42}$$

and use the partial integration skills below,

$$\int_{-\infty}^{z} udv = uv\Big|_{-\infty}^{z} - \int_{-\infty}^{z} vdu \tag{A.43}$$

$$\int_{-\infty}^{z} dz'\alpha_1(z')\int_{-\infty}^{z'}\alpha_1(z'')dz'' = \frac{1}{2}\left[\int_{-\infty}^{z}\alpha_1(z')dz'\right]^2 \tag{A.44}$$

So, after the Fourier transform and integration over the three variables of z', z'', and z''', E_1 term turns out to be:

$$\int_{-\infty}^{\infty} d(2q_g) e^{-2iq_g z}\frac{1}{iq_g}\iiint_{-\infty}^{\infty} dz'dz''dz'''\Big[E_1\Big]$$

$$= 2\pi\left\{-\frac{1}{3}\beta_1^3(z) + \frac{1}{2cos^2\theta}\beta_1^2(z)\Big[\beta_1(z) - \alpha_1(z)\Big]\right.$$

$$-\frac{1}{2cos^4\theta}\beta_1(z)\Big[\beta_1(z) - \alpha_1(z)\Big]^2 + \frac{1}{4cos^6\theta}\Big[\beta_1(z) - \alpha_1(z)\Big]^3$$

$$\left.+\frac{3}{4cos^6\theta}\alpha_1(z)\alpha_1'(z)\int_{-\infty}^{z}\Big[\beta_1(z') - \alpha_1(z')\Big]dz'\right.$$

$$
\begin{aligned}
&+\frac{1}{cos^4\theta}\Big(1-\frac{3}{4cos^2\theta}\Big)\alpha_1(z)\beta_1'(z)\int_{-\infty}^{z}\Big[\beta_1(z')-\alpha_1(z')\Big]dz' \\
&+\frac{1}{2cos^4\theta}\Big(1-\frac{3}{2cos^2\theta}\Big)\beta_1(z)\alpha_1'(z)\int_{-\infty}^{z}\Big[\beta_1(z')-\alpha_1(z')\Big]dz' \\
&+\frac{1}{cos^2\theta}\Big[1-\frac{3}{4cos^2\theta}\big(1-tan^2\theta\big)\Big]\beta_1(z)\beta_1'(z)\int_{-\infty}^{z}\Big[\beta_1(z')-\alpha_1(z')\Big]dz' \\
&-\frac{1}{8cos^6\theta}\alpha_1''(z)\Big[\int_{-\infty}^{z}\big(\beta_1(z')-\alpha_1(z')\big)dz'\Big]^2 \\
&-\frac{1}{4cos^4\theta}\big(1-\frac{1}{2cos^2\theta}\big)\beta_1''(z)\Big[\int_{-\infty}^{z}\big(\beta_1(z')-\alpha_1(z')\big)dz'\Big]^2\Bigg\}
\end{aligned}
\tag{A.45}
$$

Next, due to the similarity of the terms E_3 and E_4 with the term E_1, we can employ the same procedure, calculation methods and integration skills. Here I directly list out the final calculation results of the two terms:

$$
\begin{aligned}
&\int_{-\infty}^{\infty}d(2q_g)e^{-2iq_gz}\frac{1}{iq_g}\iiint_{-\infty}^{\infty}dz'dz''dz'''\Big[E_3\Big] \\
&=2\pi\Bigg\{\frac{2}{3}\beta_1^3(z)-\frac{1}{cos^2\theta}\beta_1^2(z)\Big[\beta_1(z)-\alpha_1(z)\Big]+\frac{1}{2cos^6\theta}\beta_1(z)\Big[\beta_1(z)-\alpha_1(z)\Big]^3 \\
&-\frac{1}{cos^4\theta}\big(1-\frac{3}{2cos^2\theta}\big)\beta_1'(z)\Big[\beta_1(z)-\alpha_1(z)\Big]\int_{-\infty}^{z}\Big[\beta_1(z')-\alpha_1(z')\Big]dz' \\
&-\frac{3}{2cos^6\theta}\alpha_1'(z)\Big[\beta_1(z)-\alpha_1(z)\Big]\int_{-\infty}^{z}\Big[\beta_1(z')-\alpha_1(z')\Big]dz' \\
&+\frac{1}{4cos^4\theta}\Big[tan^2\theta-1\Big]\beta_1''(z)\Big[\int_{-\infty}^{z}\big(\beta_1(z')-\alpha_1(z')\big)dz'\Big]^2 \\
&-\frac{1}{4cos^6\theta}\alpha_1''(z)\Big[\int_{-\infty}^{z}\big(\beta_1(z')-\alpha_1(z')\big)dz'\Big]^2\Bigg\}
\end{aligned}
\tag{A.46}
$$

and,

$$
\begin{aligned}
&\int_{-\infty}^{\infty} d(2q_g) e^{-2iq_g z} \frac{1}{iq_g} \iiint_{-\infty}^{\infty} dz' dz'' dz''' \Big[E_4\Big] \\
&= 2\pi \Bigg\{ -\frac{1}{3}\beta_1^3(z) + \frac{1}{2cos^2\theta}\beta_1^2(z)\Big[\beta_1(z) - \alpha_1(z)\Big] \\
&+ \frac{1}{2cos^4\theta}\beta_1(z)\Big[\beta_1(z) - \alpha_1(z)\Big]^2 + \frac{1}{4cos^6\theta}\Big[\beta_1(z) - \alpha_1(z)\Big]^3 \\
&+ \frac{3}{4cos^6\theta}\alpha_1(z)\Big[\alpha_1'(z) - \beta_1'(z)\Big] \int_{-\infty}^{z} \Big[\beta_1(z') - \alpha_1(z')\Big] dz' \\
&+ \frac{1}{2cos^4\theta}\big(-1 - \frac{3}{2cos^2\theta}\big)\beta_1(z)\alpha_1'(z) \int_{-\infty}^{z} \Big[\beta_1(z') - \alpha_1(z')\Big] dz' \\
&+ \frac{1}{cos^2\theta}\Big[-1 + \frac{1}{2cos^2\theta}\big(1 + \frac{3}{2cos^2\theta}\big)\Big]\beta_1(z)\beta_1'(z) \int_{-\infty}^{z} \Big[\beta_1(z') - \alpha_1(z')\Big] dz' \\
&- \frac{1}{8cos^6\theta}\alpha_1''(z)\Big[\int_{-\infty}^{z} \big(\beta_1(z') - \alpha_1(z')\big) dz' \Big]^2 \\
&- \frac{1}{4cos^4\theta}\big(1 - \frac{1}{2cos^2\theta}\big)\beta_1''(z)\Big[\int_{-\infty}^{z} \big(\beta_1(z') - \alpha_1(z')\big) dz' \Big]^2 \Bigg\}
\end{aligned}
\tag{A.47}
$$

Finally, let's calculate the term E_2 which is the most complicated term among the four terms listed previously, since it contains a multiple-related "generator". Recall the expression of term E_2 in equation (A.33) where the two Heaviside functions, $H(z' - z'')$ and $H(z''' - z'')$, express the "lower-higher-lower" spatial relation, a characteristic of internal multiple generation. To begin with the calculation, let's introduce a new variable $u = z' - z'' + z'''$ to connect the three variables and make the calculation a further step of simplicity, then

$$
\begin{aligned}
&z'' = z' + z''' - u, \quad \Rightarrow dz'' = -du \\
&H(z' - z'') = H(u - z'''), \quad H(z''' - z'') = H(u - z')
\end{aligned}
$$

and the integral over E_2 will become as,

$$\int_{-\infty}^{\infty} dz' \int_{-\infty}^{\infty} dz'' \int_{-\infty}^{\infty} dz''' H(z'-z'')H(z'''-z'')e^{2iq_g(z'-z''+z''')}\Big[\cdots\Big]$$
$$\Rightarrow \int_{-\infty}^{\infty} dz' \int_{-\infty}^{\infty} dz''' \int_{-\infty}^{\infty} du H(u-z')H(u-z''')e^{2iq_g u}\Big[\cdots\Big]_{z''=z'+z'''-u}$$

Substitue the above variable relation into term E_2, then the expression $\Big[\cdots\Big]$ is displayed as,

$$\begin{aligned}
&\frac{1}{iq_g}M_1(z')N_1(z'+z'''-u)M_1(z''') = -\underline{\frac{1}{iq_g}}\beta_1'(z')\beta_1'(z'+z'''-u)\beta_1'(z''') \\
&+\underline{\frac{1}{cos^2\theta}}\Big\{-\beta_1'(z'+z'''-u)\beta_1'(z''')\Big[\beta_1(z')-\alpha_1(z')\Big]+\beta_1'(z')\beta_1'(z''') \\
&\cdot\Big[\beta_1(z'+z'''-u)-\alpha_1(z'+z'''-u)\Big]-\beta_1'(z')\beta_1'(z'+z'''-u)\Big[\beta_1(z''')-\alpha_1(z''')\Big]\Big\} \\
&+\underline{\frac{iq_g}{cos^4\theta}}\Big\{\beta_1'(z''')\Big[\beta_1(z')-\alpha_1(z')\Big]\Big[\beta_1(z'+z'''-u)-\alpha_1(z'+z'''-u)\Big] \\
&-\beta_1'(z'+z'''-u)\Big[\beta_1(z')-\alpha_1(z')\Big]\Big[\beta_1(z''')-\alpha_1(z''')\Big] \\
&+\beta_1'(z')\Big[\beta_1(z''')-\alpha_1(z''')\Big]\Big[\beta_1(z'+z'''-u)-\alpha_1(z'+z'''-u)\Big]\Big\} \\
&+\underline{\frac{(iq_g)^2}{cos^6\theta}}\Big\{\Big[\beta_1(z')-\alpha_1(z')\Big]\Big[\beta_1(z''')-\alpha_1(z''')\Big]\Big[\beta_1(z'+z'''-u)-\alpha_1(z'+z'''-u)\Big]\Big\}
\end{aligned} \tag{A.48}$$

Performing a Fourier transform $\int_{-\infty}^{\infty} d(2q_g)e^{-2iq_g z}[\cdots]$ on both sides of the equation, which will result in a delta function $\delta(z-u)$. Similarly, we have to employ the same calculation skills shown in equations (A.40,A.41,A.42). Now let's calculate the above equation term by term.

$$\begin{aligned}
&-\frac{1}{iq_g}\beta_1'(z')\beta_1'(z'+z'''-u)\beta_1'(z''') \\
&\to 2\int_{-\infty}^{z} d\eta \int_{-\infty}^{\infty} dz' \int_{-\infty}^{\infty} dz''' \int_{-\infty}^{\infty} du\delta(\eta-u)\beta_1'(z')\beta_1'(z'+z'''-u)\beta_1'(z''')H(u-z')H(u-z''') \\
&= 2\int_{-\infty}^{z} du \int_{-\infty}^{u} dz'\beta_1'(z') \int_{-\infty}^{u} dz'''\beta_1'(z''')\beta_1'(z'+z'''-u)
\end{aligned} \tag{A.49}$$

$$
\begin{aligned}
&-\beta_1'(z'+z'''-u)\beta_1'(z''')\Big[\beta_1(z')-\alpha_1(z')\Big] \\
&\to -\int_{-\infty}^{z} dz'''\beta_1'(z''')\int_{-\infty}^{z} dz'\Big[\beta_1(z')-\alpha_1(z')\Big]\beta_1'(z'+z'''-z) \\
&=-\int_{-\infty}^{z} dz'''\beta_1'(z''')\left\{\Big[\beta_1(z')-\alpha_1(z')\Big]\beta_1'(z''')-\int_{-\infty}^{z} dz'\Big[\beta_1'(z')-\alpha_1'(z')\Big]\beta_1(z'+z'''-z)\right\} \\
&=-\frac{1}{2}\beta_1^2(z)\Big[\beta_1(z)-\alpha_1(z)\Big]+\int_{-\infty}^{z} dz'\Big[\beta_1'(z')-\alpha_1'(z')\Big]\int_{-\infty}^{z} dz'''\beta_1'(z''')\beta_1(z'+z'''-z)
\end{aligned}
\tag{A.50}
$$

$$
\begin{aligned}
&\beta_1'(z')\beta_1'(z''')\Big[\beta_1(z'+z'''-u)-\alpha_1(z'+z'''-u)\Big] \\
&\to \int_{-\infty}^{z} dz'\beta_1'(z')\int_{-\infty}^{z} dz'''\beta_1'(z''')\Big[\beta_1(z'+z'''-z)-\alpha_1(z'+z'''-z)\Big]
\end{aligned}
\tag{A.51}
$$

$$
\begin{aligned}
&-\beta_1'(z')\beta_1'(z'+z'''-u)\Big[\beta_1(z''')-\alpha_1(z''')\Big] \\
&\to -\int_{-\infty}^{z} dz'\beta_1'(z')\int_{-\infty}^{z} dz'''\Big[\beta_1(z''')-\alpha_1(z''')\Big]\beta_1'(z'+z'''-z) \\
&=-\int_{-\infty}^{z} dz'\beta_1'(z')\left\{\Big[\beta_1(z)-\alpha_1(z)\Big]\beta_1(z')-\int_{-\infty}^{z} dz'''\Big[\beta_1'(z''')-\alpha_1'(z''')\Big]\beta_1(z'+z'''-z)\right\} \\
&=-\frac{1}{2}\beta_1^2(z)\Big[\beta_1(z)-\alpha_1(z)\Big]+\int_{-\infty}^{z} dz'\beta_1'(z')\int_{-\infty}^{z} dz'''\Big[\beta_1'(z''')-\alpha_1'(z''')\Big]\beta_1(z'+z'''-z)
\end{aligned}
\tag{A.52}
$$

$$
\begin{aligned}
&\beta_1'(z''')\Big[\beta_1(z')-\alpha_1(z')\Big]\Big[\beta_1(z'+z'''-u)-\alpha_1(z'+z'''-u)\Big] \\
&\to -\frac{1}{2}\frac{d}{dz}\left\{\int_{-\infty}^{z} dz'\Big[\beta_1(z')-\alpha_1(z')\Big]\int_{-\infty}^{z} dz'''\beta_1'(z''')\Big[\beta_1(z'+z'''-z)-\alpha_1(z'+z'''-z)\Big]\right\}
\end{aligned}
$$

$$= -\frac{1}{2}\Bigg\{\beta_1'(z)\int_{-\infty}^{z}\Big[\beta_1(z')-\alpha_1(z')\Big]^2 dz' + \int_{-\infty}^{z} dz'\Big[\beta_1'(z')-\alpha_1'(z')\Big]\int_{-\infty}^{z} dz'''\beta_1'(z''')\Big[\beta_1(z'+z'''-z)-\alpha_1(z'+z'''-z)\Big]\Bigg\} \tag{A.53}$$

$$\begin{aligned}
&-\beta_1'(z'+z'''-u)\Big[\beta_1(z')-\alpha_1(z')\Big]\Big[\beta_1(z''')-\alpha_1(z''')\Big]\\
&\to \frac{1}{2}\frac{d}{dz}\Bigg\{\int_{-\infty}^{z} dz'\Big[\beta_1(z')-\alpha_1(z')\Big]\int_{-\infty}^{z} dz'''\Big[\beta_1(z''')-\alpha_1(z''')\Big]\beta_1'(z'+z'''-z)\Bigg\}\\
&= \frac{1}{2}\Bigg\{2\Big[\beta_1(z)-\alpha_1(z)\Big]\int_{-\infty}^{z}\beta_1'(z')\Big[\beta_1(z')-\alpha_1(z')\Big]dz'\\
&\quad -\int_{-\infty}^{z} dz'\Big[\beta_1(z')-\alpha_1(z')\Big]\int_{-\infty}^{z} dz'''\beta_1''(z'+z'''-z)\Big[\beta_1(z''')-\alpha_1(z''')\Big]\Bigg\}\\
&= \frac{1}{2}\Bigg\{2\Big[\beta_1(z)-\alpha_1(z)\Big]\int_{-\infty}^{z}\beta_1'(z')\Big[\beta_1(z')-\alpha_1(z')\Big]dz' - \int_{-\infty}^{z} dz'\Big[\beta_1(z')-\alpha_1(z')\Big]\\
&\quad \Big[\big(\beta_1(z)-\alpha_1(z)\big)\beta_1'(z') - \int_{-\infty}^{z} dz'''\big(\beta_1'(z''')-\alpha_1'(z''')\big)\beta_1'(z'+z'''-z)\Big]\Bigg\}\\
&= \frac{1}{2}\Bigg\{\Big[\beta_1(z)-\alpha_1(z)\Big]\int_{-\infty}^{z}\beta_1'(z')\Big[\beta_1(z')-\alpha_1(z')\Big]dz'\\
&\quad +\Big[\beta_1(z)-\alpha_1(z)\Big]\int_{-\infty}^{z}\beta_1(z')\Big[\beta_1'(z')-\alpha_1'(z')\Big]dz'\\
&\quad -\int_{-\infty}^{z} dz'\Big[\beta_1'(z')-\alpha_1'(z')\Big]\int_{-\infty}^{z} dz'''\Big[\beta_1'(z''')-\alpha_1'(z''')\Big]\beta_1(z'+z'''-z)\Bigg\}
\end{aligned} \tag{A.54}$$

$$\begin{aligned}
&\beta_1'(z')\Big[\beta_1(z''')-\alpha_1(z''')\Big]\Big[\beta_1(z'+z'''-u)-\alpha_1(z'+z'''-u)\Big]\\
&\to -\frac{1}{2}\frac{d}{dz}\Bigg\{\int_{-\infty}^{z} dz'\beta_1'(z')\int_{-\infty}^{z}\Big[\beta_1(z''')-\alpha_1(z''')\Big]\Big[\beta_1(z'+z'''-z)-\alpha_1(z'+z'''-z)\Big]dz'''\Bigg\}\\
&= -\frac{1}{2}\Bigg\{\beta_1'(z)\int_{-\infty}^{z}\Big[\beta_1(z')-\alpha_1(z')\Big]^2 dz' + \Big[\beta_1(z)-\alpha_1(z)\Big]\int_{-\infty}^{z}\beta_1'(z')\Big[\beta_1(z')-\alpha_1(z')\Big]dz'
\end{aligned}$$

$$
\begin{aligned}
&- \int_{-\infty}^{z} dz' \beta_1'(z') \int_{-\infty}^{z} dz''' \Big[\beta_1(z''') - \alpha_1(z''')\Big] \Big[\beta_1'(z' + z''' - z) - \alpha_1'(z' + z''' - z)\Big] \Bigg\} \\
&= -\frac{1}{2} \Bigg\{ \beta_1'(z) \int_{-\infty}^{z} \Big[\beta_1(z') - \alpha_1(z')\Big]^2 dz' \\
&+ \int_{-\infty}^{z} dz' \beta_1'(z') \int_{-\infty}^{z} dz''' \Big[\beta_1'(z''') - \alpha_1'(z''')\Big] \Big[\beta_1(z' + z''' - z) - \alpha_1(z' + z''' - z)\Big] \Bigg\}
\end{aligned} \tag{A.55}
$$

$$
\begin{aligned}
&\Big[\beta_1(z') - \alpha_1(z')\Big] \Big[\beta_1(z''') - \alpha_1(z''')\Big] \Big[\beta_1(z' + z''' - u) - \alpha_1(z' + z''' - u)\Big] \\
&\to \frac{1}{4} \frac{d^2}{dz^2} \Bigg\{ \int_{-\infty}^{z} dz' \Big[\beta_1(z') - \alpha_1(z')\Big] \int_{-\infty}^{z} dz''' \Big[\beta_1(z''') - \alpha_1(z''')\Big] \\
&\qquad \Big[\beta_1(z' + z''' - z) - \alpha_1(z' + z''' - z)\Big] \Bigg\} \\
&= \frac{1}{4} \frac{d}{dz} \Bigg\{ 2\Big[\beta_1(z) - \alpha_1(z)\Big] \int_{-\infty}^{z} \Big[\beta_1(z') - \alpha_1(z')\Big]^2 dz' - \int_{-\infty}^{z} dz' \Big[\beta_1(z') - \alpha_1(z')\Big] \\
&\quad \int_{-\infty}^{z} dz''' \Big[\beta_1(z''') - \alpha_1(z''')\Big] \Big[\beta_1'(z' + z''' - z) - \alpha_1'(z' + z''' - z)\Big] \Bigg\} \\
&= \frac{1}{4} \frac{d}{dz} \Bigg\{ \Big[\beta_1(z) - \alpha_1(z)\Big] \int_{-\infty}^{z} \Big[\beta_1(z') - \alpha_1(z')\Big]^2 dz' + \int_{-\infty}^{z} dz' \Big[\beta_1(z') - \alpha_1(z')\Big] \\
&\quad \int_{-\infty}^{z} dz''' \Big[\beta_1'(z''') - \alpha_1'(z''')\Big] \Big[\beta_1(z' + z''' - z) - \alpha_1(z' + z''' - z)\Big] \Bigg\} \\
&= \frac{1}{4} \Bigg\{ \Big[\beta_1'(z) - \alpha_1'(z)\Big] \int_{-\infty}^{z} \Big[\beta_1(z') - \alpha_1(z')\Big]^2 dz' + \Big[\beta_1(z) - \alpha_1(z)\Big]^3 \\
&\quad + \Big[\beta_1(z) - \alpha_1(z)\Big] \int_{-\infty}^{z} \Big[\beta_1'(z') - \alpha_1'(z')\Big] \Big[\beta_1(z') - \alpha_1(z')\Big] dz' \\
&\quad + \Big[\beta_1'(z) - \alpha_1'(z)\Big] \int_{-\infty}^{z} \Big[\beta_1(z') - \alpha_1(z')\Big]^2 dz' - \int_{-\infty}^{z} dz' \Big[\beta_1(z') - \alpha_1(z')\Big] \\
&\quad \int_{-\infty}^{z} dz''' \Big[\beta_1'(z''') - \alpha_1'(z''')\Big] \Big[\beta_1'(z' + z''' - z) - \alpha_1'(z' + z''' - z)\Big] \Bigg\} \\
&= \frac{1}{4} \Bigg\{ \Big[\beta_1(z) - \alpha_1(z)\Big]^3 + 2\Big[\beta_1'(z) - \alpha_1'(z)\Big] \int_{-\infty}^{z} \Big[\beta_1(z') - \alpha_1(z')\Big]^2 dz'
\end{aligned}
$$

$$+\int_{-\infty}^{z} dz' \Big[\beta_1'(z') - \alpha_1'(z')\Big] \int_{-\infty}^{z} dz''' \Big[\beta_1'(z''') - \alpha_1'(z''')\Big] \Big[\beta_1(z' + z''' - z) - \alpha_1(z' + z''' - z)\Big] \Bigg\} \tag{A.56}$$

Now we put all the above results together and simplify the final result of term E_2 by collecting the coefficients of similar terms, and we have:

$$\begin{aligned} E_2 = 2\pi \Bigg\{ & -\frac{1}{cos^2\theta}\beta_1^2(z)\Big[\beta_1(z) - \alpha_1(z)\Big] + \frac{1}{2cos^4\theta}\beta_1(z)\Big[\beta_1(z) - \alpha_1(z)\Big]^2 \\ & + \frac{1}{4cos^6\theta}\Big[\beta_1(z) - \alpha_1(z)\Big]^3 - \frac{1}{cos^4\theta}\beta_1'(z)\int_{-\infty}^{z}\Big[\beta_1(z') - \alpha_1(z')\Big]^2 dz' \\ & + \frac{1}{2cos^6\theta}\Big[\beta_1'(z) - \alpha_1'(z)\Big]\int_{-\infty}^{z}\Big[\beta_1(z') - \alpha_1(z')\Big]^2 dz' + MUL \Bigg\} \end{aligned} \tag{A.57}$$

where "MUL" is called as multiple term which is expressed as,

$$\begin{aligned} MUL = & -\frac{1}{4cos^6\theta}\int_{-\infty}^{z} dz'\alpha_1'(z')\int_{-\infty}^{z} dz'''\alpha_1'(z''')\alpha_1(z' + z''' - z) \\ & + \Big(-\frac{1}{2cos^4\theta} + \frac{1}{4cos^6\theta}\Big)\int_{-\infty}^{z} dz'\alpha_1'(z')\int_{-\infty}^{z} dz'''\alpha_1'(z''')\beta_1(z' + z''' - z) \\ & + \Big(-\frac{1}{cos^4\theta} + \frac{1}{2cos^6\theta}\Big)\int_{-\infty}^{z} dz'\alpha_1'(z')\int_{-\infty}^{z} dz'''\beta_1'(z''')\alpha_1(z' + z''' - z) \\ & + \Big(-\frac{2}{cos^2\theta} + \frac{2}{cos^4\theta} - \frac{1}{2cos^6\theta}\Big)\int_{-\infty}^{z} dz'\alpha_1'(z')\int_{-\infty}^{z} dz'''\beta_1'(z''')\beta_1(z' + z''' - z) \\ & + \Big(-\frac{1}{cos^2\theta} + \frac{1}{cos^4\theta} - \frac{1}{4cos^6\theta}\Big)\int_{-\infty}^{z} dz'\beta_1'(z')\int_{-\infty}^{z} dz'''\beta_1'(z''')\alpha_1(z' + z''' - z) \\ & + \Big(\frac{3}{cos^2\theta} - \frac{3}{2cos^4\theta} + \frac{1}{4cos^6\theta}\Big)\int_{-\infty}^{z} dz'\beta_1'(z')\int_{-\infty}^{z} dz'''\beta_1'(z''')\beta_1(z' + z''' - z) \end{aligned} \tag{A.58}$$

So, the final calculated result for the 3^{rd} term, equation (A.31), can be clearly expressed as:

$$\begin{aligned} G_0V_1G_0V_1G_0V_1G_0 =& \frac{\rho_0}{16}e^{-iq_g(z_g+z_s)}\iiint_{-\infty}^{\infty} dz'dz''dz''' \frac{1}{2\pi}\frac{(E_1+E_2+E_3+E_4)}{iq_g} \\ =& \frac{\rho_0}{16}e^{-iq_g(z_g+z_s)}\{intE1234\} \end{aligned} \tag{A.59}$$

where $\{intE1234\}$ term is a denotion of the integration result:

$$\{intE1234\} = \iiint_{-\infty}^{\infty} dz'dz''dz''' \frac{1}{2\pi}\frac{(E_1+E_2+E_3+E_4)}{iq_g} \tag{A.60}$$

and its computed result is explicitely expressed by summing together all the results of E_1, E_2, E_3 and E_4 terms:

$$\begin{aligned} \{intE1234\} =& -\frac{5}{4cos^6\theta}\Big[\alpha_1(z)-\beta_1(z)\Big]^3 + \frac{1}{2cos^4\theta}\beta_1(z)\Big[\alpha_1(z)-\beta_1(z)\Big]^2 \\ &+ \frac{1}{cos^2\theta}\beta_1^2(z)\Big[\alpha_1(z)-\beta_1(z)\Big] - \frac{1}{2cos^6\theta}\alpha_1''(z)\Big[\int_{-\infty}^{z}\big(\alpha_1(z')-\beta_1(z')\big)dz'\Big]^2 \\ &- \frac{1}{2cos^4\theta}(1-tan^2\theta)\beta_1''(z)\Big[\int_{-\infty}^{z}\big(\alpha_1(z')-\beta_1(z')\big)dz'\Big]^2 \\ &- \frac{3}{cos^6\theta}\alpha_1(z)\alpha_1'(z)\int_{-\infty}^{z}\Big[\alpha_1(z')-\beta_1(z')\Big]dz' \\ &+ \frac{1}{cos^4\theta}(3sec^2\theta-2)\alpha_1(z)\beta_1'(z)\int_{-\infty}^{z}\Big[\alpha_1(z')-\beta_1(z')\Big]dz' \\ &+ \frac{3}{cos^6\theta}\beta_1(z)\alpha_1'(z)\int_{-\infty}^{z}\Big[\alpha_1(z')-\beta_1(z')\Big]dz' \\ &+ \frac{1}{cos^4\theta}(3tan^2\theta-1)\beta_1(z)\beta_1'(z)\int_{-\infty}^{z}\Big[\alpha_1(z')-\beta_1(z')\Big]dz' \\ &- \frac{1}{cos^4\theta}\beta_1'(z)\int_{-\infty}^{z}\Big[\alpha_1(z')-\beta_1(z')\Big]^2dz' \\ &- \frac{1}{2cos^6\theta}\Big[\alpha_1'(z)-\beta_1'(z)\Big]\int_{-\infty}^{z}\Big[\alpha_1(z')-\beta_1(z')\Big]^2dz' \\ &+ MUL \end{aligned} \tag{A.61}$$

where "MUL" is the multiple term.

In summary, the final expression of the 3^{rd} order ISS term is calculated, and the result for $\alpha_3(z)$ and $\beta_3(z)$ can be clearly expressed by collecting all the results from equations (A.11, A.16, A.15, A.59) and making the *L.H.S.* equal to the *R.H.S.*:

$$
\begin{aligned}
&\frac{1}{\cos^2\theta}\alpha_3(z) + \left(1-\tan^2\theta\right)\beta_3(z) \\
&= -\frac{1}{\cos^4\theta}\left[\alpha_1(z)-\beta_1(z)\right]\left[\alpha_2(z)-\beta_2(z)\right] + \frac{1}{4}\frac{1}{\cos^2\theta}\beta_1^2(z)\left[\alpha_1(z)-\beta_1(z)\right] \\
&+ \frac{1}{8}\frac{1}{\cos^4\theta}\beta_1(z)\left[\alpha_1(z)-\beta_1(z)\right]^2 - \frac{5}{16}\frac{1}{\cos^6\theta}\left[\alpha_1(z)-\beta_1(z)\right]^3 \\
&- \frac{1}{2}\frac{1}{\cos^4\theta}{\alpha_1}'(z)\int_{-\infty}^{z}\left[\alpha_2(z')-\beta_2(z')\right]dz' \\
&- \frac{1}{2}\frac{1}{\cos^4\theta}{\alpha_2}'(z)\int_{-\infty}^{z}\left[\alpha_1(z')-\beta_1(z')\right]dz' \\
&+ \frac{1}{2}\left(\tan^4\theta-1\right){\beta_1}'(z)\int_{-\infty}^{z}\left[\alpha_2(z')-\beta_2(z')\right]dz' \\
&+ \frac{1}{2}\left(\tan^4\theta-1\right){\beta_2}'(z)\int_{-\infty}^{z}\left[\alpha_1(z')-\beta_1(z')\right]dz' \\
&- \frac{1}{8}\frac{1}{\cos^6\theta}{\alpha_1}''(z)\left[\int_{-\infty}^{z}(\alpha_1(z')-\beta_1(z'))dz'\right]^2 \\
&- \frac{1}{8}\frac{1}{\cos^4\theta}\left(1-\tan^2\theta\right){\beta_1}''(z)\left[\int_{-\infty}^{z}(\alpha_1(z')-\beta_1(z'))dz'\right]^2 \\
&- \frac{1}{4}\frac{3}{\cos^6\theta}\alpha_1(z){\alpha_1}'(z)\int_{-\infty}^{z}\left[\alpha_1(z')-\beta_1(z')\right]dz' \\
&+ \frac{1}{4}\frac{3}{\cos^6\theta}\beta_1(z){\alpha_1}'(z)\int_{-\infty}^{z}\left[\alpha_1(z')-\beta_1(z')\right]dz' \\
&+ \frac{1}{4}\frac{1}{\cos^4\theta}\left(3\tan^2\theta+1\right)\alpha_1(z){\beta_1}'(z)\int_{-\infty}^{z}\left[\alpha_1(z')-\beta_1(z')\right]dz' \\
&+ \frac{1}{4}\frac{1}{\cos^4\theta}\left(3\tan^2\theta-1\right)\beta_1(z){\beta_1}'(z)\int_{-\infty}^{z}\left[\alpha_1(z')-\beta_1(z')\right]dz' \\
&- \frac{1}{4}\frac{1}{\cos^4\theta}{\beta_1}'(z)\int_{-\infty}^{z}\left[\alpha_1(z')-\beta_1(z')\right]^2dz'
\end{aligned}
$$

$$-\frac{1}{8}\frac{1}{\cos^6\theta}\left[\alpha_1{}'(z)-\beta_1{}'(z)\right]\int_{-\infty}^{z}\left[\alpha_1(z')-\beta_1(z')\right]^2 dz' + MUL. \tag{A.62}$$

and "MUL" is expressed as:

$$\begin{aligned}
MUL = &-\frac{1}{4cos^6\theta}\int_{-\infty}^{z} dz'\alpha_1'(z')\int_{-\infty}^{z} dz'''\alpha_1'(z''')\alpha_1(z'+z'''-z)\\
&+\Big(-\frac{1}{2cos^4\theta}+\frac{1}{4cos^6\theta}\Big)\int_{-\infty}^{z} dz'\alpha_1'(z')\int_{-\infty}^{z} dz'''\alpha_1'(z''')\beta_1(z'+z'''-z)\\
&+\Big(-\frac{1}{cos^4\theta}+\frac{1}{2cos^6\theta}\Big)\int_{-\infty}^{z} dz'\alpha_1'(z')\int_{-\infty}^{z} dz'''\beta_1'(z''')\alpha_1(z'+z'''-z)\\
&+\Big(-\frac{2}{cos^2\theta}+\frac{2}{cos^4\theta}-\frac{1}{2cos^6\theta}\Big)\int_{-\infty}^{z} dz'\alpha_1'(z')\int_{-\infty}^{z} dz'''\beta_1'(z''')\beta_1(z'+z'''-z)\\
&+\Big(-\frac{1}{cos^2\theta}+\frac{1}{cos^4\theta}-\frac{1}{4cos^6\theta}\Big)\int_{-\infty}^{z} dz'\beta_1'(z')\int_{-\infty}^{z} dz'''\beta_1'(z''')\alpha_1(z'+z'''-z)\\
&+\Big(\frac{3}{cos^2\theta}-\frac{3}{2cos^4\theta}+\frac{1}{4cos^6\theta}\Big)\int_{-\infty}^{z} dz'\beta_1'(z')\int_{-\infty}^{z} dz'''\beta_1'(z''')\beta_1(z'+z'''-z)
\end{aligned} \tag{A.63}$$